UNIVERSITY OF NAPLES "FEDERICO II"

PhD course in Aerospace, Naval and Quality Engineering

PhD Thesis in
Aerospace Engineering

"ELECTRICALLY HEATED COMPOSITE LEADING EDGES FOR AIRCRAFT ANTI-ICING APPLICATIONS"

by

Francesco De Rosa

2010

To my girlfriend Tiziana
for her patience and understanding
precious and rare human virtues

University of Naples Federico II
Department of Aerospace Engineering DIAS

PhD Thesis in Aerospace Engineering
Author: F. De Rosa
Tutor: Prof. G.P. Russo

PhD course in Aerospace, Naval and Quality Engineering
XXIII PhD course in Aerospace Engineering, 2008-2010
PhD course coordinator: Prof. A. Moccia

Abstract

An investigation was conducted in the Aerospace Engineering Department (DIAS) at Federico II University of Naples aiming to evaluate the feasibility and the performance of an electrically heated composite leading edge for anti-icing and de-icing applications. A 283 [mm] chord NACA0012 airfoil prototype was designed, manufactured and equipped with an High Temperature composite leading edge with embedded Ni-Cr heating element. The heating element was fed by a DC power supply unit and the average power densities supplied to the leading edge were ranging 1.0 to 30.0 [kW m^{-2}]. The present investigation focused on thermal tests experimentally performed under fixed icing conditions with zero AOA, Mach=0.2, total temperature of -20 [°C], liquid water content LWC=0.6 [g m^{-3}] and average mean volume droplet diameter MVD=35 [μm]. These fixed conditions represented the top icing performance of the Icing Flow Facility (IFF) available at DIAS and therefore it has represented the "sizing design case" for the tested prototype. An analytical model has been also developed both for the preliminary sizing and test guidance. Running wet and fully evaporative functional modes have been verified both analytically and experimentally with reasonable agreement. A room temperature thermal endurance test has been run for 10^4 cycles with max thermal load representative of 1.5 times the max temperature experienced within the leading edge in fully evaporative conditions aiming to verify the integrity of the composite laminate after the imposed thermal stress through micrographic inspection. The achieved results, despite obtained under limited icing conditions imposed by the IFF wind tunnel, showed great potentialities for the proposed Icing Protection System named EHCLE (Electrical Heated Composite Leading Edge) which has been constantly working below 60% of its maximum operative temperatures under the given icing conditions and the explored power densities. This potentiality justify the need for future development in a larger scale under more severe icing condition for a final assessment about the applicability of such Icing Protection System to real aircrafts.

Key words: anti-icing, de-icing, High Temperature Composite, EHCLE, IPS

Acknowledgements

I would first like to thank my Tutor and advisor Prof. G.P. Russo for his guidance. His expertise during the numerous problems encountered in this study were invaluable.

I wish to thank Dr. A. Esposito for his support and availability night and day, his extensive expertise in experimental methods and techniques has been essential to the project.

I also wish to thank all the other members of the team which has been working for more than two years to make this research feasible and among them a special gratitude goes to V. Caso and F. Parente for helping to solve experimental and numerical problems.

This work was supported by the Department of Aerospace Engineering DIAS and therefore a special thanks goes to the DIAS Director Prof. F. Marulo which believed in the project and made the laboratory available.

During the years working at the University of Naples Aerodynamics Laboratory, I had the pleasure of working with many PhD, graduate and undergraduate students. I would like to thank all of them.

Table of Contents

List of Figures

List of Tables

Nomenclature

Acronyms:

AAN: Air Atomizing Nozzle
AFM: Aircraft Flight Manual
AIM: Aeronautical Information Manual (U.S.)
AOA: Angle of Attack
BMI: Bismaleimide
CET: Coefficient of Thermal Expansion
CFRP: Carbon Fiber Reinforced Plastic
DC: Duty Current
DIAS: Dipartimento di Ingegneria Aerospaziale
EHCLE: Electrically Heated Composite Leading Edge
EIDI: Electro-Impulsive De-Icing
EP: Epoxy
FAA: Federal Aviation Authority
FE: Fully Evaporative
FLE: Fix Leading Edge
FM: Functional Mode
FMEA: Failure Mode Effects and Analysis
FVF: Fiber Volume Fraction
HE: Heating Element
HT: High Temperature
IFF: Icing Flow Facility
INBD: Inboard
IPS: Icing Protection System
ITC: Icing Test Condition
LCM: Lumped Capacitance Method
LE: Leading Edge
LPED: Low Power Electro-thermal Deicing
LWC: Liquid Water Content
MVD: Median Volume Diameter
OAT: Outside Air Temperature
OUTBD: Outboard
PDPA: Phase Doppler Particle Analyzer
PID: Proportional–Integral–Derivative (controller)
RT: Room Temperature (in the present work RT conditions always refer to 20°C)
RW: Running Wet
SAT: Static Air Temperature
SCDD: Super Cooled Drizzle Drops
SIPS: Smart Icing Protection System
SLD: Super Cooled Large Droplet
SMA: Shape Memory Alloy
TAT: Total Air Temperature
TC: Thermocouple
TC/T: Thermocouple T-type
TET: Thermal Endurance Test
VOC: Volatile Oxide Content
WSS: Water Spraying System

Abbreviations:
AUX: Auxiliary
Dim.: Dimension
Q.ty: Quantity

Subscripts:
LE denotes Leading Edge
LF denotes Liquid Film
HE denotes Heating Element
ES denotes External Surface of the Leading Edge
IS denotes Internal Surface of the Leading Edge
EXT denotes External Flow
INT denotes Leading Edge Internal cavity
INTT denotes Leading Edge Internal cavity Tentative value
LAM denoted High Temperature composite Laminate

1 Introduction

In-flight ice accretion on aircraft has been recognized since the early days of aviation as a source of threat to safety from minor up to catastrophic. Although major advancements in aircraft ice protection systems have been made over the years due to increased understanding of the ice-accretion process, accidents due to icing are still occurring.

Ice on aircraft aerodynamic surfaces destroys the smooth flow of air, decreasing lift, increasing drag, degrading control authority and decreasing the stability. The actual weight of the ice on the aeroplane is secondary to the airflow disruption it causes. As power is added to compensate for the additional drag and the nose is lifted to maintain altitude, the angle of attack increases, allowing the underside of the wings and fuselage to accumulate additional ice. Ice accumulates on every exposed frontal surface of the aeroplane, not just on the wings, propeller, and windshield, but also on the antennas, vents, intakes, and cowlings. It builds in flight where no Ice Protection System can reach it. It can cause antennas to vibrate so severely that they break. In moderate to severe conditions, a light aircraft can become so iced up that continued flight is impossible. The aeroplane may stall at much higher speeds and lower angles of attack than normal. It can roll or pitch uncontrollably, and recovery may be impossible.

Recent massive development and introduction of CFRP materials in aircraft structures has generated the need to design and develop IPSs able to perform within composite structures which, for the limited maximum continuous service temperature of classical epoxy resins, has been for years a challenging task for all major aircraft manufacturers. Nevertheless new High Temperature polymers gave the possibility to reconsider the application of thermal IPSs to composite structure by reaching max continuous service temperatures up to 200[°C] without significant degradation of structural properties, whilst for classical epoxy composites it was limited to around 85[°C].

This thesis is an attempt to preliminary design, assemble and test a thermal IPS integrated within an HT composite structure that I named with the acronym of EHCLE (Electrically Heated Composite Leading Edge) which is self explanatory of the treated topics. The IPS was built up embedding an electrical resistance within the composite leading edge skin laminate resulting in a final product which is structure and system at same time for the benefit of both. For technological reasons directly linked to the scale of the tested prototype a uniformly distributed single-path resistance was adopted leaving to future developments the possibility to investigate finer solutions using tailored multi-path resistances.

The current work is focussing to the thermal performance of a scaled model against severe icing conditions and preliminarily evaluates its capabilities to reach “Running Wet” and “Fully Evaporative” functional modes.

The engineering activity has been performed either within the Department of Aerospace Engineering (DIAS) at University of Naples Federico II, either in cooperation with SAMPE Benelux in Brussels especially for the M&P development.

The icing test activity has been performed using the “Icing Flow Facility (IFF)”, available at DIAS in Naples, which is a supersonic wind tunnel converted into subsonic icing wind tunnel. A relevant part of the present work has been spent to calibrate and set the IFF up to the requested performance level.

1.1 Research objectives

The current research was launched to understand the behaviour under severe icing conditions of an electrically heated Icing Protection System integrated into the aircraft composite wing leading edge. To preliminary evaluate feasibility and performance of such IPS a scaled model has been used and the relevant engineering and experimental activity performed on it is the core of the present work. The design method has been intentionally set as general as possible to make future applications not only possible within wing leading edges but into any composite component facing icing cycles.

A major objective has been to evaluate thermal performance limitations and material capabilities giving preliminary but essential information for higher scale future developments.

Being the system itself integrated into the composite primary structure a major role was played by the selected materials. The composite materials used in the current work are representative of the newest material family performing at high temperature by using modified epoxy resins. This choice was limited to market availability and project budget not compromising tough the overall research results. More accurate and effective investigations will be possible and part of our future activity.

Very critical has been at beginning to evaluate the possibility of achieving fully evaporative functionality within the integrity range of the composite material available and for such reason a very dense screening was performed in terms of icing test and power densities supplied to the system with the major intent of not damaging the two available prototypes essential to completeness of the test campaign. Experimental results have been in reasonable agreement with analytical forecasts with some exception which we were able to explain after deeper investigations as it will be later on shown.

This work is organized in six chapters which are going from an introduction to icing problems, through a review of relevant literature and Icing Protection Systems and trough the preliminary design phase with the complete description of the analytical method adopted. Last chapters will then introduce and describe the test apparatus, the prototype set up, the summary of the experimental results and the conclusions with an eye to future developments.

1.2 Review of Icing Literature

This paragraph will provide a summary of existing icing and icing-protection literature relevant to this work. According to a recent study [44], snow and ice accumulation was determined to be the leading cause of around 10% of all fatal aircraft accidents. Wind tunnel

and flight tests have shown that frost, snow, and ice accumulations on the leading edge or on the upper surface of the wing no thicker or rougher than few tents of millimetres can reduce lift by 30% and increase drag up to 40%. Larger accretions can reduce lift even further and increase drag by over 80%. Even aircraft equipped with IPS for flight into icing conditions are significantly affected by ice accumulation on the unprotected areas. NASA studies revealed that up to 50% of the total drag increase associated with a wing leading edge icing remained after all the protected surfaces were completely deiced [10][11]. Therefore the efficiency of the Ice Protection System is crucial for safety on one side but on the other has always been a problem for the huge amount of needed energy and also for the weight of the IPS itself. In this paragraph I will try to explain in a simply way all the physics and phenomena which are involved in aircraft icing problems whilst the Icing Protection System scenario will be treated separately within paragraph 1.4.

1.2.1 Droplet Classification

As described in [5] droplets diameters can vary from few microns to few millimeters covering then a very large spectra. Obviously there is a relation between altitude and droplet dimensions and temperature but what is very interesting is that there is a relation, coming from practical observation, between droplet diameter and ice accretion on airframe structures. This is reported in table 1.1.

Tab.1.1 Ice observation as a function of droplet diameter [22]

Droplet Category	Droplet Diameter [μm]	Observation Criteria
Small	<10	Ice accretion is limited to the leading edge of large component.
Medium	10 to 30	Ice accretion occurs aft of the leading edge but do not exceed the zones where ice protection systems are active.
Large	30 to 100	Ice accretion exceeds the zones where ice protection systems are active.
Freezing Rain or Drizzle	100 to 1000	Ice accretion has an important extend downstream.

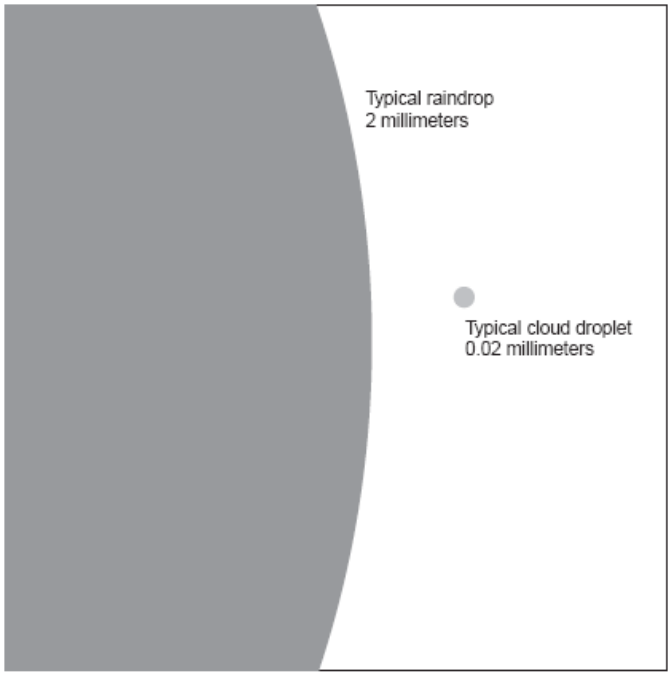

Fig.1.1 Droplet size schematic comparison[2]

1.2.2 Aircraft Icing Risks

Ice forms on aircraft surfaces at 0[°C] or colder when liquid water is present. Tab.1.2[1] illustrates the icing risk in terms of cloud type and ambient temperature.

Tab.1.2 Icing Risks[1]

Icing Risk	Cumulus Clouds	Stratiform Clouds	Rain and Drizzle
High	0°C > T > -20°C	0°C > T > -15°C	0°C > T
Medium	-20°C > T > -40°C	-15°C > T > -30°C	
Low	-40°C > T	-30°C > T	

Generally, the worst continuous icing conditions are found near the freezing level in heavy stratified clouds, or in rain, with icing possible up to 8,000 [ft] higher. Icing is rare above this higher altitude as the droplets in the clouds are already frozen. In cumuliform clouds with strong updrafts, however large water droplets may be carried to high altitudes and structural icing is possible up to very high altitudes. Further, in cumuliform cloud the freezing level may be distorted upwards in updrafts and downwards in downdrafts, often by many thousands of feet. This leads to the potential for severe icing to occur at almost any level and the efficiency of the IPS is therefore essential to minimize icing hazards.

1.2.3 Ice Shapes

The pioneering studies concerning the ice-accretion process began during the second world war and knew a massive industrial and academic diffusion in the 50's [45]. Aircraft can accrete ice on its aerodynamic surfaces when flying through clouds of super-cooled water droplets. When these droplets impact the surface of the airfoil (usually near the leading-edge stagnation region), they will either freeze on contact or run downstream in liquid state. Depending on the surface temperature of the airfoil, this flow will either freeze as it runs back or may simply run off the airfoil entirely.

The size and shape of the ice accretion depend on numerous factors: aircraft configuration, airfoil geometry, angle of attack, airspeed, temperature, water droplet size, liquid water content, and the time the aircraft has operated in icing condition. An experiment by Hansman [46] has identified four distinct types as shown in Fig. 1.2 into which most ice accretions can be categorized.

This experiment was conducted on a cylinder, but the results are applicable to airfoils as well. The rime ice was characterized by a conformal white ice and was observed at temperatures well below freezing. Mixed-ice and the two glaze-horn accretions were observed at temperatures near freezing. The mixed-ice accretions had a smooth, clear glaze near the stagnation zone with a rime-like accretion downstream. The horn A growth was characterized by glaze ice in the stagnation region surrounded by a closely spaced white-ice horns that grew into the flow. The horn B growth was similar to the horn A growth except the horns were spread farther apart and grew out radially. The horns also consisted of clear, glaze ice instead of white, rime ice.

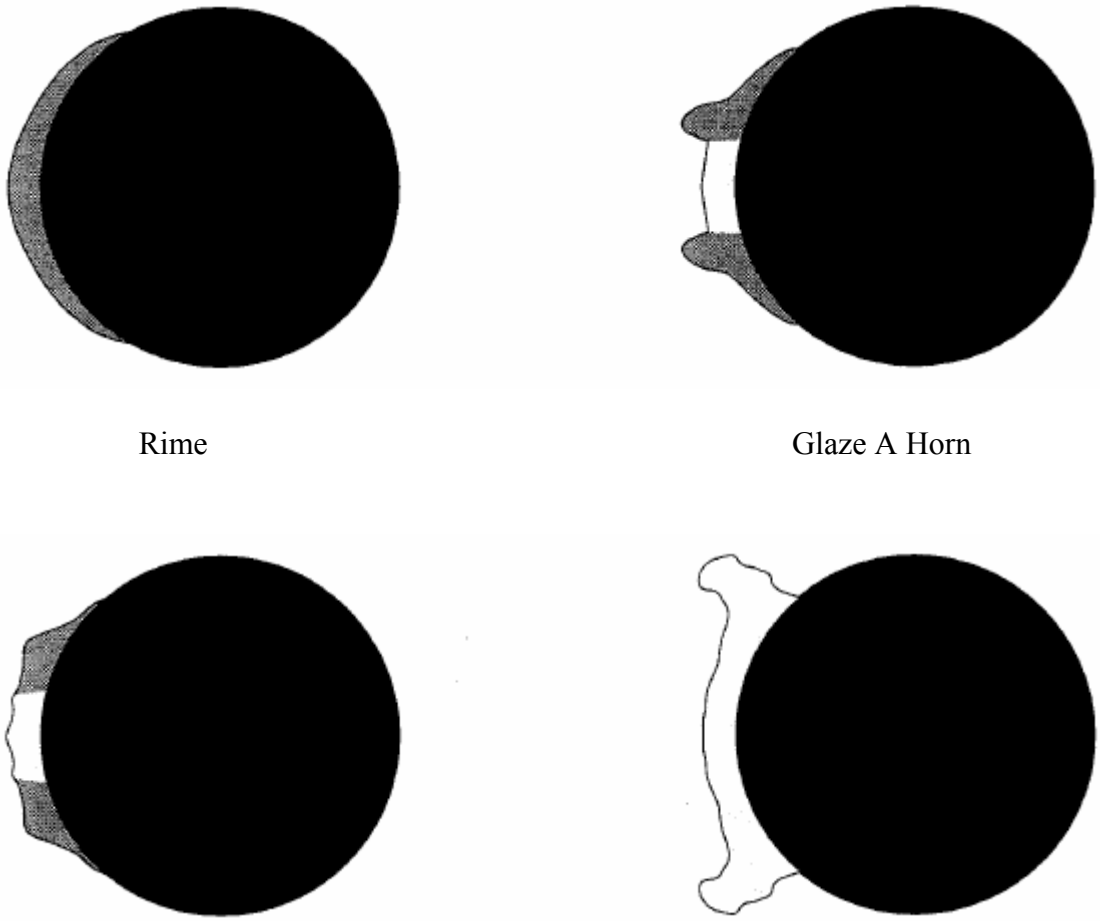

Fig.1.2 Ice accretion types according to Hansman classification[46]

1.2.4 Impingement area considerations

The impingement area is one of the key parameters for any IPS development because it heavily influences the extension of the protected areas of the leading edge. Ice could in fact accrete immediately downstream of the protected area, which typically extends between 5-10% of the chord, leaving the IPS completely inefficient [27].

The trajectory of the small droplets (found in standard icing clouds) tends to follow the streamlines around the airfoil very closely. Only the droplets near the stagnation point streamline will impinge on the airfoil surface. The droplets away from the stagnation streamline will follow the streamlines around the airfoil and will not impinge. However, the trajectory of the larger droplets is less likely to follow the streamlines around the airfoil due to

their higher inertia. Thus, as the droplet size gets larger the impingement limit moves further down the chord[48] as shown in Fig. 1.3.

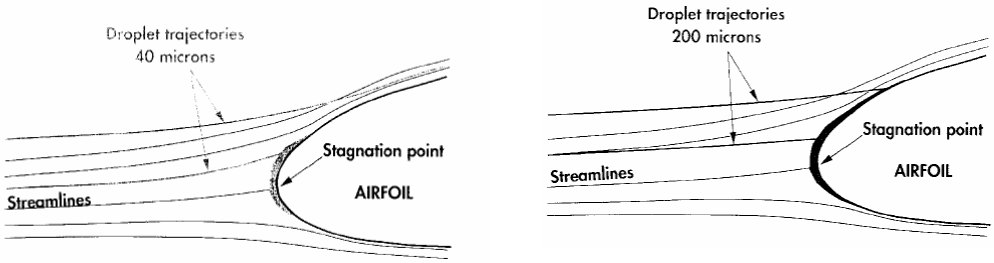

Fig.1.3 Trajectory comparison between large and small droplets

The impingement limits of SLD icing may be further downstream than the active portion of the deicing system. When the deicing system is activated, only the ice over the active portion is removed. This can lead to a spanwise-step type of ice accretion protuberance that forms behind the leading-edge deicing system.

In general, past studies have shown that the most critical protuberance location is somewhere in the vicinity of the upper limit of a pneumatic IPS and is related to the adverse pressure gradient in the recovery region [15]. Studies with glaze horn ice [55][19][59] showed that the largest reduction in performance was observed when the horn was perpendicular to the flow.

A study which examined the effects of various types of icing conditions, found that the freezing drizzle icing resulted in the most severe performance degradation [54] due to a spanwise-step ice accretion.

In low-Reynolds number wind tunnel tests with simulated ice shapes it was found that a freezing drizzle ice shape with a simulated deicing boot operation resulted in a more severe performance degradation than one without the de-icing boot operation. When the deicing boot was not in use, in fact, the ice accretion occurs around the leading edge of the wing and tends to conform to the geometry of the wing but when the de-icing system is in use, the spanwise-step shape forms immediately downstream of the boot [63].

The reduction in $\boldsymbol{Cl_{max}}$ can reach 30% and the increase in drag can reach 200% flying in icing clouds with SLD [51].

Several studies reviewed the aerodynamic effects of the SLD ice accretion showing that the SLD ice accretion severely degraded the aero performance[52][53].

The crash of the ATR-72 aircraft (with pneumatic boots IPS) near Roselawn was thought to have been a result of SLD ice accretion. Tests following the crash suggested that there was significant ridge-type ice accretion immediately behind the boots, which led to severe control

degradation. Nevertheless it has been proven that the ridge ice that formed aft of the IPS resulted in a larger lift loss and drag increase than when the leading edge was completely iced over [49].

1.2.5 Flowfield around an iced Airfoil

The severe effect of the ice shape was thought to be due, in large part, to the large separation bubble that forms downstream of the ice shape. The bubble is a complex region of unsteady re-circulating flow, with a flow structure that is analogous to the laminar separation bubble that forms on clean airfoils.

As shown in [56] the formation of a separation bubble behind a simulated leading-edge glaze ice accretion has remarkable similarities to conventional laminar separation bubbles. In this case, the ice accretion imposed a severe pressure gradient on the flow, causing the flow to separate at the horn. A separation bubble formed to reduce the necessary pressure recovery. Since there was a horn on both the upper and lower surface, a separation bubble was present on both surfaces. A region of constant pressure was followed by recovery, which marked shear-layer transition and eventually reattachment of the flow.

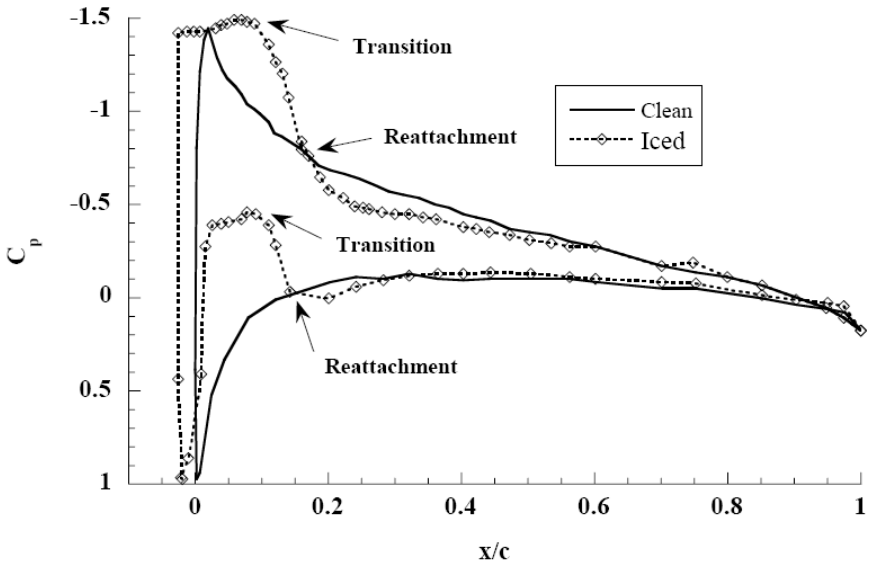

Fig.1.4 Surface pressure distribution on an airfoil with simulated glaze ice shape [56]

The authors showed that the reattachment point moved downstream with increasing angle of attack because of the increasing adverse pressure gradient. Since the ice-induced separation bubble had a global effect on the flowfield, it was classified as a long bubble. Thus, it was very clear that the large changes in the iced-airfoil performance were directly related to these separation bubbles as shown in Fig. 1.4.

1.2.6 Effects of Ice-Shape Height

It is proven [57] that increasing the ice protuberance height and moving it towards the leading edge resulted in the most severe performance degradations. All of the data showed that increasing the ice shape height generally resulted in more severe performance degradations. The exception to this was when the ice shape was located at the leading edge of the airfoil. After a critical height was reached, further increases in the height did not significantly worsen the performance degradation.

1.2.7 Effects of Ice-Shape Geometry

Ice shapes of various geometries have been tested on the leading edge of wings and horizontal tail planes showing that the glaze-horn accretions resulted in the most severe degradation of aircraft airfield with consequent loss of performance and stability whilst the rime ice accretion resulted in a reduced degradation .

Recent studies examined the effects of variations of the glaze-horn geometry showing that the leading-edge radius had very little effect on the iced-airfoil performance[58]. The effects became slightly more pronounced, as the ice shape was located further away from the leading edge. Ice horn radius effects were most pronounced for positions further away from the leading edge of the airfoil. It also appeared to be relatively insensitive to the ice shape heights. A statistical analysis of computational results of an airfoil with various leading-edge glaze horn ice accretions showed that the maximum lift did not vary significantly with the horn height [59]. However, there was a strong correlation between the horn angle and the maximum lift. Increasing the horn angle (so that it was more perpendicular to the flow) decreased the maximum lift.

1.2.8 Reynolds Number Effects

When the Reynolds number of a clean airfoil is increased, the Cl_{max} typically increases as well [61]. However, on an airfoil with surface contamination, this does not occur once a critical Reynolds number is reached, as Cl_{max} becomes relatively insensitive to increases in the Reynolds number [14]. An implication of the insensitivity of the 2-D iced-airfoil to the increases in the Reynolds number is that the wind-tunnel data generated at relatively low Reynolds number (less than 2 million) can be applied to flight Reynolds number (over 6 million) since the results will not vary significantly. Also, this indicates that when the full size ice shape/airfoil is to be scaled down to be tested using a smaller airfoil at lower Reynolds number, the proper ice shape shall be scaled by the factor k/c (direct geometric scaling, roughness/chord) and not be scaled by k/δ (roughness/local boundary layer thickness).

1.2.9 Effect of Ice Shape Location

A generalized summary of the effects of ice accretion (including roughness) on the airfoil maximum lift shows that moving the ice towards the leading edge caused the effects to become more severe [57].

The most critical location for the start of the surface roughness is at the leading edge with a loss in Cl_{max} [60]. However, for larger protuberances (larger than the local boundary-layer thickness), the most critical location is not necessarily the leading edge.

As explained in [52][53] the large performance degradations due to ice accretion are primarily due to the large separation bubble that forms downstream of the ice, causing large performance degradations and earlier stall. It was believed that the largest separation bubbles would form when the ice accretion was located near the location of Cp_{min} and the maximum adverse pressure gradient.

The relevant literature strongly indicates that for protrusions much larger than the local boundary layer thickness, the most critical chordwise location is not the leading edge, as previously thought. It is located somewhere downstream of the leading edge, with the exact location a function of airfoil geometry and protrusion height. None of the studies described identified the precise chordwise location where the protrusion had the most severe effect, primarily due to the limited number of locations tested.

1.2.10 Effects on High Lift and Control Surfaces

It is generally recognized that ice accretion can severely degrade the effectiveness of aircraft control surfaces, such as flaps, elevators, rudders, and aileron . These devices work by altering the airflow and the pressure distribution around the airfoil, thereby increasing (or decreasing) the lift generated without having to alter the angle of attack.

The degradation in effectiveness of such devices due to ice accretion can be detrimental especially for elevators. The ice accretion on the horizontal tail tends to be more severe than on the wing. This is because of its smaller chord and thinner airfoil. Because of this, the tail usually experiences greater performance degradation. Ice accretion on the aircraft wing can cause large changes in the aircraft pitching moment, which must be trimmed out using elevator deflection. This is compounded when the wing flap is deployed, causing further change in the pitching moment.

1.3 Definitions

Since design and performance of the proposed Electrically Heated Composite Leading Edge Icing Protection System (hereinafter simply called EHCLE IPS) are influenced by several factors, I will hereinafter summarize all major affected topics which will be encountered later on and which I believe are essential to better understand all choice and methodologies adopted.

1.3.1 Glaze ice (Clear Ice)

Glaze (or clear) ice is most likely to form in freezing rain, a phenomenon comprising raindrops that spread out and freeze on contact with the cold airframe. It is possible for liquid water drops to exist in the atmosphere at temperatures well below the normal freezing point of water. These are known as super-cooled drops. This situation can occur below a warm front. Super-cooled drops are unstable, and will freeze on contact with a surface that is below zero degrees like the skin of an aeroplane, or the propeller blades, for example. Freezing of each drop will be relatively gradual, due to the latent heat released in the freezing process, allowing part of the water drop to flow rearwards before it solidifies. The slower the freezing process,

the greater the flow-back of the water before it freezes. The flow-back is greatest at temperatures just at 0 [°C]. The result is a sheet of solid, clear, glazed ice with very little air enclosed. The surface of clear ice is smooth, usually with undulations and lumps. Clear ice can alter the aerodynamic shape of airfoils quite dramatically and reduce or destroy their effectiveness Clear ice is tenacious and, if it does break off, large chunks may damage the airframe. Freezing rain may exist at higher altitudes in the presence of ice pellets, formed by rain falling from warmer air and freezing during descent through colder air. That is, the presence of ice pellets usually indicates cold air below freezing with a layer of warmer air above. Wet snow, however, indicates sub zero temperatures at some higher altitude. The snow, which formed in the sub-zero temperatures of air above, melts to form wet snow as it passes through the warmer air at lower levels.

1.3.2 Rime Ice

Rime ice occurs when tiny, super-cooled liquid water droplets freeze on contact with a surface whose temperature is below freezing. Because the droplets are small, the amount of water remaining after the initial freezing is insufficient to coalesce into a continuous sheet before freezing. The result is a mixture of tiny ice particles and trapped air, giving a rough, opaque, crystalline deposit that is fairly brittle. Rime ice often forms on leading edges and can affect the aerodynamic qualities of an airfoil or the airflow into the engine intake. Due entrapped air, and slow accumulation rate, rime usually does not cause a significant increase in weight.
The temperature range for the formation of rime ice can be between 0[°C] and –40[°C], but is most commonly encountered in the range from –10[°C] to –20[°C].

1.3.3 Mixed Ice

Different moisture droplet sizes are commonly encountered in cloud, this variation produces a mixture of clear ice (from large drops) and rime (from small droplets.) Known as mixed ice, or in some countries as cloudy ice, most ice encounters take this form. Pure rime ice is usually confined to high altostratus or altocumulus, while pure clear ice is confined to freezing rain (below nimbostratus.)

1.3.4 Hoar Frost

Frost occurs when moist air comes in contact with a surface at sub zero temperatures. The water vapour, rather than condensing to form liquid water, changes directly to ice and deposits in the form of frost. This is a white crystalline coating that can usually be brushed off. Typical conditions for frost to deposit on a surface require a clear night, calm wind, and high humidity. Frost can form on an aeroplane when it is parked in temperatures less than 0[°C], with a dew deposit. Frost can also occur in flight when the aircraft flies from below freezing temperatures into warmer moist air – for example, on descent, or when climbing through a temperature inversion. Although frost can obscure vision through a cockpit window and degrade a wing's lift, frost does not alter the basic aerodynamic shape of the wing (unlike clear ice) however it can disrupt the smooth airflow over the wing, inducing early separation of the airflow over the upper surface. Frost is particularly dangerous during take-off when the flow disturbance may be sufficient to prevent the aeroplane becoming airborne.

1.3.5 Ice Accretion Mechanism

The leading edge of a wing flying into icing air is supposed to be exactly at air temperature. That air is loaded with water droplets, but air particles do pass around the leading edge without touching it (continuity of airflow). Since water droplets are much heavier than air particles, they do not pass around as easily, and some of them impact the leading edge. Supercooled water freezes on impact. Ice accretion results from the continuation of this process.

1.3.6 Double Horn Shape

The above process leads to an uneven distribution of water droplet impacting the leading edge. The supercooled liquid about to impact the middle of the leading edge is slightly deflected because of a slighter curved path than the airflow due inertia, and therefore freezes on the upper and lower portion of the leading edge. This process starts the double horn shape on the leading edge, and is a divergent process that is further enhanced by ram effect.

1.3.7 Ram Effect

It is a basic aerodynamic principle that due to the Bernoulli principle, the temperature at stagnation points on the airplane's outer surfaces will be greater than the static air temperature. The ram rise is directly proportional to the square of the aeroplane speed, i.e., the faster the aeroplane, the greater the ram rise. Hence it is possible for the aeroplane not to collect any ice even though it is flying in icing conditions, i.e., atmosphere concentrated with super cooled liquid water droplets at subfreezing temperatures. For example, the air temperature rise at 150 [knots] and 10,000 [ft] is 4[°C], whereas the temperature rise at 300 [knots] at the same altitude is 16[°C]. It is important to take this temperature rise into account for the assessment of ice accretion.

1.3.8 Run Back Ice and Shear Forces

An aircraft flying in icing conditions when the leading edge temperature is positive can experience run back icing. Due to ram energy, water droplets do not ice at impact, but explode into numerous small particles that migrate by the airflow along the wing surfaces. When the wing surface temperature is below 0[°C], it will cool the water. If the cooling effect is quicker than the blowing off, the water will ice on the spot. This process is called run back ice. Efficiency of the blowing off process depends on the shear forces present in the boundary layer. Higher airspeed will increase shear force.

1.3.9 Sublimation

Ice accrued on surfaces can be dissipated through sublimation. Sublimation is the direct change of water from a solid to vapour. Once out of cloud and icing conditions, the accrued ice thickness on the airframe will decrease. The rate of sublimation is dependent on the relative humidity of the air and on the airspeed.

1.3.10 Importance of Airspeed

Table 1.3 shows the required airspeed and Static Air Temperature (SAT) that will result in Total Air Temperature (TAT) of 0[°C] and 10[°C] at the wing leading edge of the aeroplane in level flight at 10,000 [ft] (SAT is coincident with the Outside Air Temperature, OAT) [1].

Tab.1.3 Resulting SAT and TAT Due to Airspeed[1]

Airspeed at 10,000 feet	**Static Air Temperature (SAT) Equivalent to**	
Airspeed (KCAS)	0°C TAT	+10°C TAT
250	-10.7°C	-1.1°C
290	-14.2°C	-4.7°C
330	-18.0°C	-8.7°C

The TATs shown in the table are at the stagnation points on the wing and empennage leading edges. Consideration must also be given to the temperature behind the leading edges and other surfaces on the aeroplane where the surface temperature may be lower than at the stagnation points. If the leading edge is at 0[°C] TAT, the wing surface behind the leading edge will be at a negative temperature and, depending on the aeroplane speed, there is a possibility of run-back ice formation behind the leading edge. Speeds that result in higher than 0[°C] TAT at the leading edge will minimise any significant formation of runback ice.

1.3.11 Cloud types

Cumulus-type. Cumulus-type clouds consist predominantly of liquid water droplets at temperatures down to about –20[°C]. Below this temperature either liquid drops or ice crystals may predominate. Newly formed cloud segments will tend to contain more liquid drops than mature parts. The risk of airframe icing is severe in cumuliform clouds in the range 0[°C] to –20[°C]. Airframe ice is unlikely below –40[°C]. The vertical motion in a convective cloud varies its composition and corresponding ice risk throughout a wide altitude band. Updrafts will tend to carry the water droplets higher and increase their size. If significant structural icing does occur, it may be necessary to descend into warmer air.

Stratiform. Liquid water drops down to about –15[°C], with a corresponding risk of structural icing, usually predominates in stratiform clouds. If significant icing is a possibility, it may be advisable to fly at a lower level where the temperature is above 0[°C], or at a higher level where the temperature is colder than –15[°C]. Stratiform clouds associated with an active front or with orographic lifting of a moist maritime stream, increase the icing probability at temperatures lower than usual; continuous upward motion of air generally means a greater retention of liquid water in the clouds.

Rain and drizzle. Raindrops and drizzle from any sort of clouds will freeze on contact with a surface whose temperature is below 0[°C]. The risk of severe clear ice increases with the size of the water drops. Vigilance is essential when flying in rain at freezing temperatures.

High- level clouds. High level clouds such as cirrus clouds, with their bases above 20,000 [ft], are usually composed of ice crystals that will not freeze onto the aeroplane, and so the risk of structural icing is slight when flying at very high levels.

1.3.12 Liquid Water Content in Clouds (LWC)

The greater the water content the greater the rate of ice accretion. High water content is often found in clouds caused by orographic and frontal lifting. An added and important factor that determines the water content is temperature at the cloud base. Recalling that warm air requires greater water content at saturation than cold air it follows that a warm cloud base implies high water content. Thus, curiously, ice accretion due to water content is more severe in summer (when clouds can be expected to be warmer) than in winter. Similarly, water content in tropical cloud is greater than in polar cloud and therefore the rate at which ice builds up is greater in the tropics (above the freezing level) than in Polar Regions.

A study made 1949 shows a classification of LWC in function of MVD in clouds and, despite there have been several attempts to modify it and extend it (dashed area in Fig.1.6), is today still valid and still adopted by certification authorities and industries for the certification of Aircraft Ice Protection Systems [25]. Fig.1.5 and Fig.1.6 show FAA approach taken for example data extracted and plotted from [25].

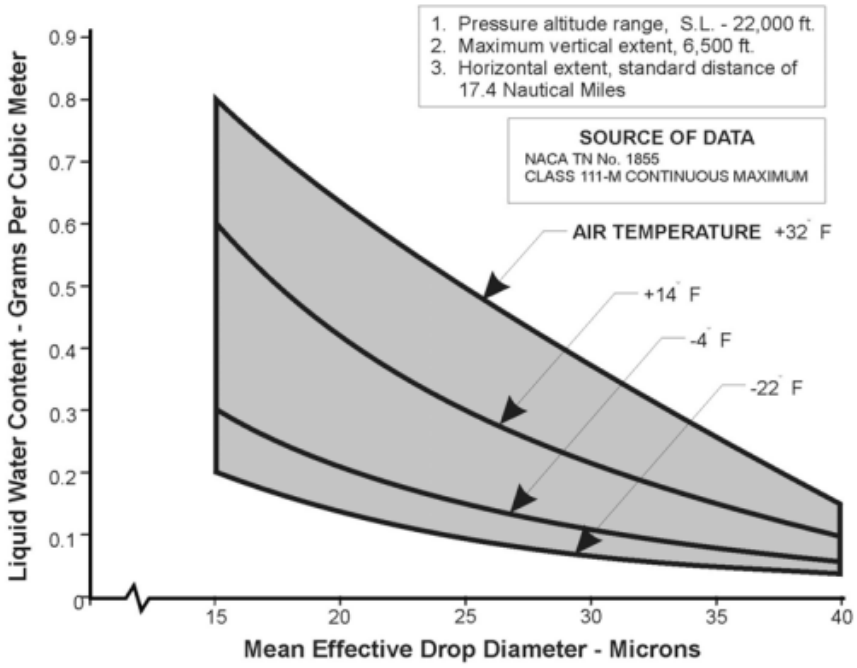

Fig.1.5 LWC vs. Mean Effective Drop Diameter for Stratiform Clouds [25][26]

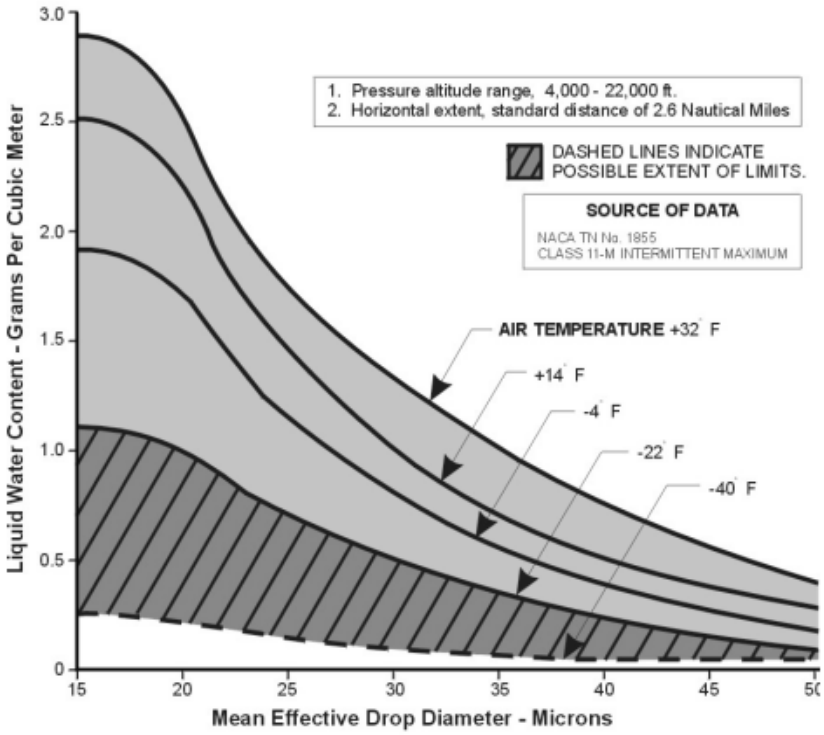

Fig.1.6 LWC vs. Mean Effective Drop Diameter for Cumuliform Clouds [25][26]

The graph proposed in Fig.1.6 is shown in the version proposed by FAA in 2009 for limits extension (dashed area represents the extension proposal [26]).

1.3.13 Ice collection efficiency E_M and water interception rate M_T

The ice collection efficiency $\boldsymbol{E_M}$ of an airfoil is an essential parameter to calculate the amount of water intercepted by the leading edge $\boldsymbol{M_T}$ and therefore to size the Ice Protection System. The collection efficiency is defined [24] as the ratio of the water intercepted by a component to the total mass of water in the volume swept out by the moving airfoil at zero AOA. It is function of geometry, airspeed, AOA, droplet size, air temperature and pressure. An example is given in Fig. 1.7.

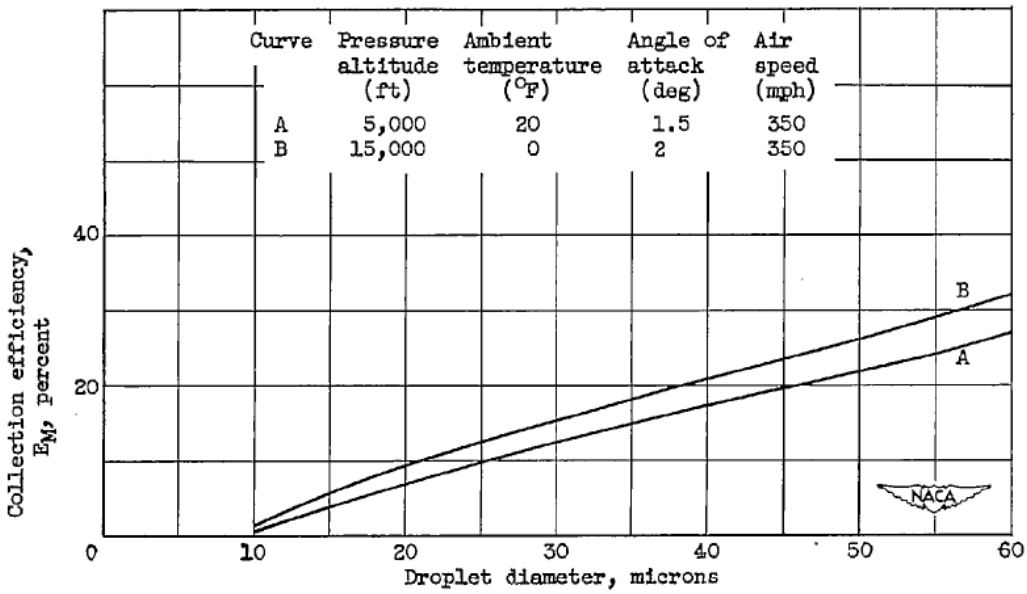

Fig.1.7 Collection efficiency example of a 12% thick airfoil and 4.8[m] chord[24]

The water interception rate can then be written [24] as following:

$$M_T = 0.3296\ E_M\, V\,(LWC)\, t\, C \tag{1.1}$$

where

$\boldsymbol{M_T}$ is the mass of intercepted water per hour and per meter span [lbs h^{-1} m^{-1}]

0.3296 is a conversion factor

E_M collection efficiency of the airfoil as percentage (%)

V airspeed [miles h^{-1}]

LWC is the liquid water content [g m^{-3}]

t is the airfoil thickness as chord percentage (%)

C is the airfoil chord length [ft]

The problem of ice collection efficiency is extensively treated within [28].

1.3.14 Icing Characteristics

Sharp components such as thin leading edges, fins, aerials, propeller and helicopter blades gather ice more readily than blunt components. The main reason is that air tends to stagnate at blunt objects increasing the ambient pressure that, in turn, increases the temperature. Similarly, sharp items have thin boundary layers giving little insulation between skin and ice. This principle is also relevant when considering thrust produced by a propeller. When ice builds up, the additional thrust requirement may not be available if propeller blade efficiency has been degraded. Indicated airspeed also influences the rate of ice accretion, below 250 [knots], in fact, the higher the speed the faster ice accumulates. Kinetic heating due to skin friction at speeds above 250[knots] reduces risks of icing significantly.

1.3.15 Super Cooled Drizzle Drops

The physics of ice formation and altitude vs. temperature profiles differ between freezing drizzle and SCDD, but for the discussion of ice accretion only, freezing drizzle and SCDD may be considered synonymous. Droplets of supercooled liquid water at temperatures below 0[°C] having diameters of 40[μm] to 400[μm] are found in both freezing drizzle and SCDD. No aircraft is certificated for flight in supercooled large droplet (SLD) conditions. Surface temperature varies with air pressure along the airfoil. At the leading edge, where pressure is the highest, the surface temperature will also be higher than farther aft. If the local surface temperature on the airfoil is warmer than freezing, no ice will form. At temperatures close to

freezing, there may be no ice on the leading edge, but ice can form further aft because of the lower temperatures. Because there is liquid runback, any ice formation aft of the leading edge tends to act like a dam, making ice growth more rapid

1.3.16 Icing Certification

With regard to ice protection, airplane type certification is currently accomplished by meeting either the requirement of JAR 23.1419 or JAR 25.1419 (or equivalent FAR) and relevant interpretative material ACJ or equivalent FAA AC [3]. These rules require an analysis to establish the adequacy of the ice protection system for the various components of the airplane based on the operational needs of that particular aircraft. In addition, tests of the ice protection system must be conducted to demonstrate that the airplane is capable of operating safely in the continuous maximum and intermittent maximum icing conditions. These conditions are described in JAR/FAR Part 25, Appendix C. The type certificate data sheet (TCDS) gives the certification basis for the airplane and lists the regulations with which the airplane has demonstrated compliance. Therefore, when an aeroplane complies with one of the regulations which refers to Part 25, appendix C, the icing certification is indicated on the TCDS and in the AFM. The AFM lists the equipment required to be installed and operable.

The JAA (or FAA) operating rules also permit flight into specified icing conditions provided that the aircraft has an Icing Protection System protecting specified areas of the aircraft. There are aircraft with partial IPS that do not meet the certification or the operating regulatory requirements for flight into icing conditions. Those installations are approved because it has been demonstrated that the equipment does not adversely affect the aircraft's structure, systems, flight characteristics, or performance. In such cases, the AFM or other approved material must explain the appropriate operating procedures for the partial IPS and contain a clear statement that the aircraft is not approved for flight into known icing condition.

It is important for pilots to understand that an airplane equipped with some types of deicing and/or anti-icing systems may not be approved for flight into known icing conditions. To be approved for such flight, the airplane must be specifically certificated to operate in known icing conditions. It is important to remember that the certification standards provide protection for the majority of atmospheric conditions encountered, but not for freezing rain or freezing drizzle or for conditions with a mixture of supercooled droplets and snow or ice

particles. Some airfoils are degraded by even a thin accumulation of ice aft of the IPS that can occur in freezing rain or freezing drizzle.

For certification purposes it is necessary to prepare analyses to substantiate decisions involving application of selected ice protection equipment and to substantiate decisions to chose protected and unprotected areas. All analyses should be validated either by tests or by previously JAA or FAA approved methods. This substantiation should include a discussion of the assumptions made in the analyses and the design provisions included to compensate for these assumptions.

It is possible to demonstrate that protection is not required for some exposed areas and components by including supporting data in the relevant certification analysis. In this case it is necessary to demonstrate that allowing for such unprotected exposed areas does not adversely affect the handling or performance of the aeroplane.

The 45-minute Hold Condition. The 45-minule-hold criterion [2] should be used in developing critical ice shapes for which the operational characteristics of the overall aeroplane are to be analysed. The aeroplane's tolerance to continuous ice accumulation on the unprotected surfaces should be evaluated. For certification purposes it is necessary to determine the effect of the 45-minute hold in continuous maximum icing conditions. A median droplet diameter of 22[μm] and a liquid water content of 0.5 [g m^{-3}] with no horizontal extent correction is normally used for this analysis.

Flutter Analysis. A flutter investigation should be made to show that flutter characteristics are not adversely affected, taking into account the effects of mass distribution of ice accumulations. This investigation relates to unprotected surfaces and to protected surfaces where residual accumulations are allowed throughout the normal airspeed and altitude envelope. The effect of ice shapes on aerodynamic properties need not be considered for flutter analysis [2].

Power Sources. It is necessary for certification purposes to evaluate the power sources in the adopted IPS. Electrical, bleed air, and pneumatic sources are normally used. A load analysis or test should be conducted on each power source to determine that the power source is adequate to supply the ice protection system, plus all other essential loads throughout the aeroplane flight envelope under conditions requiring operation of the ice protection system.

Failure Analysis. Substantiation of the hazard classification of ice protection failure is typically accomplished through analyses and/or testing. A failure modes and effects analysis (FMEA) is the bottom- up method used for identifying hazards that may result from failures. During the analysis, each identifiable failure within the system should be examined for its effect on the aeroplane and its occupants.

Impingement Limit Analyses. For certification purposes it is necessary to develop a droplet trajectory and impingement analysis of the wing, horizontal and vertical stabilisers, propellers, and any other leading edges that may require protection. This analysis should examine all critical conditions within the aeroplane's operating envelope, as well as those in the icing envelope of Part 25, Appendix C. This analysis is needed to establish the upper and lower aft droplet impingement limits that can then be used to establish the aft ice formation limit and the protective coverage needed. Typically, 40[μm] droplets are used to establish the aft impingement limits, while 20[μm] droplets are used to establish the water collection rate.

1.3.17 Icing Severity Classification

The U.S. Aeronautical Information Manual (AIM) defines "severe icing" when "the rate of accumulation is such that the de-icing/anti-icing system fails to control the hazard and an immediate flight diversion is necessary." Severity in the context of the AIM is associated with rapid growth of visible ice shapes, most often produced in conditions of high liquid water content (LWC) and other combinations of environmental and flight conditions.

Ice associated with freezing rain or freezing drizzle accreting beyond the limit of the ice-protection system is also described as "severe". This kind of ice may not develop large shapes, and may not produce familiar aerodynamic degradation such as high drag, but nonetheless, may be hazardous. Freezing rain and freezing drizzle contain droplets larger than those considered for certification, and temperatures near freezing can produce this kind of severe icing.

As prescribed by JAA and FAA policy, 40[μm] diameter droplets are normally used to determine the aft limit of ice-protection system coverage. Drizzle drops diameter may be 10 times bigger 400[μm], with 10^3 times bigger inertia and approximately 10^2 times bigger drag than smaller droplets. Drizzle drops not only impinge on the protected area of the airplane, but may impinge out of the protected area.

Freezing raindrops diameter can reach 4[mm] but tends to form in a layer sometimes coating an entire aircraft. Freezing drizzle tends to form with less extensive coverage than freezing rain, but with higher ridges. It also forms ice fingers or feathers, ice shapes perpendicular to the surface of the airfoil.

To avoid misinterpretation, in this work we will refer to FAA Classification for "Icing Severity" as shown in the following table.

As will be later on shown, to evaluate the limit capabilities of the proposed IPS (EHCLE), we will perform all icing test within the IFF Icing Tunnel in condition which are very difficult to relate to the FAA (and JAA) classification. In fact assuming that in the future an ice repellent leading edge material will exist, it will fly always in non severe icing conditions whatever the cloud is, nevertheless in the same cloud an old aircraft will be in trouble. This is to say that the FAA classification, shown in Tab. 1.4, relates to the "severity" of the "ice accretion" but not to the severity of the "cloud" the aircraft is flying into.

Tab.1.4 FAA Ice Severity Classification

FAA ICE SEVERITY CLASSIFICATION			
SEVERITY	ICE ACCRETION RATES		
	Time required for 1/4 [in] accretion, t_A	Accretion per minute M_A	Accretion per hour M_A
	[min]	[mm]	[in]
LIGHT	$15 < t_A < 60$	$0,1 < M_A < 0,4$	$0,25 < M_A < 1,0$
MODERATE	$5 < t_A < 15$	$0,4 < M_A < 1,3$	$1,0 < M_A < 3,0$
HEAVY (SEVERE)	$t_A < 5$	$1,3 < M_A$	$3,0 < M_A$

Nevertheless other "Icing Severity" classifications exist and sometimes are crossing the FAA one in one or more points ending to be very similar. The one proposed in [5] is seeing the icing hazard more from the IPS view point and it can be correlated to the LWC as shown in Tab. 1.5.

Tab.1.5 Airframe Icing Severity classification and correlation to LWC [5]

Ice Intensity	Description	Cumuliform Clouds	Stratiform Clouds
		Droplet Diameter 17 [μm]	Droplet Diameter 14 [μm]
		LWC	**LWC**
		[g/m^3]	[g/m^3]
Trace	Ice becomes perceptible. Rate of accumulation slightly greater than rate of sublimation. It is not a hazard even though except when deicing/anti-icing equipment is not utilized, unless encountered for an extended period of time (over one hour).	0.07	0.11
Light	The rate of accumulation may create a problem if flight is prolonged in this environment (over one hour). Occasional use of deicing/antiicing equipment removes/prevents accumulation. It does not present a problem if deicing/anti-icing equipment is used.	0.08 to 0.49	0.12 to 0.68
Moderate	The rate of accumulation is such that even short encounters become potentially hazardous and use of deicing/anti-icing equipment or diversion is necessary.	0.50 to 1.00	0.69 to 1.33
Severe	The rate of accumulation is such that deicing/anti-icing equipment fails to reduce or control the hazard. Immediate diversion is necessary.	> 1.00	> 1.33

1.3.18 Supercooled Large Droplet (SLD)

The term supercooled large droplets (SLD) is used to describe droplets larger than 50[μm]. These are larger than those prescribed in the JAA and FAA Part 25, Appendix C for certification. It was originally thought that SLD arise from the classic melting of snow as it falls through a warm layer, becoming rain or drizzle drops. These then fall through a subfreezing layer and become freezing rain or drizzle. More recently, however, it was discovered that SLD could also form entirely in a liquid state, without the classic process of freezing and then melting [47]. It has been recognized that icing clouds with droplets the size of SLD can pose significant threat to the safety of aircraft. However, because SLD encounters has shown a very limited and brief occurrence, they were not part of the JAA and FAA Part 25, Appendix C icing envelope, and aircraft manufactures were not required to test their aircraft in SLD conditions as part of the certification process. Pilots were simply told to avoid encounters with SLD icing clouds.

1.4 Review of Anti-icing and De-icing Systems

Aircraft remove in-flight ice accretion by activating ice protection systems. Most systems in use today can be categorized into two main types: thermal and pneumatic. Other types like vibrational, chemical, Shape Memory Alloys and Super-hydrophobic have limited real applications and are still under development.

Thermal systems melt the ice accretion or prevent the ice from forming by application of heat on the protected surface of the wing. This is done either through use of electric heaters or by ducting hot bleed air from the jet engine. The bleed-air thermal system is common on jet-powered aircraft and is capable of either Anti-Icing or Deicing functionalities. Since the very beginning of the modern era of civil aviation it was thought to use part of the energy produced by the engine to face the in flight icing of wing leading edges [6]. Main reason was not only the availability of an already existing energy source but also the fact that in most of the cases such source was very close to the leading edge minimizing the impact of the systems.

Pneumatic deicing systems usually consist of an inflatable rubber boot located at the leading edge of the wing. This boot is inflated with air, causing the ice accreted over it to break and shed off the surface. The pneumatic deicing system is common on piston-engine aircraft (which cannot generate any bleed air) and turbo-prop powered aircraft (which cannot generate sufficient bleed air) and is only capable of deicing functionality.

The Deicing system typically covers the region of the wing leading edge where the ice is likely to accrete during standard icing encounters prescribed by JAA and FAA Part 25, Appendix C icing envelopes used in aircraft certification.

Ice Protection Systems (IPS) can be selected and designed according to specific needs and specific aircraft flight envelopes [64][65]. Typical applications of IPSs other than the wing leading edges concerns also the engine nacelle lips where ice accretion can be as detrimental as for the wing itself [4]. Therefore each IPS has is own impact on weight, energy consumption and cost, therefore trying to classify all possible technical solutions will certainly lead to rankings without a general validity. For these reasons I will hereinafter present the most common technical solutions limiting the discussion to the description level as shown in Tab. 1.6.

Tab.1.6 Icing Protection Systems Classification

IPS FAMILY	IPS types	ANTI-ICING CAPABILITY YES/NO	DE-ICING CAPABILITY YES/NO	STATE OF THE ART
THERMAL	**AIR BLEED**	YES	YES	MOST COMMON SOLUTION FOR JET AIRPLANES
	MICROWAVE FOR ALUMUNIUM	NO	YES	UNDER DEVELOPMENT
	MICROWAVE FOR CFRP	YES	YES	UNDER DEVELOPMENT
	ELECTROTHERMAL (SHEETS)	YES	YES	USED IN HELICOPTER BLADES AND PROPELLERS IPS
	ELECTROTHERMAL (CIRCUITS)	YES	YES	UNDER DEVELOPMENT
	ELECTROTHERMAL (COATED WIRES OR FIBERS)	YES	YES	UNDER DEVELOPMENT
VIBRATIONAL	ELECTRO IMPULSIVE EIDI (COIL)	NO	YES	USED IN SOME RUSSIAN AND SWEDISH AIRPLANES
	ELECTRO EXPULSIVE (FOIL)	NO	YES	FAA CERTIFIED AND USED IN SOME SMALL AIRPLANES
	ULTRASONIC	NO	YES	AMERICAN PATENT BUT NO APPLICATIONS
THERMO VIBRATIONAL	THERMAL AND ELECTRO EXPULSIVE	YES	YES	FAA CERTIFIED BUT NO APPLICATIONS
DEFORMATION	**PNEUMATIC**	NO	YES	MOST COMMON SOLUTION FOR PROPELLER AIRPLANES
	ELECTRO EXPULSIVE (BOOTS)	NO	YES	UNDER DEVELOPMENT
	SHAPE MEMORY ALLOY (SMA)	NO	YES	UNDER DEVELOPMENT
CHEMICAL	FLUIDS	NO	YES	USED IN SOME AIRPLANE
	ELECTROLYTIC	NO	YES	UNDER DEVELOPMENT
HYDROPHOBIC	HYDROPHOBIC NANO-PILLAR ARRAYS	YES	YES	UNDER DEVELOPMENT

Hereinafter a short description of the above classified Icing Protection Systems.

1.4.1 Air-Bleed Ice Protection System

The Air-Bleed Ice Protection System is capable of either De-Icing or Anti-Icing functionality by stilling hot air from engine compressors and distributing it by tubes to the areas to be protected. The hot air flows within a tube (so called Piccolo Tube) which extends spanwise very close to the inner surface of the leading edge to be deiced and due to the high pressure, ranging typically 2 to3 [bar], it exhausts through little holes which work like nozzles resulting in a multitude of little flows which hit the inner face of leading edge. The thermal power transferred to the leading edge depends, a part from hot air temperature, on dimension and density of these holes on the Piccolo Tube as shown in Fig.1.8. The heat transfer mechanism starts by convection on the inner side of the metallic Leading Edge skin and develops as conduction through skin itself up to the external surface. The ice is therefore prevented and/or removed by evaporation or melting (less energy consumption than evaporation but run-back ice possible). The Air-Bleed Ice Protection System is located within the most forward portion of the leading edge 5÷10% of the chord (within the FLE for non-high-lifted LE structures or within the slat structure for high-lifted LE). The system is lifetime reliable but requires several inspections.

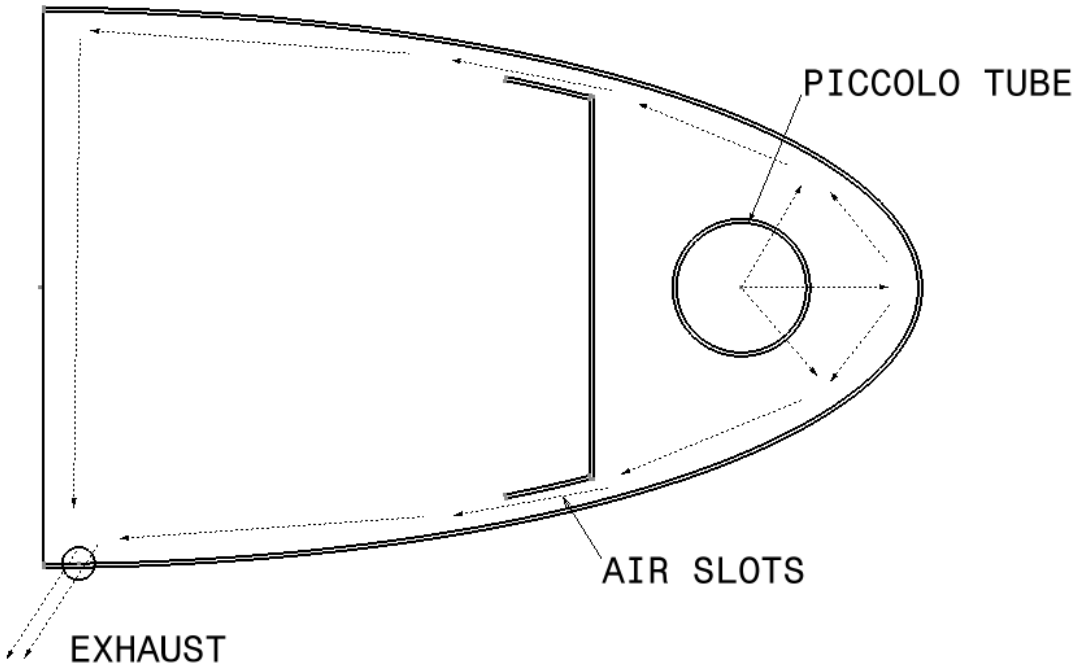

Fig.1.8 Air-Bleed Icing Protection System principle

The used power can be estimated in terms of 2-3% more fuel consumption when system is on with 200-300[kW] thermal power used [28][5] for continuous heating in running wet conditions but it can sensibly increase for the most severe icing conditions in fully evaporative mode topping 1.2[MW]. A scheme of the Fluid IPS is shown in Fig. 1.8 and Fig.1.9.

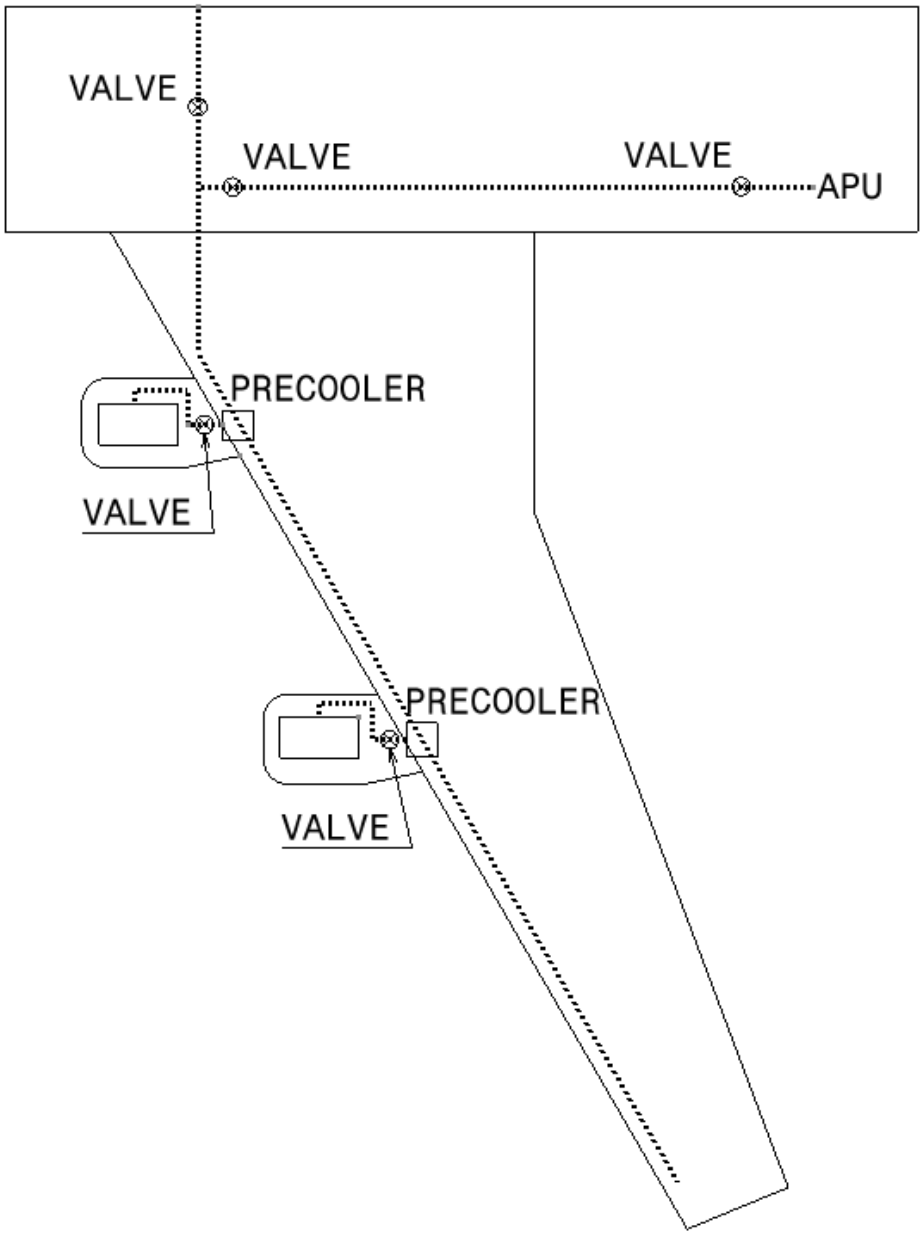

Fig.1.9 Air-Bleed Icing Protection System layout

When used for cyclical heating in the same icing conditions the required total power can be much lower because there is no need to evaporate all the impinging water [30] but the power

density can be higher as much as 50% [28]. Typically for cyclic thermal de-icing, switch-ON and switch-OFF intervals are 10÷20[s] versus 2÷4[min] respectively. The surface heating ratio can be assumed around 5÷10[kW m^{-2}] for running wet working mode and 15÷30 [kW m^{-2}] when water is completely evaporated [6][7]. When the system is on there is a relative reduction of maximum thrust. The Air-Bleed Ice Protection System is implemented in most large Jet aircraft with ice protection.

1.4.2 Fluid Ice Protection System

The Air-Bleed Ice Protection System is capable of either De-Icing or Anti-Icing functionality by pumping a glycol-based fluid under pressure through a porous material along the leading edge; such fluid is acting as freezing point depressant and therefore it can either prevent ice accretion either de-bond already accreted ice. The leading edge is partially made of porous panel within the affected zones [5]. The system is lifetime reliable and the pump uses only 30÷100[W] but the fluid consumption is quite high and it has to be refilled regularly. The fluid has to be filtered and the filters also have to replaced regularly. A scheme of the Fluid IPS is shown in Fig. 1.10.

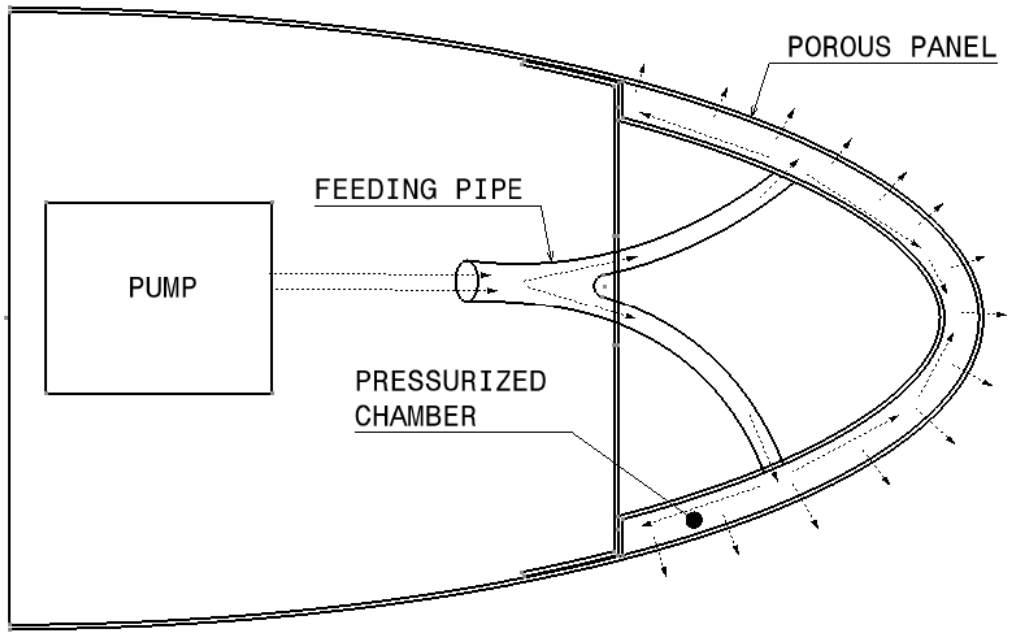

Fig.1.10 Fluid Icing Protection System layout

1.4.3 Pneumatic De-Icing

The Pneumatic Ice Protection System is only capable of De-Icing functionality (no Anti-Icing function is possible) by a burst of expanding bleed air in a flexible channel underneath the boot surface which causes rapid distortion of its surface. The induced bending and the shear stresses break the bonds between ice and surface. Alternative systems work with pumps and ambient air or a stored air reservoir.

The system transforms potential energy into kinetic energy but the heat energy is lost and not used reducing the overall efficiency of the system.

For a typical regional airplane the power consumption can be estimated around 0.3÷0.5 [W m^{-2}] absorbed by the valves and 8÷10 [m^3 h^{-1}] maximum continuous bleed air. These values increase for maximum intermittent bleed air during inflation cycles topping 9÷10 [W m^{-2}] and 40÷60 [m^3 h^{-1}] bleed air.

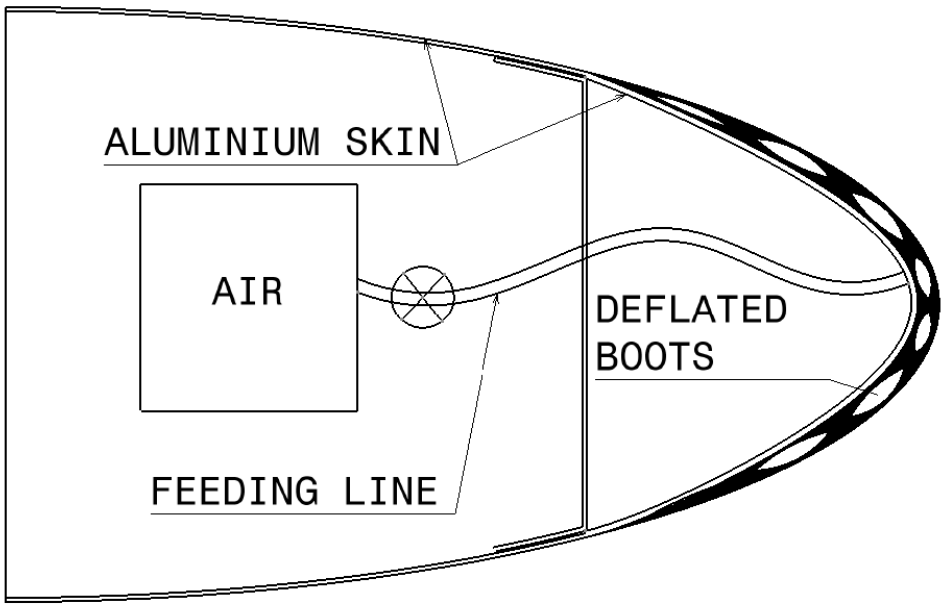

Fig.1.11 Pneumatic Icing Protection System layout

The system is lifetime reliable but a small quantity of icing water can penetrate into the boots reducing the efficiency and the thermal fluctuations can cause porosity, vulcanization and cracks into the rubber. In severe icing conditions it has been verified that during cyclic operations of the boots some ice-accretion can take place out of the protected area on the

upper wing and for long exposition it was causing a spanwise ice step which was impossible to remove [2][5][15].

The Pneumatic De-Icing system is implemented in most of regional and small airplanes with propeller engines. A scheme of the Pneumatic IPS is shown in Fig. 1.11.

1.4.4 Vibrating Electro-Impulse De-Icing System

The Electro-Impulse Icing Protection System is only capable of De-Icing functionality (no Anti-Icing function is possible) by high voltage electric currents discharged through coils underneath the skin surface. Such discharge induces eddy currents and vibrations in the aircraft skin causing the disband of the accreted ice. In fact it generates two electromagnetic fields which are repulsive resulting in a high pressure on the surface skin [5][20].

The power consumption tops 250÷300 [W] in total for a military aircraft which is typically equivalent to 15[W] per meter along the wing span.

The system is lifetime reliable but the coils are heavy and that's the reason why is not widely implemented. This system was developed in Russia for Military aircrafts. A scheme of the Vibrating Electro-Impulse IPS is shown in Fig. 1.12.

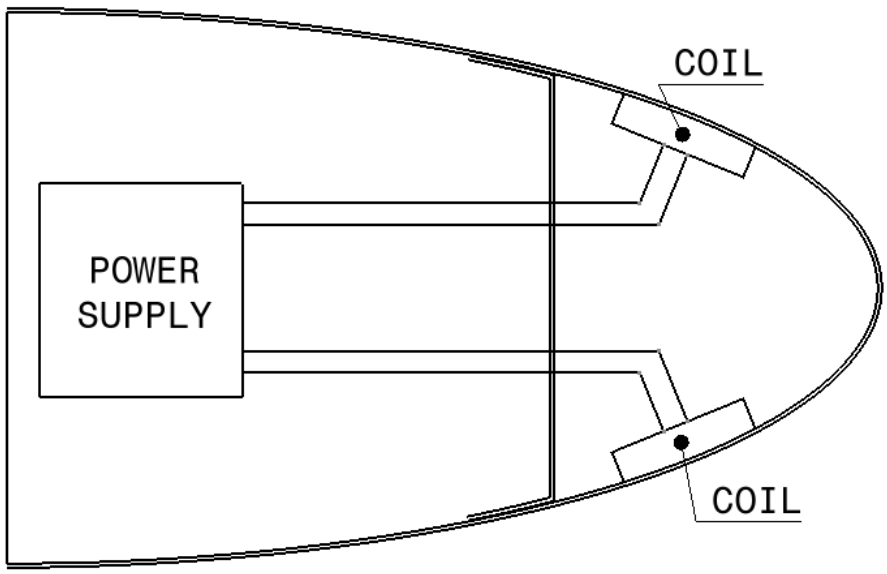

Fig.1.12 Electro-Impulse Icing Protection System layout

1.4.5 Vibrating Electro-Expulsive De-Icing System

The Electro-Impulse Icing Protection System is only capable of De-Icing functionality (no Anti-Icing function is possible) by discharging high electrical currents through conductor pairs foils in opposite directions resulting in repulsive electromagnetic fields. This causes a rapid vibration of the foils deforming the skin and consequently debonding the ice. This system shows a power consumption around 80 [W] per meter along the wing span.

The system is lifetime reliable but becomes heavy for large surfaces therefore such system has only been implemented in small airplanes [5]. A scheme of the Vibrating Electro-Expulsive IPS is shown in Fig. 1.13.

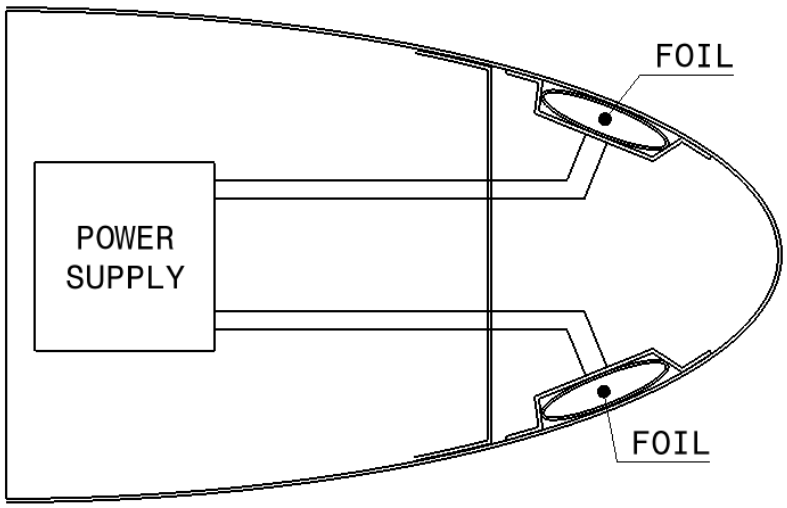

Fig.1.13 Vibrating Electro-Expulsive Icing Protection System layout

1.4.6 Deforming Electro-Expulsive De-Icing System

The Deforming Electro-Impulse Icing Protection System is only capable of De-Icing functionality (no Anti-Icing function is possible) by discharging high electrical currents through conductor pairs in opposite directions resulting in electromagnetic repulsive fields. This causes a rapid deformation of the boot surface and debonds the ice. This system shows a power consumption above 100 [W] per meter along the wing span [5].

The system is lifetime reliable but can only be implemented on a limited portion of the skin loosing the overall efficiency. A scheme of the Deforming Electro-Expulsive IPS is shown in Fig. 1.14.

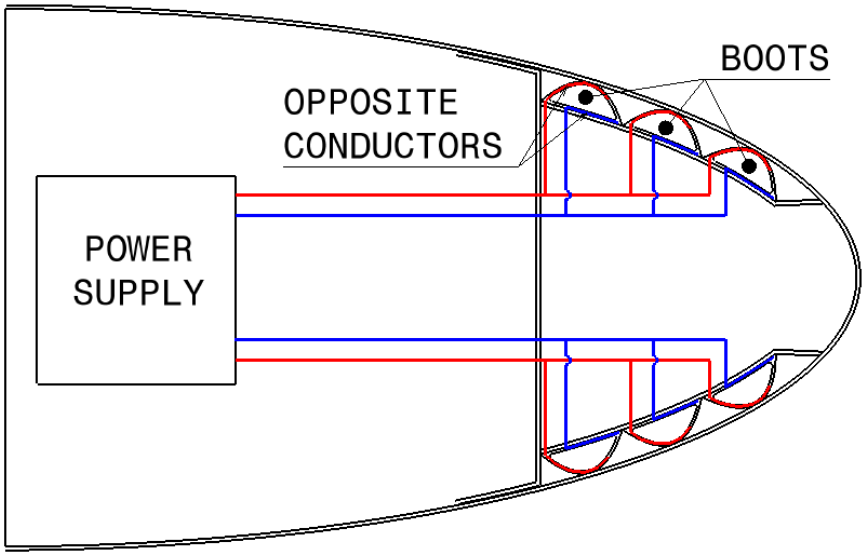

Fig.1.14 Deforming Electro-Expulsive Icing Protection System layout

1.4.7 Electrolytic De-Icing System

The Electrolytic Icing Protection System is only capable of De-Icing functionality (no Anti-Icing function is possible) by using micro-electrodes embedded into the exposed surface able to generate ice electrolysis. A DC bias generates current flow through the ice decomposing ice into gaseous hydrogen and oxygen. This reduces the surface adhesion and the gas create cracks in the ice. The power consumption can be assumed generally around 0.5÷1.0 [kW m^{-2}] when the system in on.

The system is lifetime reliable but requires a massive number of electrodes which an corrode with time and must be frequently inspected to ensure proper functionality and to avoid propagation of corrosion. A scheme of the Electrolytic IPS is shown in Fig. 1.15.

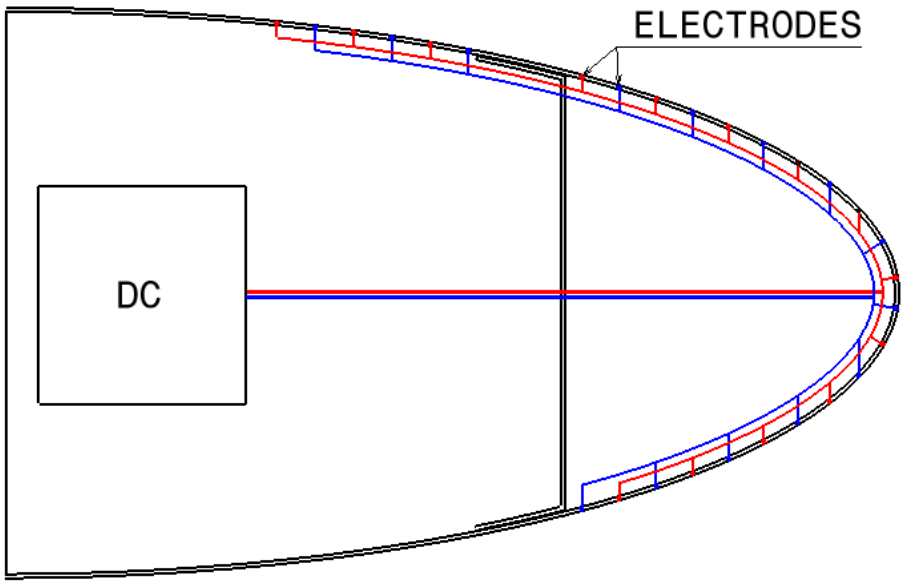

Fig.1.15 Electrolytic Icing Protection System layout

1.4.8 Microwave Ice Protection System for CFRP LE

The Microwave Ice Protection System for CFRP leading edges is capable either of De-Icing or Anti-Icing functionality by a microwave generator placed into the leading edge which is homogeneously heating the CFRP LE itself which has an high rate of microwave absorption. Due to such high rate, the efficiency of the system is extremely high with negligible losses. The typical power consumption seems to be around 20[kW] in total for a regional airplane wing but very little experimental data is available and a proper estimation of required power is today quite difficult.

The system is lifetime reliable but requires shielding of adjacent structures and systems which can result in a massive weight penalty. A scheme of the Microwave IPS for composite leading edges is shown in Fig. 1.16.

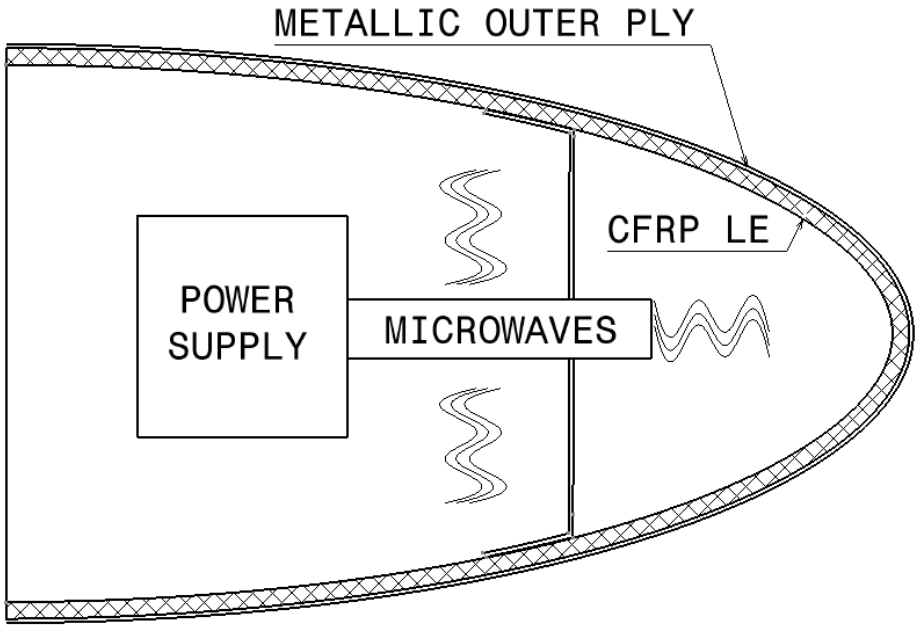

Fig.1.16 Microwave Icing Protection System layout for CFRP Leading Edges

1.4.9 Microwave De-Icing System for Aluminium LE

The Microwave Icing Protection System for aluminium leading edges is only capable of De-Icing functionality (no Anti-Icing function is possible) by heating up the already accreted ice which absorbs microwaves and melts.

Ice microwave absorption is not extremely high and therefore the efficiency of the system is typically below 70% causing a considerably loss of energy when the system is on.. The typical power consumption seems to be around 30 [kW] in total for a regional airplane wing but very little experimental data is available and even in this case a proper estimation of required power is today quite difficult.

The system is lifetime reliable but requires shielding of adjacent structures and systems which can result in a massive weight penalty. A scheme of the Microwave IPS for aluminium leading edges is shown in Fig. 1.17.

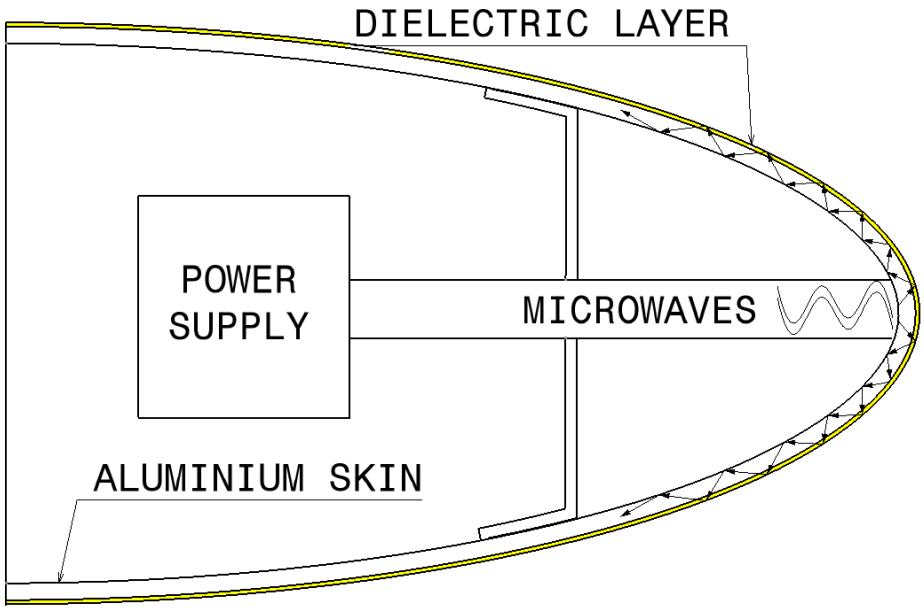

Fig.1.17 Microwave Icing Protection System layout for Aluminium Leading Edges

1.4.10 Shape Memory Alloy De-Icing System

The Shape Memory Alloy (SMA) Icing Protection System for aluminium leading edges is only capable of De-Icing functionality (no Anti-Icing function is possible) by using expansion and contraction ability of SMA materials which is producing shear forces to disbond accreted ice. The needed activation energy would be normally supplied by heating of resistors but in theory it could be taken from any available and compatible source.

The power consumption of such system could in theory be estimated around 10% of those needed by a conventional system (pneumatic or bleed air) but very little data is available and nevertheless such system would hardly be applicable to all the required areas due to the interface with the main wing structure.

The SMA system is lifetime reliable but requires expensive and complex materials which may induce a global loss of effectiveness and applicability. A theoretical scheme of the SMA IPS is shown in Fig. 1.18.

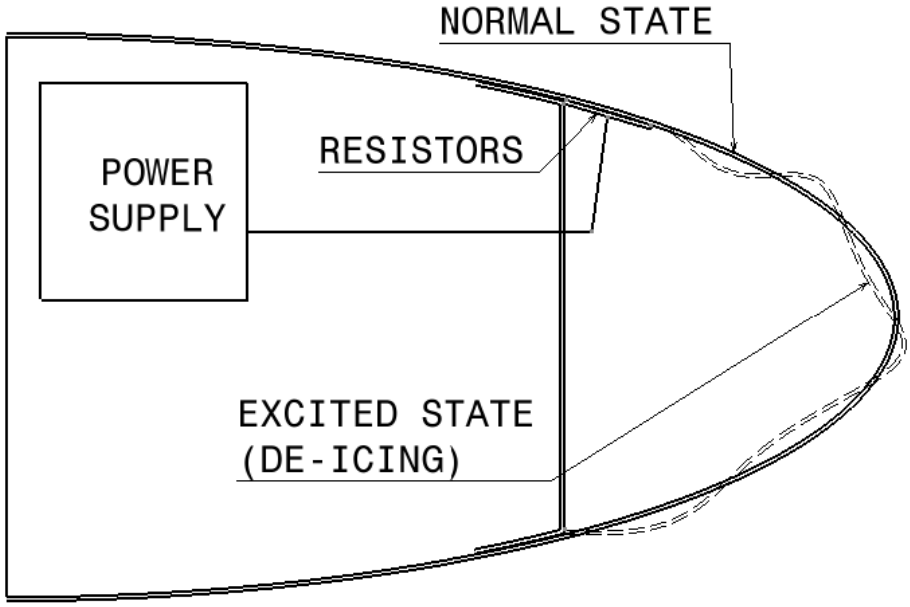

Fig.1.18 Shape Memory Alloy Icing Protection System layout

1.4.11 Electrothermal Ice Protection System

The Electrothermal Ice Protection System is capable of either De-Icing or Anti-Icing functionality by empowering electrical resistances which heat up the leading edge skin melting the accreted ice or preventing ice to form. Resistance can be bonded on the inner surface of the LE skin (metallic or composite)[66] or embedded directly into the matrix of a composite LE.

Several applications can be found in literature concerning electrically heated metallic LE but few aircraft manufacturer adopted this solution because pneumatic and air-bleed systems are more effective for metallic skins [9][12][21]. Pneumatic and Air-bleed IPSs are not applicable to composite leading edges and therefore the Electrothermal IPS may play a fundamental role for future aircrafts provided that an evidence of feasibility is proven. In this sense the current work aims to give a contribution.

In theory, for composite materials, a metallic resistance and/or metallic coated fibers can be laid up directly into the laminate avoiding the bonding of resistors on the inner surface but limited data and publications are available on this subject [21]. Some demonstration of low

power Electrothermal IPS (LPED) has been provided using an average of only 2.0 [kW m^{-2}] but no complete certification seems to be yet achieved [5][8][17].

The current work aims to preliminarily develop an IPS which embeds a metallic resistance into the LE composite laminate evaluating the feasibility of it and creating the basis to future development of this system which within the current work will shortly called EHCLE.

The EHCLE power consumption, as will be later on shown, can be preliminarily estimated around 5.0 [kW m^{-2}] for running wet functional mode to 30.0 [kW m^{-2}] for fully evaporative functional mode, but some limitations and problems will be found as well as great opportunities for future applications and developments.

Such system, using a proper matrix, will be lifetime reliable provided that operating temperatures will never exceed the allowed limit. The large number of resistance paths will have a sensible impact on inspection intervals but optimization will be shown possible.

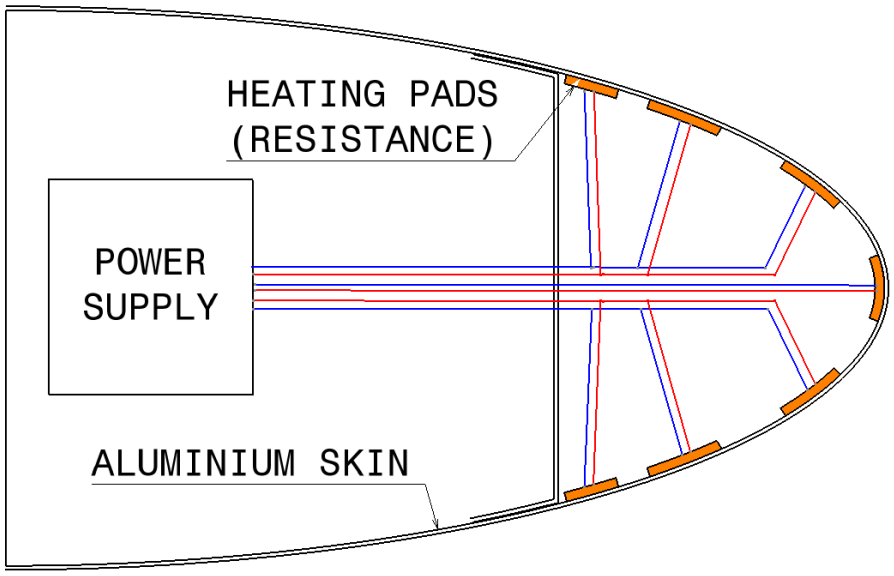

Fig.1.19 Electrothermal Icing Protection System layout for aluminium leading edges

The great advantage of the EHCLE type IPS proposed in the present work, is weight and energy saving but the key is certainly the possibility to de-ice any exposed surface by-passing almost all structural obstacles, which are normally limiting Air-bleed and Pneumatic Icing Protection Systems, increasing the overall safety. A scheme of the Electrothermal IPS for aluminium and composite leading edges are shown in Fig. 1.19 and Fig. 1.20 respectively.

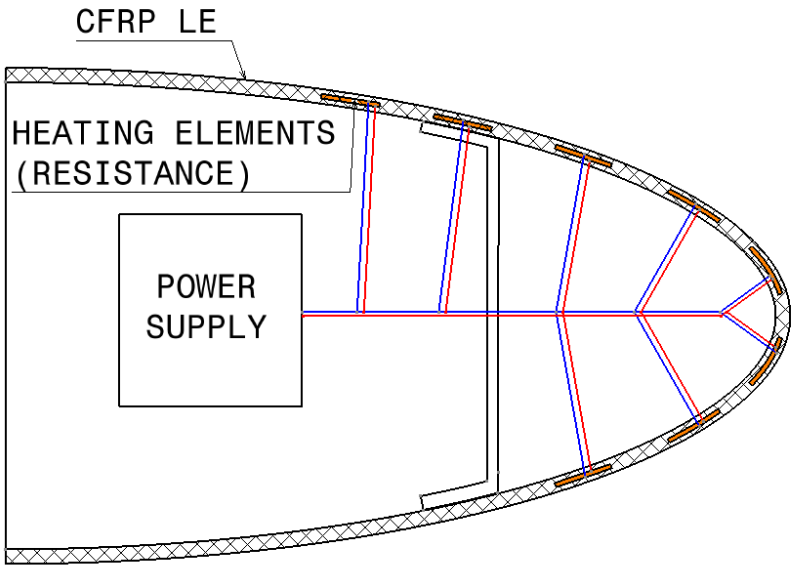

Fig.1.20 Electrothermal Icing Protection System layout for CFRP leading edges

1.4.12 Ultrasonic Icing Protection System

The Ultrasonic Icing Protection System is only capable of De-Icing functionality (no Anti-Icing function is possible) by using ultrasonic waves induced by piezo-electric transducers which propagate on the surface to be deiced. Ultrasounds generate shear stress in the leading edge skin and that breaks the bond between ice and surface.

Due to the very limited data available on this subject it is today very difficult to estimate power consumption and main characteristics of Ultrasonic IPS but it has to be considered because the technology required is available and used properly may offer advantages for aircraft manufacturers.

In theory Ultrasonic IPS can be applicable either to metallic or CFRP leading edges. A scheme of the Ultrasonic IPS for composite leading edges is shown in Fig. 1.21.

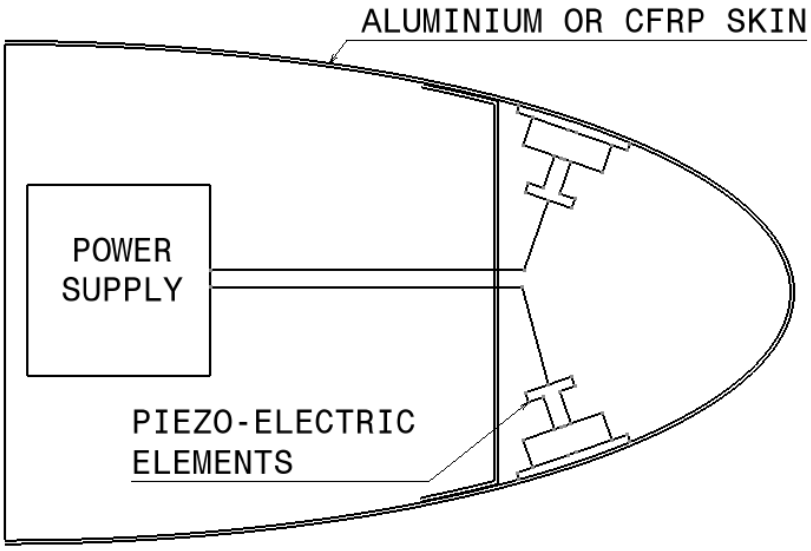

Fig.1.21 Ultrasonic Icing Protection System layout

1.4.13 Electrothermal-Expulsive Icing Protection System

The Electrothermal-Expulsive Ice Protection System is capable of either De-Icing or Anti-Icing functionality combining electrical resistances covering the impingement area of the leading edge and an electro-expulsive de-icing system located downstream which removes (by deformation) the runback ice by cyclic shedding.

This combination would in theory guarantee an energy saving with respect to pure Electrothermal system which covers a bigger area and works at much higher temperature to avoid runback ice.

Despite this hybrid system has been certified in the US there is a very limited concerned literature and an estimation of the real needed powers looks quite difficult because it depends on the ratio Electrothermal/Expulsive energy adopted [5].

The Hybrid Electrothermal-Expulsive system is lifetime reliable with all limitation imposed by both components. A scheme of the Electrothermal Expulsive IPS is shown in Fig. 1.22.

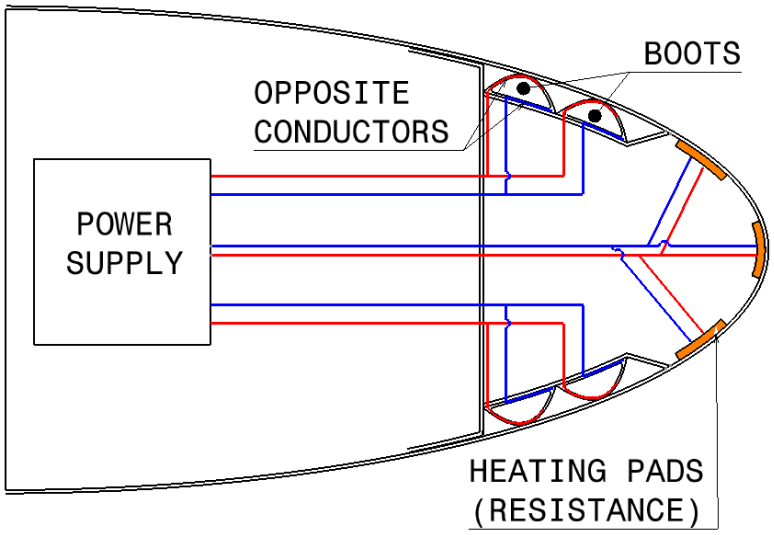

Fig.1.22 Electrothermal-Expulsive Icing Protection System layout

1.4.14 Hydrophobic Icing Protection System

The Hydrophobic Ice Protection System is today still far to be realistically applied. Super-hydrophobic materials are able to vanish the adhesion forces which allow the ice to adhere on the leading edge surfaces and therefore they would represent the most efficient, the most reliable, the lightest and the most cost-effective way of protecting aircraft surfaces. Unfortunately the development of these materials [32] begun in the recent years and first results show only potentiality and not real feasibility. In theory it is possible today to build up coating materials based on nano-structure arrays (nano-pillars) able to copy the so called Lotus effect. In practice these materials are quite weak if we look at their possibility to survive impacts from little stones, hail, sand and anything else an aircraft leading edge is facing in service. Nevertheless super-hydrophobic coatings in conjunction with classical Ice Protection Systems can give in the near future some important improvement to IPS energy saving.

1.5 IPS Functional modes

Pneumatic IPS normally are operated in "Cyclic Mode" because the boots can only be inflated instantaneously and cannot be kept pressurized because it will severely degraded the airfield around the leading edge. The pneumatic de-icing inflating cycle can vary according to specific needs and system layout, therefore it cannot be generalized.

Thermal IPS can work in three different modes as hereinafter shown:

I) Fully Evaporative Mode

The Fully Evaporative mode is achieved when: "The protected surface is heated to sufficiently elevated temperature to evaporate the impinging ice/water particles and prevent run-back ice formation". Obviously this is the most heavy working mode in terms of energy consumption and overall system and structure thermal stress. Typically the Fully Evaporative Mode is achieved keeping the surface temperature above 50[°C] but it can be higher according to the specific IPS [50].

II) Running Wet Mode

The Running Wet mode is achieved when: "The protected surface is heated to sufficiently elevated temperature to prevent the impinging of ice/water particles from freezing within the heated zone itself". This working mode requires sensibly less power than the fully evaporative one but does not guarantee that run-back ice accretes after the protected area and therefore it does not prevent a certain degradation of the airfield. Typically the Running Wet Mode is achieved keeping the surface temperature above 0[°C] but it can be higher according to the specific IPS[50].

III) Cyclic Mode

The Cyclic working mode of a thermal IPS is achieved when the system is activated cyclically to achieve only running wet working mode at regular intervals letting some ice to accrete in the meantime. Despite not very common it can be used to reduce the energy consumption.

This working mode requires higher values of power densities but for limited duration and in the end it requires less total power consumption than "continuous fully evaporative" or "continuous running wet" modes. This working mode does not prevent run-back ice accretion downstream the protected area and therefore it does not prevent a certain degradation of the airfield.

1.6 Smart Ice Protection Systems (SIPS)

Sophisticated simulations have been developed and used to study the effect of ice accretion on aircraft performance and control. On the basis real icing flights data, icing effects on aircraft have been documented and classified with a correlation to the type of icing encounter. Neural networks have been identified for use in analysing an enormous number of inputs coming from the SIPS system sensors placed all over the aero surfaces. Good results have been seen using stability and control derivatives and trim values to predict icing level. In practice within SIPS systems, using a reverse method, it is possible to identify the icing type and hazard by the effect it is producing on aero surfaces. Information essential to the pilots have been identified along with the importance of accuracy in command display information. Multi-modal feedback shows promise in communicating icing information to pilots. Initial flight deck display concepts have been proposed and are being tested at NASA. Piloted flight simulation is under development using networked computing. SIPS systems are being implemented and tested on realistic flight scenarios [18][19] with excellent results.

2 EHCLE Prototype Design and Analysis

The EHCLE prototype was preliminarily designed by means of the analytical method described in the following paragraph. Within this method I will account for material data as declared by the material supplier and I will use a linear theory for steady and unsteady heat transfer. A semi-empirical method has been developed to account for accretion, melting and evaporation of ice based in first instance on existing literature and therefore corrected on the basis of EHCLE preliminary experimental results.

2.1 Preliminary Layout

The Electrothermal IPS which was developed in the current work is based on electrical resistances embedded within a HT composite laminate as shown in Fig.2.1. As hereinafter shown the needed electrical power to run this system can be smaller than those required for metallic skins [9] due mostly to reduced losses guaranteed by the embedded heating element which transfers up 98% of the total energy to the leading edge surface. EHCLE preliminary layout was chosen responding to several needs imposed by the composite manufacturing and accounting for the overall dimension of the IFF wind tunnel where it was supposed to be tested. Hereinafter I summarize all basic parameters which have been involved in the prototype design and analysis.

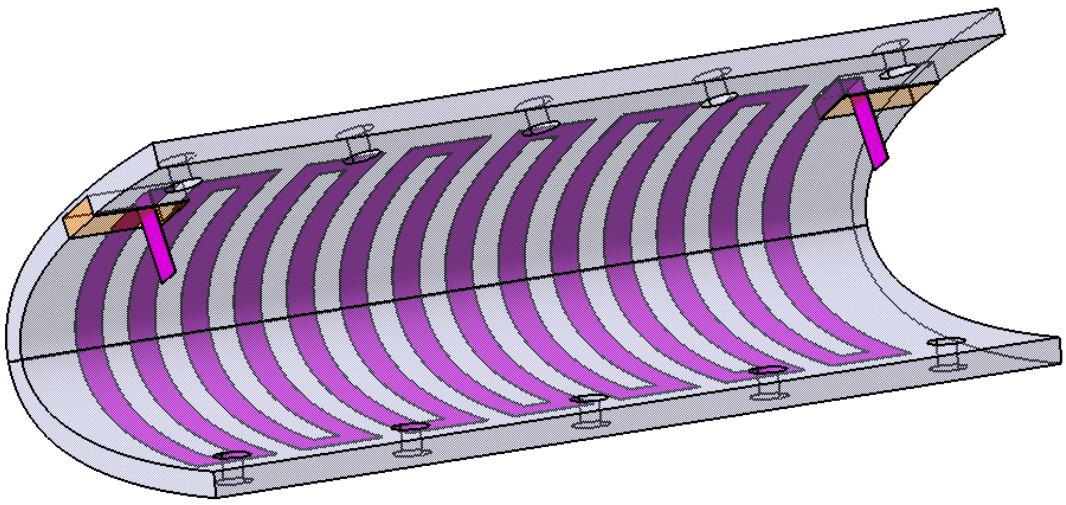

Fig.2.1 Electrically Heated Composite Leading Edge layout

Airfoil: the airfoil to use was long debating in the preliminary phase and some existing metallic NACA0012 where tested within the IFF to evaluate the uniformity and stability of the icing flow in relation to the geometrical parameters. In the end it was found that the best stable and uniform icing conditions were achieved using the NACA0012 with maximum thickness around 34[mm] and therefore it was chosen as template for the ceramic female tooling which has been therefore used for the manufacturing of the composite leading edge and main body.

The final airfoil measured therefore 34[mm] max thickness, 283[mm] in chord and 118[mm] in span (span has been chosen to proper fit within IFF test chamber).

It is necessary to point out that for the purpose of the present work the airfoil geometry is quite secondary because no aerodynamic investigations will be performed and only the thermal behaviour will be monitored under well known airflow speed and total temperature. With these premises, it is evident that the choice was made to save the manufacturing costs using an available metallic airfoil as negative avoiding to NC manufacture a dedicated one.

EHCLE layup: the thickness of the leading edge wasn't chosen to respond to structural requirements but to respond to formability requirements of the laminate within the ceramic tool. Due to the very small nose radius of the chosen airfoil, around 10[mm], some preliminary trials have been performed showing that the max thickness which could be formed without deformations and wrinkles was ranging 2.5÷3.0[mm] and the final design was therefore based on this information.

It is important to bear in mind, in fact, that the metallic leading edge sizing cases are not static nor thermal but defined to respond to bird-impact requirements. Obviously the present study does not account for it postponing such analysis to future developments, nevertheless it does not influence the general validity of the achieved results. As it will be later on shown, in fact, the ECHLE type leading edge thickness could in theory be increased on the inner side as much as needed without significant loss of system efficiency. The key parameter, in fact, is the distance of the resistance from the outer surface which can be kept adding further plies (thickness increase) only on the inner side of the leading edge where the temperature gradient is negligible.

In this sense the resistance should be positioned (within the thickness) just after the first outer ply, but it has been positioned after 3 plies of carbon either to reduce the waviness that the metallic resistance would induce on the outer surface either to guarantee a minimum

continuous thickness on the outer surface for static and impact reasons. The preliminary layup is shown in Fig.2.2 and Fig.2.3.

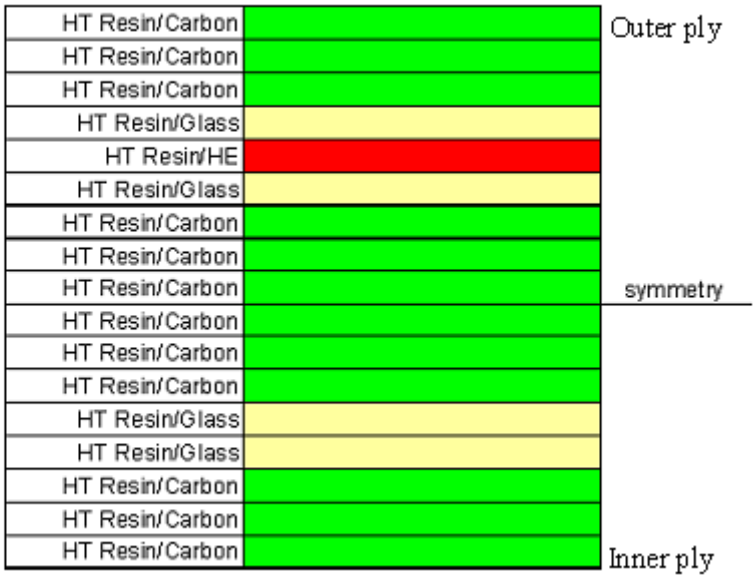

Fig.2.2 EHCLE layup cross sectioned at heating element location (Zone 1)

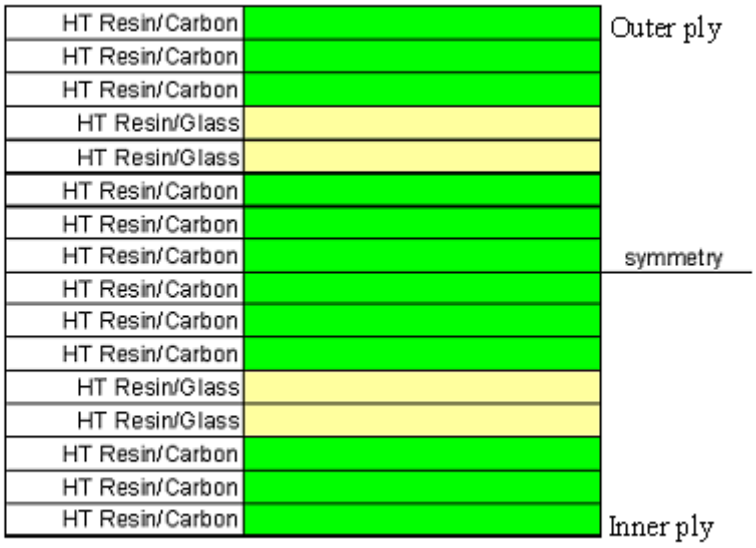

Fig.2.3 EHCLE layup cross sectioned at out of the heating element (Zone 2)

The EHCLE prototype layup has been built up according to basic composite principle of symmetry and balance. Symmetry in due to avoid distortion during curing cycle and to avoid

asymmetrical static and thermal load distribution. Nevertheless for the purpose of this work the static and/or dynamic loading has not been considered.

The glass plies which are surrounding the resistance (HE) have been introduced for the following reasons:

- To improve the adhesion around the resistance thanks to the high deformability and reduced thickness
- To guarantee the electrical insulation with respect to the conductive carbon
- To avoid galvanic corrosion between carbon and Ni-Cr

The remaining glass plies have been introduced to guarantee the global symmetry of the layup. The ply table with relevant stacking sequence and material data is shown in Tab.2.1.

Tab.2.1 EHCLE laminate Ply Table and Stacking Sequence

EHCLE Laminate	Stacking Sequence	Ply N	Material	Material Areal Weight	Orientation	Thickness Zone 1	Thickness Zone 2	Notes
				[g m^{-2}]	deg	[mm]	[mm]	
layup	1	1	HT resin / Carbon	200	45/135	0,193	0,193	
		2	HT resin / Carbon	200	0/90	0,193	0,193	
		3	HT resin / Carbon	200	45/135	0,193	0,193	
	2	4	HT resin / glass 120 style	80	0-90	0,080	0,080	
		4a	NI80CR20	na	-	0,120	0,000	
		5	HT resin / glass 120 style	80	0-90	0,080	0,080	
	3	6	HT resin / Carbon	200	0/90	0,193	0,193	
		7	HT resin / Carbon	200	45/135	0,193	0,193	
		8	HT resin / Carbon	200	0/90	0,193	0,193	
		9	HT resin / Carbon	200	0/90	0,193	0,193	
		10	HT resin / Carbon	200	45/135	0,193	0,193	
		11	HT resin / Carbon	200	0/90	0,193	0,193	
	4	12	HT resin / glass 120 style	80	0-90	0,080	0,080	
		13	HT resin / glass 120 style	80	0-90	0,080	0,080	
	5	14	HT resin / Carbon	200	45/135	0,193	0,193	
		15	HT resin / Carbon	200	0/90	0,193	0,193	
		16	HT resin / Carbon	200	45/135	0,193	0,193	
					Total Thickness	**2,75**	**2,63**	

Leading Edge protected area: the chordwise extension of any IPS is in theory related to the impingement area of water particles. In practice this area is always smaller than the area available on the leading edge and therefore to be more conservative the IPS extends, in certain cases, to all the available space which can be up to the wing front spar for a Fix Leading Edge wing (FLE) or up to the max allowed aft point of the slat for slatted wings (IPS within the slat).

In most cases the IPS extends anyway up to the erosion zone limit and for the EHCLE prototype this criteria has been chosen. The erosion zone limit is commonly defined as the area between the two lines tangent to the LE and drawn at ±15 degrees along the chord at zero AOA, as shown in Fig.2.4.

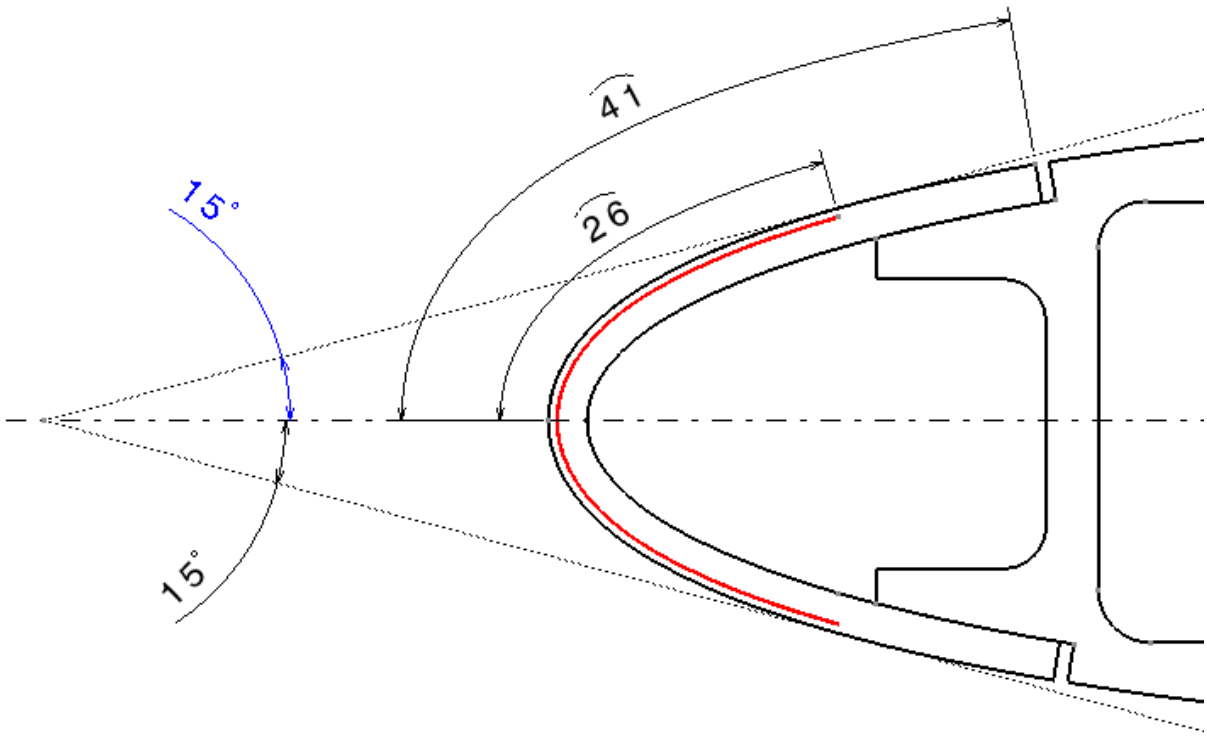

Fig.2.4 EHCLE chordwise extension, dimensions in [mm]

This common practice is due mostly to the fact that on civil aircraft there are no spanwise joints inside the erosion zone (to avoid erosion in the fastened area) and therefore just after the erosion zone there is always a spanwise joint or a spanwise fastened reinforcement (spar or stringer) which will prevent the further extension of the IPS.

2.2 Final Layout and Analytical Model

The final sizing of the EHCLE prototype accounts only for thermal load cases postponing structural considerations to future investigations on a larger scale.

The thermal load cases have been defined to cope with “running wet” and ”fully evaporative” functionality of the Icing Protection System. Obviously the sizing case was the “fully evaporative” one, able to evaporate all impinging water without runback ice accretion.

In order to design an IPS which was performing also weight wise, the Ni-Cr resistance was crafted in a regular path able to cover a certain percentage of the protected area. This percentage has been defined during the EHCLE development to guarantee a fast response of the system after switch-ON. In fact, increasing the inter-distance W_B it is evident that the temperature will reach a uniform value on the external surface after a longer time and it is also possible that it does not reach an equilibrium at all leaving on the surface different temperature zones.

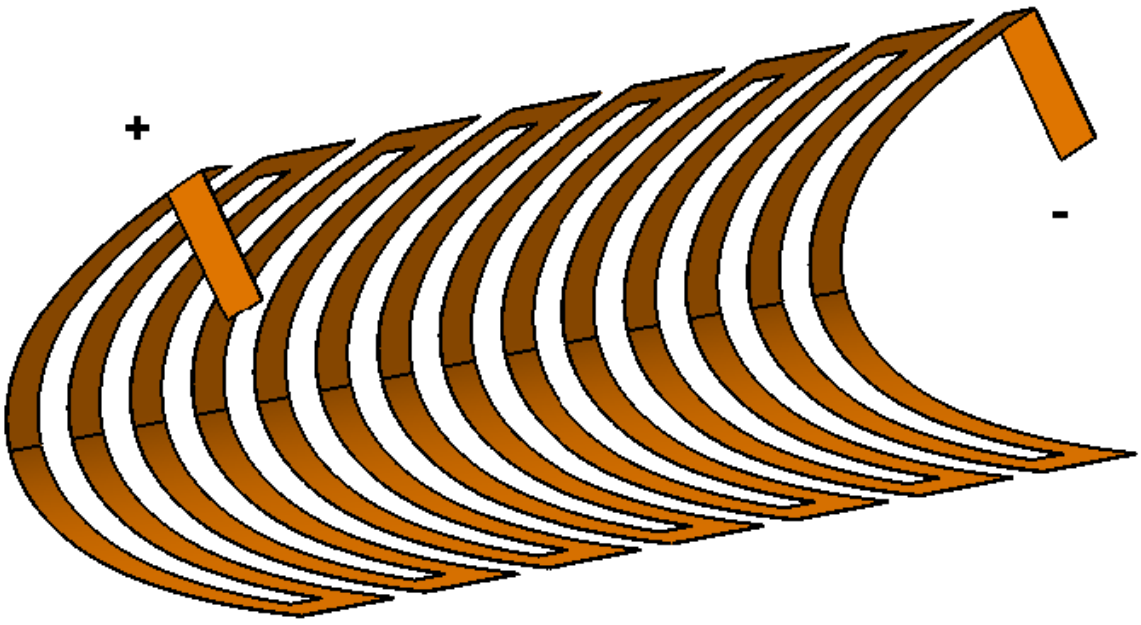

Fig.2.5 EHCLE Heating Element 3D view (resistance)

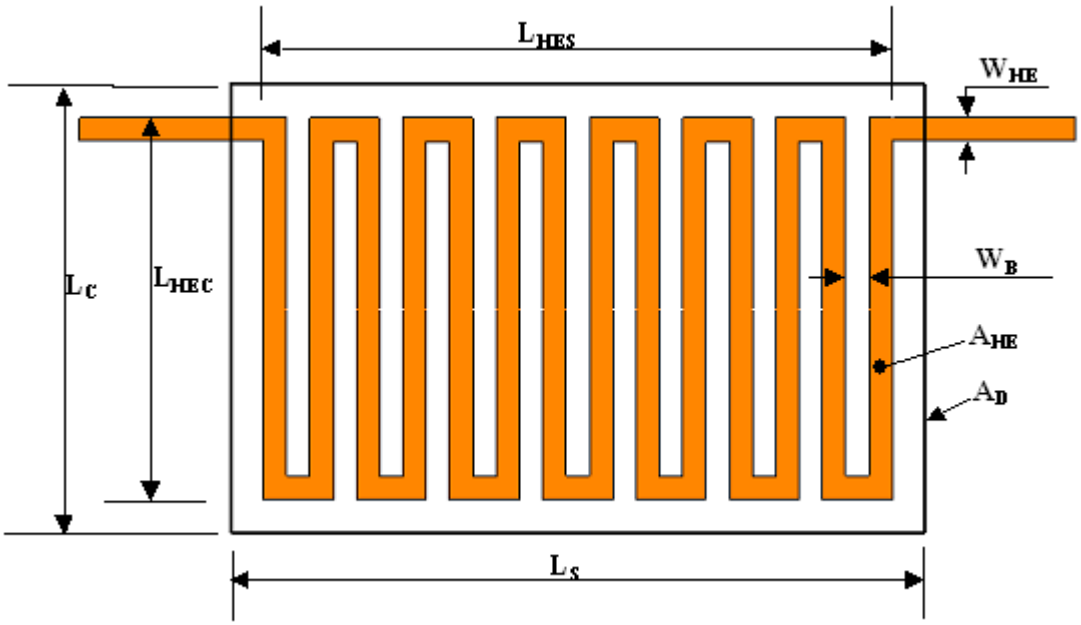

Fig.2.6 EHCLE flattened view of resistance and de-iced area A_D

Tab.2.2 EHCLE geometrical parameters

Parameters	**Symbol**	**Value**	**dim**
Deiced Area Spanwise length	L_S	101.6	mm
Heating Element spanwise length	L_{HES}	86.7	mm
Heating Element chordwise length	L_{HEC}	52.2	mm
De-iced Area	$A_D=L_S\ L_{HEC}$	5304	mm^2
Heating Element Area (flattened)	A_{HE}	2451	mm^2
Heating Element Width	W_{HE}	3.175	mm
Heating Element Inter-distance	W_B	3.175	mm
Heating Element Total Length	L_{HE}	772.1	mm
HECLE chordwise Length	L_C	80.0	mm
Heating Element cross section	S_{HE}	3.81E-7	m^2
Leading Edge Chordwise length	L_{LE}	30	mm
Filling factor	$K_F=A_{HE}/A_D$	0.46	-
Weight factor	$K_w=W_{HE}/A_D$	0.47	$kg\ m^{-2}$

Tab.2.3 EHCLE Laminate parameters

Parameters	**Symbol**	**Value**	**dim**
Carbon ply thickness	τ_C	0.193	mm
Glass ply thickness	τ_G	0.080	mm
Laminate total thickness	τ_{LAM}	2.64	mm
Laminate thermal capacity	c_{LAM}	1100	J kg^{-1} K^{-1}
Laminate thermal conductivity	λ_{LAM}	0.50	W m^{-1} K^{-1}
Laminate density	ρ_{LAM}	1300	kg m^{-3}
Laminate thermal diffusivity	α_{LAM}	3.50E-7	m^2 s^{-1}
Laminate CTE	CTE_{LAM}	12 E-06	K^{-1}
Laminate weight	W_{LAM}	18.2	g

Tab.2.4 EHCLE Heating Element parameters (Ni80-Cr20)

Parameters	**Symbol**	**Value**	**dim**
Heating Element thickness	τ_{HE}	0.12	mm
Heating Element Resistivity	r_{HE}	1.08E-06	Ω m
HE thermal conductivity	λ_{HE}	11.30	W m^{-1} K^{-1}
HE thermal capacity	c_{HE}	450	J kg^{-1} K^{-1}
Heating Element density (Ni80Cr20)	ρ_{HE}	8400	kg m^{-3}
Heating Element CTE	CTE_{HE}	13 E-06	K^{-1}
Heating Element weight	M_{HE}	2.5	g

Hereinafter the EHCLE global heat exchange analytical model scheme which has been built up taking a spanwise section and considering only one of the elementary constituents which the section itself is made of.

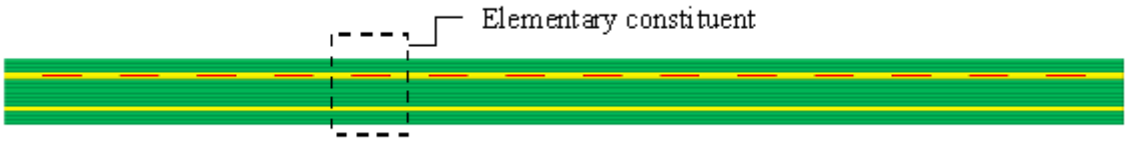

Fig.2.7 EHCLE typical spanwise section

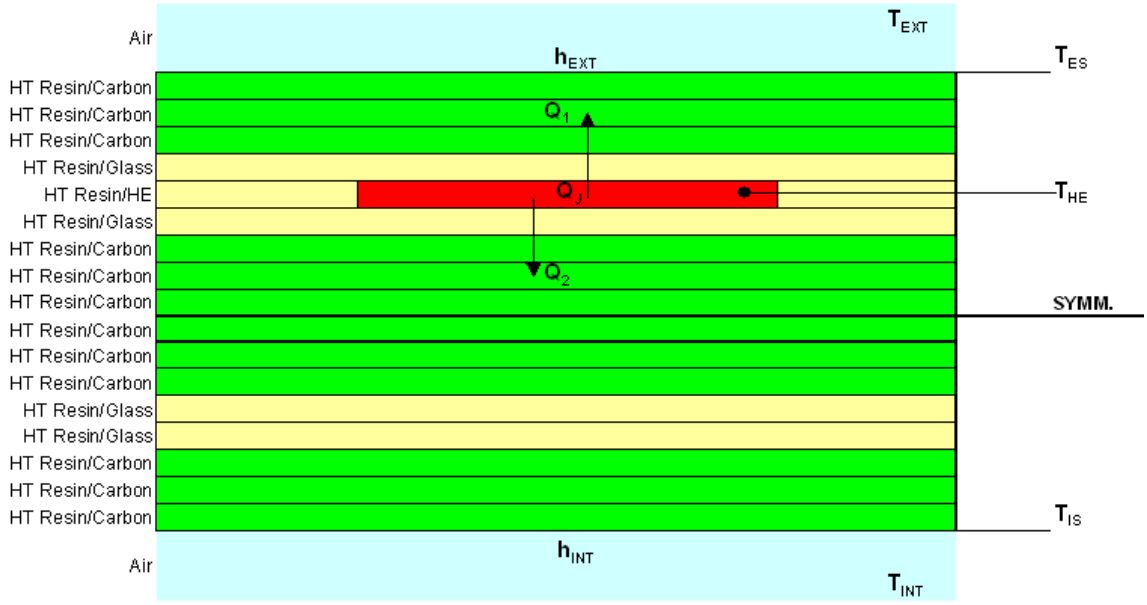

Fig.2.8 EHCLE elementary constituent

Within this scheme:

h_{EXT} is the convection coefficient on the external surface due to the icing flow comprehensive of air and water contributions [W m^{-2} °C^{-1}]

h_{INT} is the convection coefficient on the internal surface due to natural convection in air [W m^{-2} °C^{-1}]

T_{ES} is the external surface temperature of the EHCLE prototype [°C]

T_{HE} is the heating element (resistance) temperature of the EHCLE prototype [°C]

T_{IS} is the internal surface temperature of the EHCLE prototype [°C]

T_{EXT} is the external flow total temperature [°C]

T_{INT} is the air temperature within the EHCLE prototype inner cavity [°C]

Q_J is the electrical power density produced by the heating element [Wm^{-2}]

Q_1 is part of ***Q_J*** which is transferred to the leading edge external environment [Wm^{-2}]

Q_2 is part of ***Q_J*** which is transferred to the leading edge internal environment [Wm^{-2}]

Power densities Q_1 and Q_2 are directly proportional to the heat exchanged on each side and therefore, assuming negligible losses, we can write the basic relation:

$$Q_J = Q_1 + Q_2 \tag{2.1}$$

Equation (2.1) is indirectly defining the efficiency of the EHCLE system, E_{EHCLE}:

$$E_{EHCLE} = \frac{Q_1}{Q_J} \tag{2.2}$$

which represents the ratio between the power transferred to the external surface against the total energy supplied.

The external convection coefficient h_{EXT}. The convection coefficient h_{EXT} between the external icing flow and the external surface of the leading edge is analytically very complex to model and very often empirical formulas are used to obtain reference values. A very accurate model, in fact, would require to solve first the external aerodynamic field and then to integrate it along the affected surface for the laminar region first and the turbulent region after [22], where the laminar-turbulent transition can be evaluated in accordance with the Von Doenhoff criterion [23] using the local Reynolds number.
For the purpose of the present work empirical formulas have been used to calculate analytically the convection coefficient h_{EXT} obtaining anyway results in good agreement with the experimental results imposed by the IFF tunnel in the most severe icing condition working mode (see ITC5 in Tab. 5.1).

h_{EXT} calculation method. For the purpose of the current work, which is mainly to preliminary size the EHCLE IPS system, we will use a simplified method which is assuming that the total heat lost on the external surface is the sum of two contribution, the convective "DRY" and the convective "WET", acting in parallel. In this scheme the dry convection, driven by the

coefficient h_{CDRY}, accounts only for the external flow without the water content whilst the wet convection, driven by the coefficient h_{CWET}, accounts only for the heat lost because of the impinging water particles. Obviously this is just a simplified assumption. A rigorous method would not threat the impinging water as a convective flow but would consider the global equilibrium of the surface with variable mass of water, ice and vapor. Nevertheless we are interested in macroscopic quantities and this method returns, in this sense, sufficiently reliable results as will be later on shown.

Within the proposed scheme, being the contribution of h_{CWET} and h_{CDRY} acting simultaneously on the same surface and applying the electrical analogy, we can consider the two equivalent thermal resistances in parallel and therefore the global external coefficient h_{EXT} can be written as following:

$$h_{EXT} = h_{CDRY} + h_{CWET} \tag{2.3}$$

A basic method to account for the heat balance at the surface with impinging water particles can be found in [28], and requires the simultaneous solution of thermal and aerodynamic field problem. More detailed and sophisticated approach can be found in [34][35][36] and requires a sensible amount of experimental data to generate correlations useful for convective coefficient estimation. This method can be thereafter simplified with reasonable agreement of results through a modified Hilpert correlation [35]. The simplified approach described by equation (2.3) is in a certain way inspired by the semi-empirical correlations described in [34] [35][36] and is obviously applicable only to the cases where experimental data are available and correlation identified.

h_{CDRY} calculation method. An efficient method to evaluate preliminarily the dry external convective coefficient, h_{CDRY}, can be obtained assuming the leading edge of chordwise length L_{LE} equivalent to a cylinder of diameter $D=L_{LE}$ and multiplying the convection coefficient by an dimensionless reduction factor, C_R, given by the ratio between cylinder circumference and heating element chordwise length (effective portion of surface exposed to convective flow). Despite this method is quite empirical and simplified it returns values which are in good agreement with test results (see EHCLE preliminary dry tests). The empirical relation in this

case can be written starting from Martinelli's equation [28][33], neglecting the flat plate portions of the leading edge (top and bottom) and considering only the cylinder of diameter $D=L_{LE}$ and reducing it by the factor hereinafter described.

$$h_{CDRY} = \frac{1.14\,\lambda_{AIR}\,R_e^{0.5}\,P_r^{0.4}}{L_{LE}}\,C_R \tag{2.4}$$

where C_R is the convection area reduction factor calculated as following:

$$C_R = \frac{\pi\,L_{LE}}{L_{HEC}} = 0.55 \tag{2.4a}$$

where :

λ_{AIR} is the thermal conductivity of the air at temperature T_{LF}

$R_e = \frac{\rho V L_{LE}}{\mu}$ is the local Reynolds number calculated at temperature T_{LF}

L_{LE} is the reference length that in this case has been set as the leading edge chord length

Pr is the Prandtl number of the air at temperature T_{LF}

T_{LF} is the so called “liquid film temperature” which can be assumed as the arithmetical average of T_{EXT} and T_{ES}

For the EHCLE preliminary sizing T_{ES} was not known because it is an equilibrium temperature and it has to be evaluated otherwise or experimentally measured. In our case it was preliminarily evaluated according to reference literature for similar icing flows and then T_{LF} was obtained from it. Obviously this method was adjusted after the preliminary tests of the EHCLE prototype using T_{ES} values as obtained from the experimental results. Nevertheless the h_{CDRY} do not vary enormously within the temperature range considered (10< T_{ES} <100 [°C]). In fact, despite the EHCLE prototype was sized assuming h_{CDRY} evaluated at a too high temperatures, T_{LF} =50[°C] for the fully evaporative case and at T_{LF} =25[°C] for the running wet case, it was anyway possible to correct the analytical model after the first

experimental results without significant variations of the foreseen performance. Hereinafter I will refer only to the corrected version of the analytical model, where h_{CDRY} is evaluated at T_{LF} =25[°C] for the fully evaporative case and at T_{LF} =5[°C] for the running wet case.
The above shown method returned for the given conditions a value of h_{CDRY} = 172[$Wm^{-2}°C^{-1}$] for the fully evaporative case and at h_{CDRY} = 163 [$W\ m^{-2}\ °C^{-1}$] for the running wet case.

h_{CWET} calculation method. For the EHCLE analytical model we will follow the simplified approach above shown using our preliminary experimental results to evaluate the ice accretion rate M_A defined as the mass of ice accreted on area A_D of the leading edge per unit time.
The mass of ice was measured running 5 times a wet tests for a duration of 4 minutes in conditions ITC5 with power-OFF and measuring both the weight of the ice shape detached from the leading edge with a light warm up of the EHCLE system and the total ice volume by measuring the ice shape geometry. The average of all the measurements has been then used for calculations. Since the ice shape was not detached completely at top and bottom end the weight measurements were corrected by an extra ice weight calculated measuring the remaining iced area times the average ice thickness left on it. This correction coefficient was always smaller than 5% of the weight of the detached ice shape. The average mass of the detached ice shape was m_A= 6.1 [g] accreted in 4 minutes which is equivalent to an average ice accretion rate of M_A= 0.025 [$g\ s^{-1}$].
Assuming that all impinging water equates the amount of ice accreted on the area A_D and imposing that all the water is evaporated we can write:

$$Q_{WET} = -M_A L_V \quad \text{(Fully Evaporative case)} \tag{2.4b}$$

$$Q_{WET} = -M_A L_f \quad \text{(Running Wet case)} \tag{2.4c}$$

where the sign minus is to indicate that the power is absorbed by the water and where:

Q_{WET} is the power absorbed by the evaporating water [W]

M_A is the mass of ice accreted on the area A_D of the leading edge per unit time [g s^{-1}]

L_V is the latent heat of vaporization of liquid water [J g^{-1}] (see Tab.2.5)

L_f is the latent heat of fusion of the ice [J g^{-1}] (see Tab.2.5)

Tab.2.5 Latent heats of water in air atmosphere at 0 [°C]

Water Latent Heats at temperature 0 [°C]		
Latent Heat type	Value [J/g]*	Description
Latent heat of condensation, *Lc*	2500	Refers to the heat gained by the air when water vapor changes into a liquid.
Latent heat of fusion, *Lf*	±333	Refers to the heat lost (-) or gained (+) by the air when liquid water changes to ice or vice versa.
Latent heat of sublimation, *Ls*	±2833	Refers to the heat lost (-) or gained (+) by the air when ice changes to vapor or vice versa.
Latent heat of vaporization, *Lv*	-2500	Refers to the heat lost by the air when liquid water changes into vapor. This is also commonly known as the latent heat of evaporation.
*Joules per gram of water		

Within the proposed scheme the water content act as a convection on the leading edge and therefore we can write:

$$Q_{WET} = - M_A L_V = h_{CWET} A_D \left(T_{ES} - T_{EXT} \right)_{FE} \qquad (2.4d)$$

$$Q_{WET} = - M_A L_f = h_{CWET} A_D \left(T_{ES} - T_{EXT} \right)_{RW} \qquad (2.4e)$$

and finally we can obtain h_{CWET}:

$$h_{CWET} = \frac{-M_A L_V}{A_D \left(T_{ES} - T_{EXT}\right)_{FE}} \quad \text{(Fully Evaporative case)} \qquad (2.4f)$$

$$h_{CWET} = \frac{-M_A L_f}{A_D \left(T_{ES} - T_{EXT}\right)_{RW}} \quad \text{(Running Wet case)} \qquad (2.4g)$$

where T_{EXT} is known and for T_{ES} we can use the same values adopted for the evaluation of T_{LF} in the h_{CDRY} calculation above shown.

The shown method for h_{CWET} calculation returned for the conditions given by the ITC5 icing case a value of h_{CWET} = 135 [W m^{-2} °C^{-1}] for the fully evaporative case and at h_{CWET} = 50 [W m^{-2} °C^{-1}] for the running wet case.

Recalling the equation (2.3) we can now obtain the analytically calculated values of h_{EXT} which for the conditions ITC5 a value of h_{EXT} = 307 [W m^{-2} °C^{-1}] for the fully evaporative case and at h_{EXT} = 216 [W m^{-2} °C^{-1}] for the running wet case.

The above shown empirical methods yield h_{EXT} values which can differ from the measured one up to ±10% . As it will be later on described the present investigation, due to wind tunnel overall capabilities and size, is severely affected by scale factors in comparison to real cases but nevertheless it does not alter the validity of the achieved results.

The thermal conduction problem. The thermal conduction problem within the EHCLE laminate has been analytically solved using a linear model based on Fourier theory. For the purpose of the present work the radiation contribution has been neglected because within the working temperature range the radiation contribution is below 2% of the total heat exchanged.

For the conduction problem we assume for the moment steady conditions postponing the unsteady one to a later analysis with different methods. Assuming a linear distribution of temperatures, the conduction heat transfer through the laminate thickness can be generically calculated using ***Fourier's law*** as following:

$$q = -\frac{\lambda \ A}{\tau}\Delta T \tag{2.5}$$

where $\boldsymbol{q}$ is the heat transfer rate [W], $\boldsymbol{\lambda}$ is the thermal conductivity of the material considered [W m^{-1} °C^{-1}], $\boldsymbol{A}$ is the area normal to temperature gradient [m^2], $\boldsymbol{\tau}$ is the thickness of the wall [m] and ΔT is the temperature difference between the two wall surfaces[°C]. For the EHCLE problem, assuming that the temperature gradient is zero in all directions except the through-thickness one, the above shown law becomes:

$$q_1 = \frac{\lambda_{LAM}\ A_D}{3\tau_C + \tau_G}\left(T_{HE} - T_{ES}\right) \tag{2.6}$$

$$q_2 = \frac{\lambda_{LAM}\ A_D}{9\tau_C + 3\tau_G}\left(T_{HE} - T_{IS}\right) \tag{2.7}$$

where $\boldsymbol{q_1}$ and $\boldsymbol{q_2}$ are the heat rates transferred by conduction into the laminate respectively towards the external and the internal surfaces. Assuming then $\boldsymbol{Q_J}$ uniformly distributed along the area $\boldsymbol{A_D}$ and being $\boldsymbol{A_D}$ the same for all heat exchange forms involved eqs. (2.6) and (2.7) can be written as following:

$$\frac{q_1}{A_D} = \frac{\left(T_{HE} - T_{ES}\right)}{R_{C3} + R_{G1}} \tag{2.8}$$

where $R_{C3} = \frac{3\tau_C}{\lambda_{LAM}}$ and $R_{G1} = \frac{\tau_G}{\lambda_{LAM}}$

$$\frac{q_2}{A_D} = \frac{\left(T_{HE} - T_{IS}\right)}{R_{C9} + R_{G3}} \tag{2.9}$$

where $R_{C9} = \frac{9\tau_C}{\lambda_{LAM}}$ and $R_{G3} = \frac{3\tau_G}{\lambda_{LAM}}$

where the generic quantity $\boldsymbol{R_i}$ [m^2 °C W^{-1}] can be seen as an equivalent of the electrical resistance for the thermal heat transfer.

The thermal convection problem. The thermal convection problem on the outer and inner surfaces of the EHCLE laminate has been analytically solved using a linear model based on ***Newton's law of cooling*** which is hereinafter written in a general form.

$$q = h\ A\left(T_w - T_{FLUID}\right) \tag{2.10}$$

where $\boldsymbol{q}$ is the convective heat transfer rate [W], $\boldsymbol{h}$ is the convection coefficient between fluid and wall [W m^{-2} °C^{-1}], $\boldsymbol{A}$ is the area of the wall surface exposed to the convective flux [m^2] and ΔT is the temperature difference between the wall and the fluid [°C].
For the EHCLE problem the above shown law becomes:

$$q_{1C} = h_{EXT}\ A_D\left(T_{ES} - T_{EXT}\right) \tag{2.11}$$

$$q_{2C} = h_{INT}\ A_D\left(T_{IS} - T_{INT}\right) \tag{2.12}$$

where $\boldsymbol{q_{1C}}$ and $\boldsymbol{q_{2C}}$ are the heat rates transferred by convection respectively on the external and the internal surfaces. Assuming then $\boldsymbol{Q_J}$ uniformly distributed along the area $\boldsymbol{A_D}$ and being $\boldsymbol{A_D}$ the same for all heat exchange forms involved we can write (as we have done for the conduction case):

$$\frac{q_{1C}}{A_D} = \frac{(T_{ES} - T_{EXT})}{R_{EXT}} \tag{2.13}$$

where $R_{EXT} = \frac{1}{h_{EXT}}$

$$\frac{q_{2C}}{A_D} = \frac{(T_{IS} - T_{INT})}{R_{INT}} \tag{2.14}$$

where $R_{INT} = \frac{1}{h_{INT}}$

where the quantity $\boldsymbol{R_i}$ [m^2 °C W^{-1}] can be seen as an equivalent of the electrical resistance for the thermal exchange.

The global heat exchange analytical model has been therefore built up using an electrical equivalent model as shown in Fig.2.9.

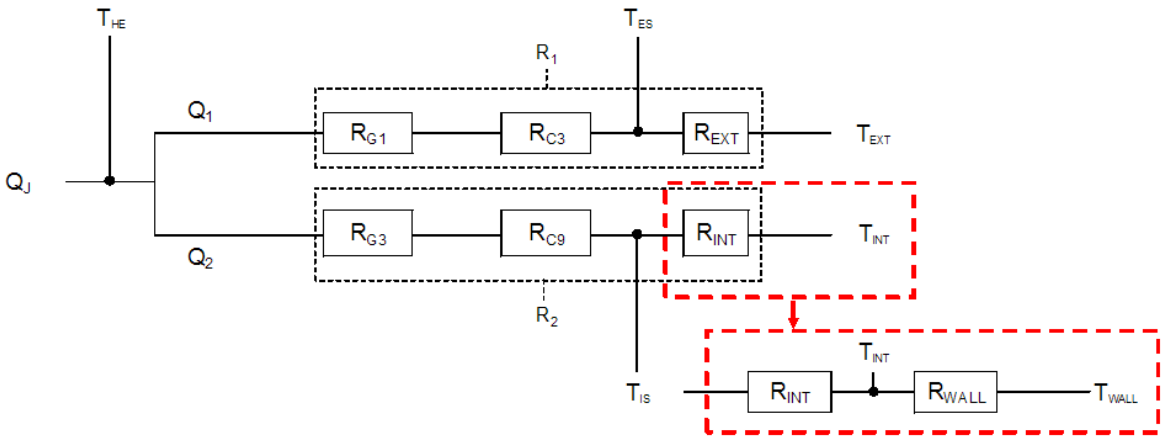

Fig.2.9 EHCLE equivalent electrical model

where:

R_1 is the total equivalent resistance of the towards the external surface [m^2 °C W^{-1}]

R_2 is the total equivalent resistance of the towards the internal surface [m^2 °C W^{-1}]

R_{EXT} is the equivalent resistance of the external surface convection [m^2 °C W^{-1}]

R_{INT} is the equivalent resistance of the internal surface convection [m^2 °C W^{-1}]

R_{WALL} is the equivalent resistance of the spar wall convection [m^2 °C W^{-1}]

R_{G1} is the equivalent resistance of the external glass ply [m^2 °C W^{-1}]

R_{G3} is the equivalent resistance of the 3 internal glass plies [m^2 °C W^{-1}]

R_{C3} is the equivalent resistance of the 3 external carbon plies [m^2 °C W^{-1}]

R_{C9} is the equivalent resistance of the 9 internal carbon plies [m^2 °C W^{-1}]

Applying the electrical equivalence to heat transfer model we can write:

$$R_1 = R_{G1} + R_{C3} + R_{EXT} = \frac{1}{h_{EXT}} + \frac{3t_C}{\lambda_C} + \frac{t_G}{\lambda_G} \tag{2.15}$$

$$R_2 = R_{G3} + R_{C9} + R_{INT} = \frac{1}{h_{INT}} + \frac{9t_C}{\lambda_C} + \frac{3t_G}{\lambda_G} \tag{2.16}$$

Recalling the equation (2.1), it can now be written as following:

$$Q_J = Q_1 + Q_2 = \frac{q_1}{A_D} + \frac{q_2}{A_D} + \frac{q_{1C}}{A_D} + \frac{q_{2C}}{A_D} \tag{2.17}$$

which accounting for eq. (2.8), (2.9), (2.13), (2.14), can be written as:

$$Q_J = \frac{(T_{HE} - T_{ES})}{R_{C3} + R_{G1}} + \frac{(T_{HE} - T_{IS})}{R_{C9} + R_{G3}} + \frac{(T_{ES} - T_{EXT})}{R_{EXT}} + \frac{(T_{IS} - T_{INT})}{R_{INT}} \tag{2.18}$$

$$Q_1 = \frac{T_{HE} - T_{EXT}}{R_1} \tag{2.19}$$

$$Q_2 = \frac{T_{HE} - T_{INT}}{R_2} \tag{2.20}$$

$$T_{HE} = \frac{R_1 R_2 Q_J + T_{INT} R_1 + T_{EXT} R_2}{R_1 + R_2} \tag{2.21}$$

$$T_{ES} = T_{HE} - Q_1 \left(\frac{3T_C}{\lambda_C} + \frac{T_G}{\lambda_G} \right) \tag{2.22}$$

$$T_{IS} = T_{HE} - Q_2 \left(\frac{9T_C}{\lambda_C} + \frac{3T_G}{\lambda_G} \right) \tag{2.23}$$

Equation (2.21) returns the equilibrium temperature of the resistance for a given power density $\boldsymbol{Q_J}$ and given external and internal convection coefficients, $\boldsymbol{h_{EXT}}$ and $\boldsymbol{h_{INT}}$. Once $\boldsymbol{T_{HE}}$ is known the temperature field can be solved everywhere but still there is the internal convection problem to be solved.

The internal convection. The internal convection coefficient $\boldsymbol{h_{INT}}$ has been calculated using a model of natural convection within the leading edge cavity and it is linked to the global model through the temperature $\boldsymbol{T_{IS}}$ and the convection coefficient $\boldsymbol{h_{INT}}$. Using an iterative method, the global model is launched starting with a tentative value of $\boldsymbol{T_{INT}}$ which we name $\boldsymbol{T_{INTT}}$ and it is run until it converges to the $\boldsymbol{T_{INT}}$.

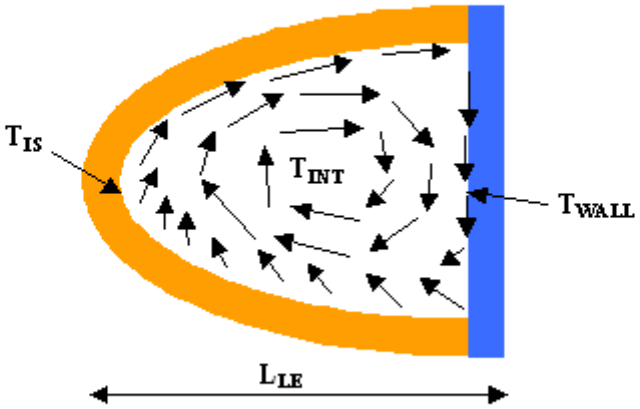

Fig.2.10 EHCLE natural convection model within the leading edge cavity

Iterations starts calculating the ***Grashoff*** numbers at temperature T_{INTT} , Gr_1 and Gr_2 , respectively at the nose and the vertical wall as following:

$$Gr_1 = \frac{g\,\beta\,L_{LE}^3}{\nu^2}\left(T_{IS} - T_{INTT}\right) \tag{2.24}$$

$$Gr_2 = \frac{g\,\beta\,L_{LE}^3}{\nu^2}\left(T_{INTT} - T_{WALL}\right) \tag{2.25}$$

where g [m s^{-2}] is gravity acceleration, β [$°C^{-1}$] is the coefficient of thermal expansion of air and ν [m^2 s^{-1}] is the kinematic viscosity of air.

Once the Grashoff numbers are known, we can calculate at T_{INTT} the ***Rayleigh*** numbers Ra_1 and Ra_2 respectively at the nose and the vertical wall as following :

$$Ra_1 = Gr_1 \,\mathrm{Pr} \tag{2.26}$$

$$Ra_2 = Gr_2 \,\mathrm{Pr} \tag{2.27}$$

The inner convection coefficients can then be calculated through the ***Nusselt*** numbers, Nu_1 and Nu_2 respectively at the nose and the vertical wall as following :

$$Nu_1 = 0.53\ Ra_1^{0.25} \tag{2.28}$$

The empirical relation (2.28) is theoretically valid for circular cavities [16] and represents with good approximation the leading edge inner cavity.

$$Nu_2 = 0.59\ Ra_2^{0.25} \tag{2.29}$$

The empirical relation (2.29) is theoretically valid for vertical walls [16] and represents with good approximation the wing front spar (excluding all the systems which are routing on it).
At this point the convection coefficients h_{INT} and h_{WALL} can be calculated respectively at the nose and the vertical wall as following :

$$h_{INT} = \frac{Nu_1\ \lambda_{air}}{L_{LE}} \tag{2.30}$$

$$h_{WALL} = \frac{Nu_2\ \lambda_{air}}{L_{LE}} \tag{2.31}$$

Using the electrical equivalence shown in Fig.2.8 we can now write:

$$Q_C = h_{INT} A_D \left(T_{INT} - T_{IS}\right) = h_{WALL} A_{WALL} \left(T_{WALL} - T_{INT}\right) \tag{2.32}$$

where Q_C [W] is the heat rate exchanged by natural convection in the leading edge cavity. From eq. (2.32) with simple operations we can isolate T_{INT} :

$$T_{INT} = \frac{h_{WALL}\, A_{WALL}\, T_{WALL} + h_{INT}\, A_D\, T_{IS}}{h_{INT}\, A_D + h_{WALL}\, A_{WALL}} \tag{2.33}$$

The value of $\boldsymbol{h_{INT}}$ is calculated through eq. (2.30) and is then used to solve the heat exchange problem of the laminate having in return the inner surface temperature $\boldsymbol{T_{IS}}$ which is then used to calculate $\boldsymbol{T_{INT}}$ through eq. (2.33).

At this point there are two possibilities:

1) $\boldsymbol{T_{INT}} = \boldsymbol{T_{INTT}}$ then the convergence has been achieved and the obtained values are correct

2) $\boldsymbol{T_{INT}} \neq \boldsymbol{T_{INTT}}$ then the convergence has not been achieved, the obtained values are not correct and the iteration shall continue with another tentative value of $\boldsymbol{T_{INTT}}$.

The calculation are started assigning a certain value to $\boldsymbol{Q_J}$ [W m^{-2}] and then plotting the temperature field. When the temperature field shows the target temperatures on the external surface $\boldsymbol{T_{ES}}$ the relevant value of $\boldsymbol{Q_J}$ is assumed as sizing case and the heating element (Ni-Cr resistance) can be designed to reproduce it according to the following relations:

$$R_{HE} = r_{HE} \quad \frac{L_{HE}}{S_{HE}} = r_{HE} \quad \frac{L_{HE}}{W_{HE}\, \tau_{HE}} \tag{2.34}$$

where $\boldsymbol{R_{HE}}$ [Ω] is the total resistance of the heating element.

$$P_T = \Delta V\, I = \frac{(\Delta V)^2}{R_{HE}} = I^2\, R_{HE} \tag{2.35}$$

where:

ΔV is the EHCLE applied DC voltage at the extremities of the resistance [V]

I is the current through the resistance[A]

P_T is the total power given to the resistance [W]

From the previous relation we can now write the average power density Q_J as:

$$Q_J = \frac{P_T}{A_D} \tag{2.36}$$

The above mentioned target temperature of leading edge external surface T_{ES} is the key for the IPS sizing. Maintaining the right temperature of the leading edge surface during icing hazards is essential for safety. In our case the maximum T_{ES} values which came out of the experimental tests for the "fully evaporative" case, in the range of 70÷80 °C, was not far from the design target which was established on the basis of available literature [50] but the material the prototype was made of is able to withstand much higher temperatures (up to 180[°C] with an acceptable margin of safety).

The results obtained using the EHCLE analytical model are summarized in the Tab.2.6 and plotted for the "Running Wet" and "Fully Evaporative" cases. All simulations have been made at T_{ES} = -20[°C], Mach number M=0.2 and liquid water content ***LWC=0.6*** [g m^{-3}] (which are representative of real ITC5 test conditions, see Tab. 5.1) with exception of functional modes identified by codes FM13, FM14 and FM15 which are DRY cases with ***LWC=0***. These last three cases have been simulated to calculate the dry convection coefficient on the external surface of the leading edge and in particular, the FM13 is a dry case with the same T_{ES} value of the "running wet" case, the FM15 is a dry case with the same T_{ES} value of the "fully evaporative" case, the FM14 is an intermediate case reported for completeness.

The functional mode for the "fully evaporative" simulated case has been identified as FM1 whilst the functional mode for the "running wet" simulated case has been identified as FM12.

In theory an infinite number of cases could have been simulated but I've only considered those relevant to present work and the Tab.2.6 has been build up in accordance with the test

campaign preliminary schedule in order to have a minimum database for numerical-experimental comparison.

Tab.2.6 EHCLE Functional Modes calculated analytically

Design Param.	Functional Modes									[dim]
	FM17	FM1 FE	FM16	FM2	FM3	FM4	FM5	FM6	FM7	
ΔV	**18,7**	**17,7**	**17,5**	**17,0**	**16,3**	**15,7**	**15,0**	**14,3**	**13,6**	v
A_D	0,005304	0,005304	0,005304	0,005304	0,005304	0,005304	0,005304	0,005304	0,005304	m^2
W_{HE}	0,00012	0,00012	0,00012	0,00012	0,00012	0,00012	0,00012	0,00012	0,00012	m
r_{HE}	1,08E-06	1,08E-06	1,08E-06	1,08E-06	1,08E-06	1,08E-06	1,08E-06	1,08E-06	1,08E-06	Ω m
W_{HE}	0,003175	0,003175	0,003175	0,003175	0,003175	0,003175	0,003175	0,003175	0,003175	m
L_{HE}	0,772	0,772	0,772	0,772	0,772	0,772	0,772	0,772	0,772	m
A_{HE}	0,002451	0,002451	0,002451	0,002451	0,002451	0,002451	0,002451	0,002451	0,002451	m^2
K_F	0,46	0,46	0,46	0,46	0,46	0,46	0,46	0,46	0,46	-
R_{HE}	2,19	2,19	2,19	2,19	2,19	2,19	2,19	2,19	2,19	Ω
I	**8,52**	**8,09**	**7,97**	**7,78**	**7,46**	**7,15**	**6,84**	**6,53**	**6,22**	A
P_T	159	143	139	132	122	112	102	93	85	W
Q_J	**30,0**	**27,0**	**26,2**	**25,0**	**23,0**	**21,1**	**19,3**	**17,6**	**16,0**	kW m^{-2}
T_{EXT}	-20	-20	-20	-20	-20	-20	-20	-20	-20	°C
LWC	0,6	0,6	0,6	0,6	0,6	0,6	0,6	0,6	0,6	g m^{-3}
Mach	0,2	0,2	0,2	0,2	0,2	0,2	0,2	0,2	0,2	-
Re	125000	130000	131000	134000	137000	140000	143000	145000	147000	-
T_{ES}	80	**69**	66	60	52	45	39	34	29	°C

Design Param.	Functional Modes									[dim]
	FM8	FM9	FM10	FM11	FM12 RW	FM13 DRY-RW	FM14 DRY	FM15 DRY-FE	-	
ΔV	**12,9**	**12,2**	**11,6**	**10,0**	**8,7**	**7,6**	**10,5**	**13,5**	**-**	v
A_D	0,005304	0,005304	0,005304	0,005304	0,005304	0,005304	0,005304	0,005304	-	m^2
W_{HE}	0,00012	0,00012	0,00012	0,00012	0,00012	0,00012	0,00012	0,00012	-	m
r_{HE}	1,08E-06	1,08E-06	1,08E-06	1,08E-06	1,08E-06	1,08E-06	1,08E-06	1,08E-06	-	Ω m
W_{HE}	0,003175	0,003175	0,003175	0,003175	0,003175	0,003175	0,003175	0,003175	-	m
L_{HE}	0,772	0,772	0,772	0,772	0,772	0,772	0,772	0,772	-	m
A_{HE}	0,002451	0,002451	0,002451	0,002451	0,002451	0,002451	0,002451	0,002451	-	m^2
K_F	0,46	0,46	0,46	0,46	0,46	0,46	0,46	0,46	-	-
R_{HE}	2,19	2,19	2,19	2,19	2,19	2,19	2,19	2,19	-	Ω
I	**5,91**	**5,60**	**5,28**	**4,57**	**3,98**	**3,47**	**4,80**	**6,15**	**-**	A
P_T	76	69	61	46	35	26	50	83	-	W
Q_J	**14,4**	**12,9**	**11,5**	**8,6**	**6,5**	**5,0**	**9,5**	**15,6**	**-**	kW m^{-2}
T_{EXT}	-20	-20	-20	-20	-20	-20	-20	-20	-	°C
LWC	0,6	0,6	0,6	0,6	0,6	0	0	0	-	g m^{-3}
Mach	0,2	0,2	0,2	0,2	0,2	0,2	0,2	0,2	-	-
Re	149000	151000	152000	154000	156000	156000	143000	130000	-	-
T_{ES}	24	20	17	12	**10**	10	40	70	**-**	°C

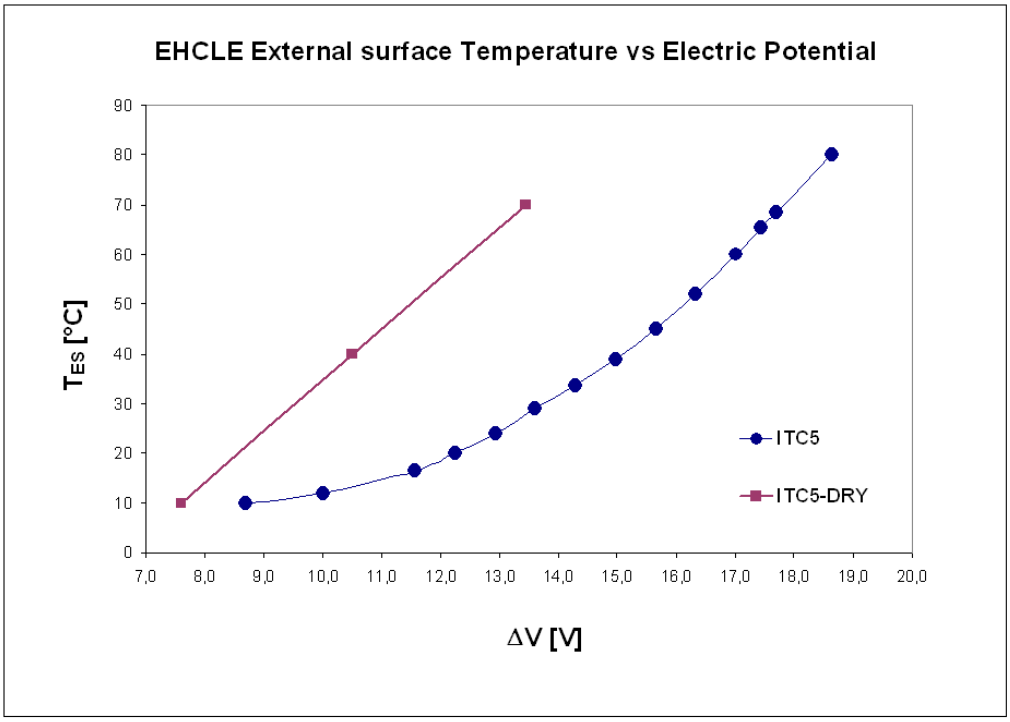

Fig.2.11 EHCLE External Surface Temperature calculated as function of the Voltage supplied for the ITC5-DRY and ITC5 flow cases

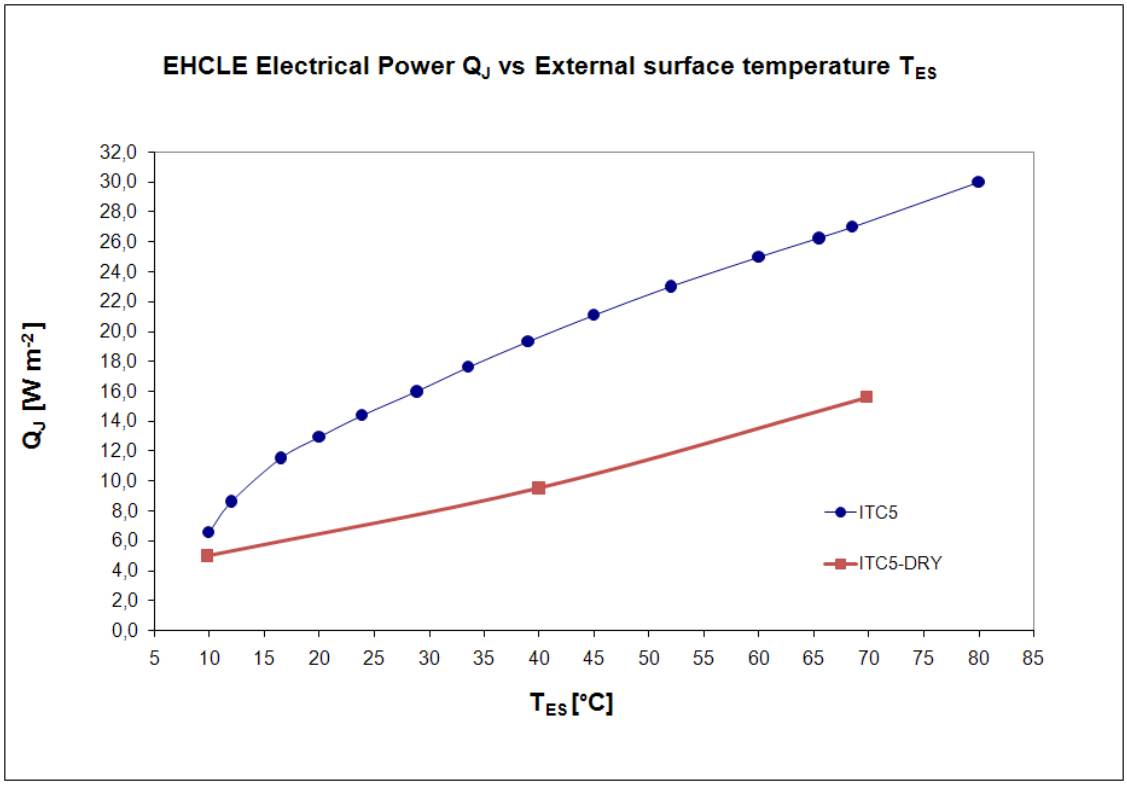

Fig.2.12 EHCLE Electrical Power density supplied calculated as function of the External Surface Temperature for the ITC5-DRY and ITC5 flow cases

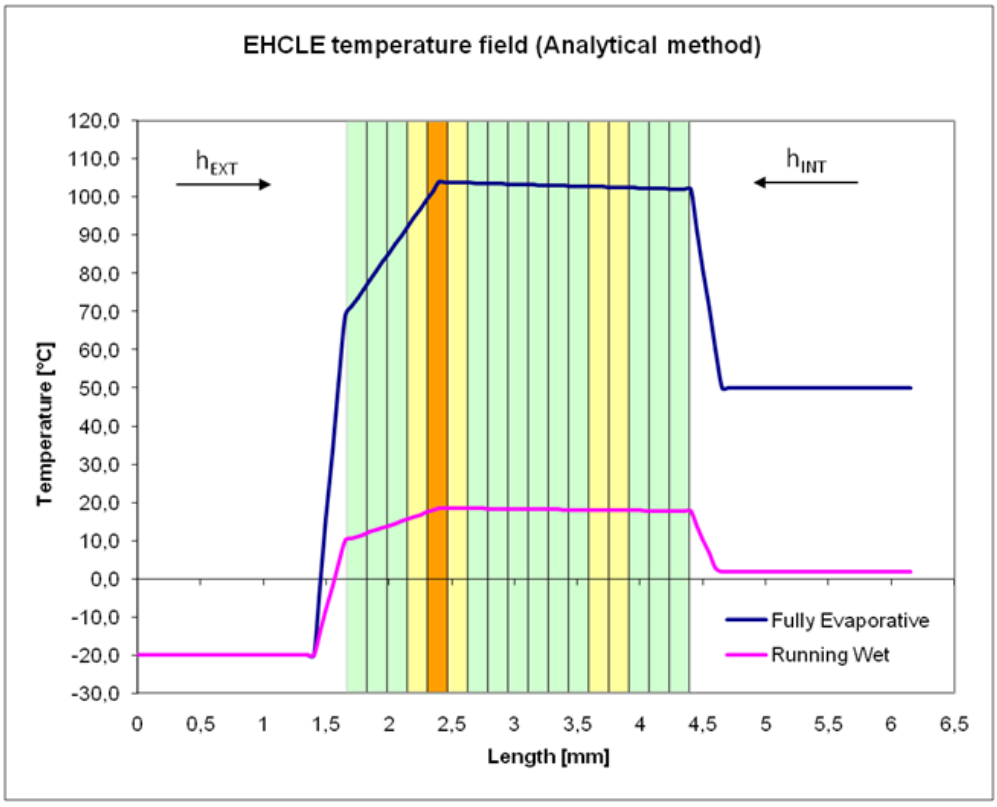

Fig.2.13 EHCLE Calculated Temperature Field (ITC5, RW/FE)

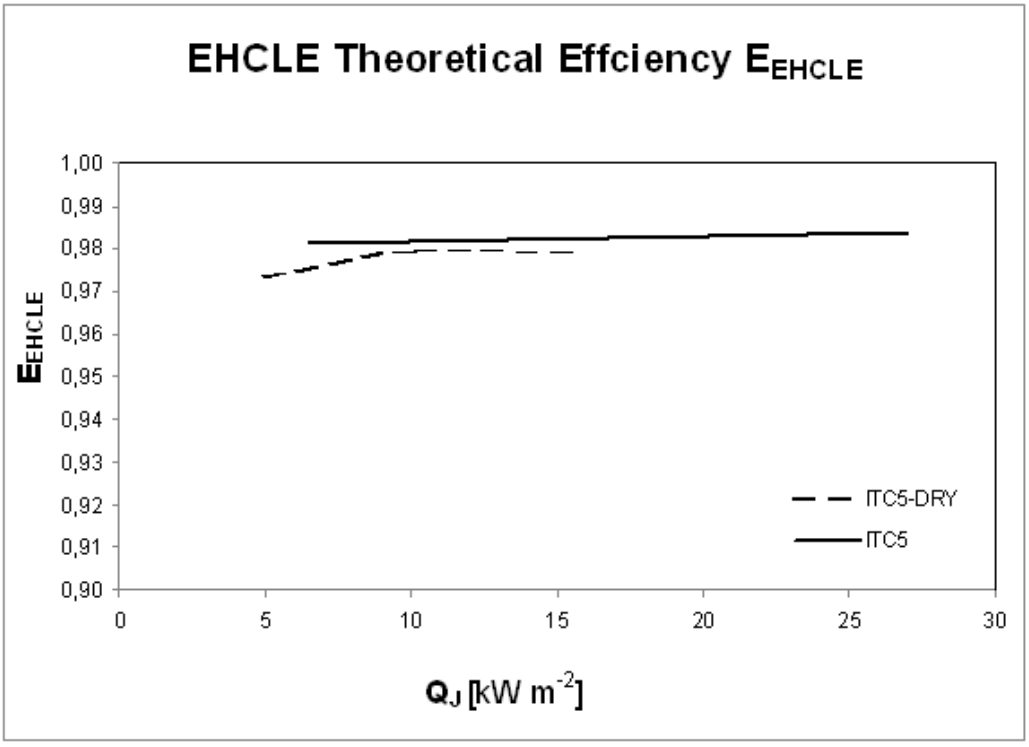

Fig.2.14 EHCLE Theoretical Efficiency E_{EHCLE} calculated under ITC5 conditions

2.3 Unsteady Analytical Model

It is necessary to point out that in several thermal IPSs, stable steady conditions are never achieved in real flights mostly because they are used for cyclic de-icing and therefore external surface temperature goes up and down following the de-icing cycles. Nevertheless it is also necessary to point out that even for IPSs which are operated in stable continuous working mode steady conditions are almost never achieved because the real icing in clouds is not uniform and the aircraft is changing continuously speed for various reasons. With this premises, it is clear that what is most important for safe operations in icing conditions is that the IPS reaction time (time to bring the surface to the target temperature for thermal IPS and time to inflate all the boots for pneumatic de-icing IPS after switch-ON) allows complete clearing of the leading edge within reasonable time to avoid the icing to be detrimental to the continuation of the flight.

How short the IPS reaction time should be has been long debated within aeronautical community but no clear statement has been given by the certification authorities mostly because there is a certain commonality in the technical solution adopted by aircraft manufacturers and therefore all certified IPS types (mostly air-bleed and pneumatic) have their own proper reaction time after switch-ON which has been proven satisfactory since more than 50 years.

As reference we can consider the reaction time of the pneumatic IPS shorter than 5 seconds even if in this case it represents the time to inflate all the boots in sequence along the wing leading edge. For the air bleed IPS there is more inertia due to the convective thermal exchange and the reaction time is also influenced by the status at switch-ON time. The IPS, in fact, can be switched-ON before any ice has accreted on the surface (because pilot knows he is flying in icing clouds) showing an average reaction time in the range of 15[s] or it can be switched-ON after some ice has already accreted on the surface (after ice detection sensor warning) showing a reaction time up to 30-40[s].

To preliminarily evaluate the time the EHCLE IPS needs to reach steady conditions after the switch-ON button has been pressed, an unsteady analytical model has been built up using Lumped Capacitance Method ($Bi<0.1$) or Heisler charts ($Bi>0.1$) pending on the ***Biot*** numbers as shown in [16]. Despite this analysis is merely theoretical it gives an important indication about the reaction time of the EHCLE system. We will analyze the simple case where the system is switched-ON before any ice has accreted on the leading edge surface and instantaneous empowering of the resistance from zero to the desired value of $\boldsymbol{P_T}$. For the experimental icing campaign the power was increased by a linear ramp and typically the

power was increased from zero to the programmed value of P_T at a rate of 3÷4 [W s^{-1}] to avoid dangerous peaks. In real aircraft it is reasonable to assume that a similar ramp shall be used.

Obviously the EHCLE reaction time which will be hereinafter calculated do not include the linear ramp but simply accounts for the thermal inertia of the system. To foresee how long the system will need to reach the equilibrium temperature on the external surface we have to account then for two contributions, first the reaction time of the system coming out of his physical nature and we need to add on top of it the chosen linear ramp which generates a further delay to the equilibrium.

For the EHCLE system the unsteady analysis shall start with the evaluation of the ***Bi*** numbers for the external convection and the internal natural convection.

Unsteady External Convection. For the EHCLE system external convection, the ***Bi*** number has been calculated as following:

$$Bi_{EXT} = \frac{h_{EXT}}{\lambda_C}\left(3t_C + t_G\right) = 0.40 \tag{2.37}$$

where the ***Bi*** number calculation has been limited to the portion of laminate located from the heating element and the external flow.

For the external convection, being ***Bi > 0.1*** to evaluate the transient to steady conditions we will use the Heisler charts provided that the ***Fourier*** number ***Fo > 0.2*** as required by the assumption made to develop this method [16]. For the current analysis this second condition has always been successfully verified when applicable (***Fo***=1.25 typically).

According to the Heisler Chart method the temperature ***T*** at time ***t*** can be calculated as hereinafter shown. First of all we need to evaluate the following ratio:

$$\frac{T_{final} - T_{EXT}}{T_{initial} - T_{EXT}} \tag{2.38}$$

where:

- for $T_{final} = T_{ES}$ and $T_{initial} = T_{HE}$ we will after obtain the time t to reach steady conditions which represents the EHCLE reaction time

- for $T_{ES} < T_{final} < T_{HE}$ and $T_{initial} = T_{HE}$ we can after plot T_{ES} from the time zero (system switch-ON) until the time t to reach the steady conditions

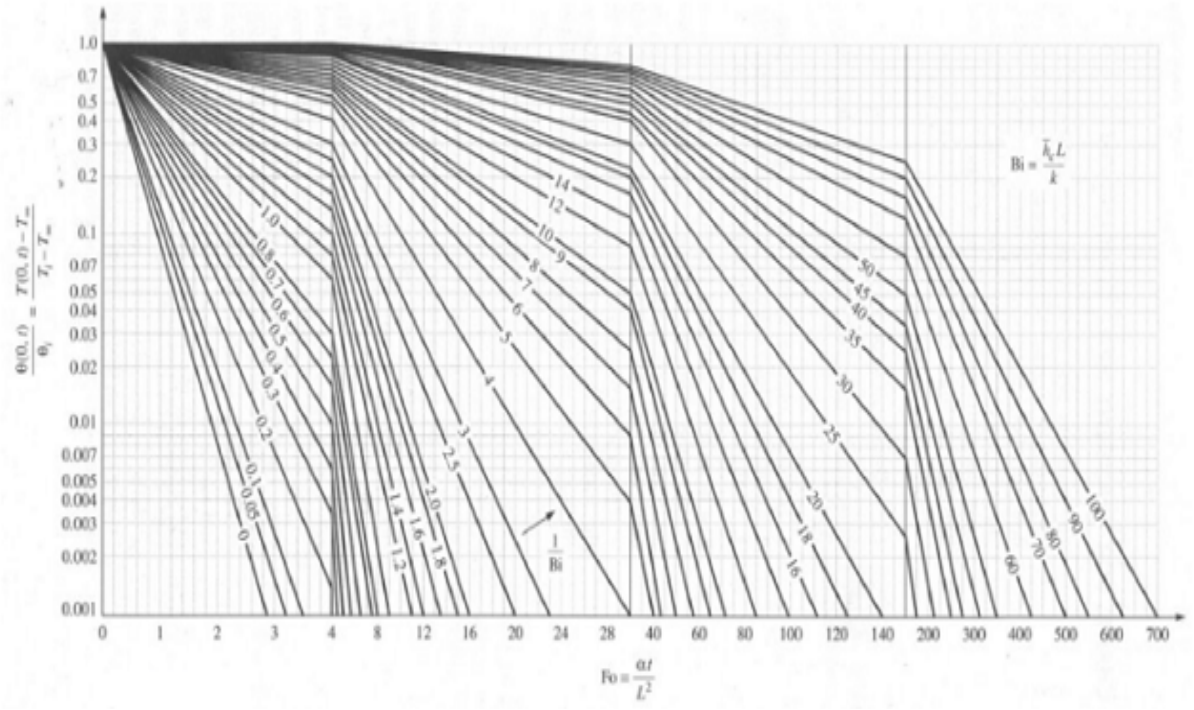

Fig.2.15 Heisler Chart

Once the ratio (2.38) is known, knowing the ratio ***1/Bi*** we obtain ***Fo*** number from Heisler Chart. Once ***Fo*** number is known we can extract the time ***t*** from ***Fo*** number definition for the external convection as follows:

$$Fo_{EXT} = \frac{\alpha_{LAM}\ t}{\left(3t_C + t_G\right)^2} \tag{2.39}$$

where:

$$\alpha_{LAM} = \frac{\lambda_{LAM}}{\rho_{LAM}\, C_{LAM}} \tag{2.40}$$

$$t = \frac{Fo_{EXT}\left(3t_C + t_G\right)}{\alpha_{LAM}} \tag{2.41}$$

Unsteady Internal Natural Convection. For the EHCLE system internal natural convection, the ***Bi*** number has been calculated as following:

$$Bi_{INT} = \frac{h_{INT}}{\lambda_C}\left(9t_C + 3t_G\right) = 0.04 \tag{2.42}$$

where the ***Bi*** number calculation has been limited to the portion of laminate located from the heating element and the internal flow.

For the internal convection, being ***Bi < 0.1*** we will use the LCM method to evaluate the transient to steady conditions. This method assumes that at any time the temperature gradient inside the material is negligible.

According to the LCM method the temperature ***T(t)*** at time ***t*** can be calculated as follows [16]:

$$T\left(t\right) = T_{EXT} + \left(T_{HE} - T_{EXT}\right)\; e^{-\frac{h_{INT}}{\rho_{LAM}\, C_{LAM}\left(9t_C + 3t_G\right)}t} \tag{2.43}$$

and therefore resolving eq.(2.43) for ***t*** we can plot the unsteady temperature from zero up to $T(t)=T_{IS}$.

Major results of the unsteady EHCLE analysis are hereinafter shown.

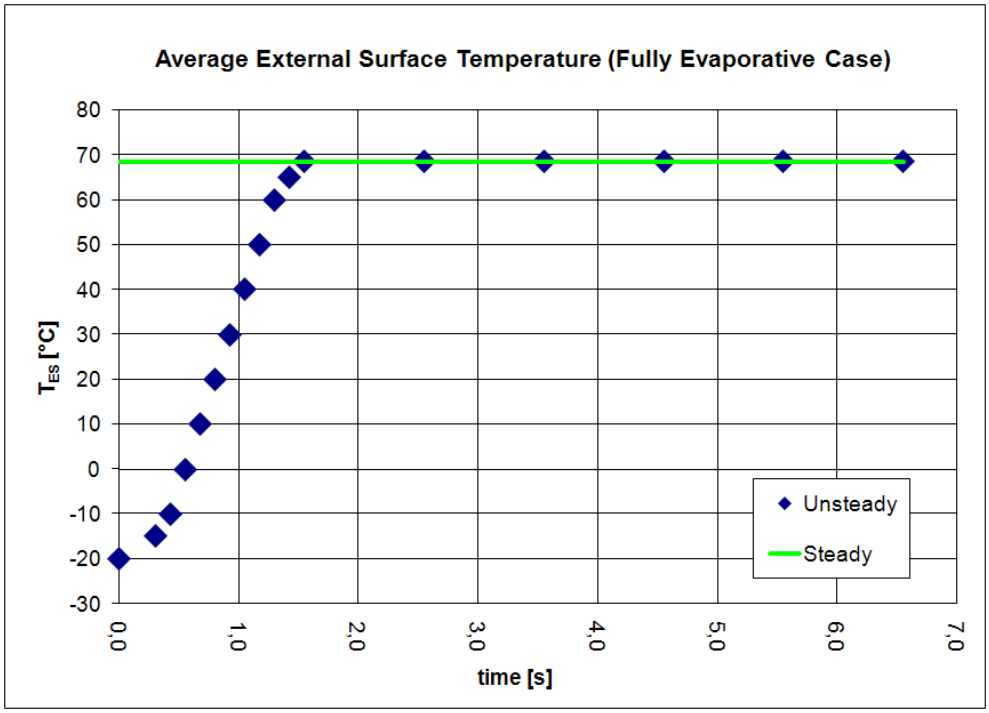

Fig.2.16 Unsteady analysis. EHCLE Average External Surface Temperature for the "Fully evaporative" case

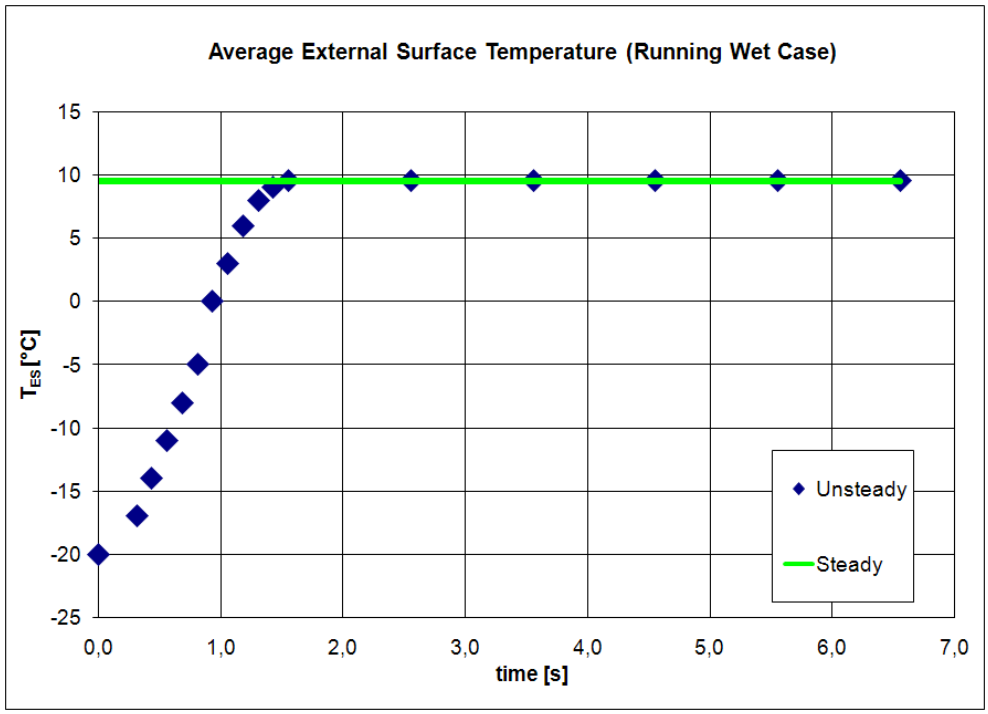

Fig.2.17 Unsteady analysis. EHCLE Average External Surface Temperature for the "Running Wet" case

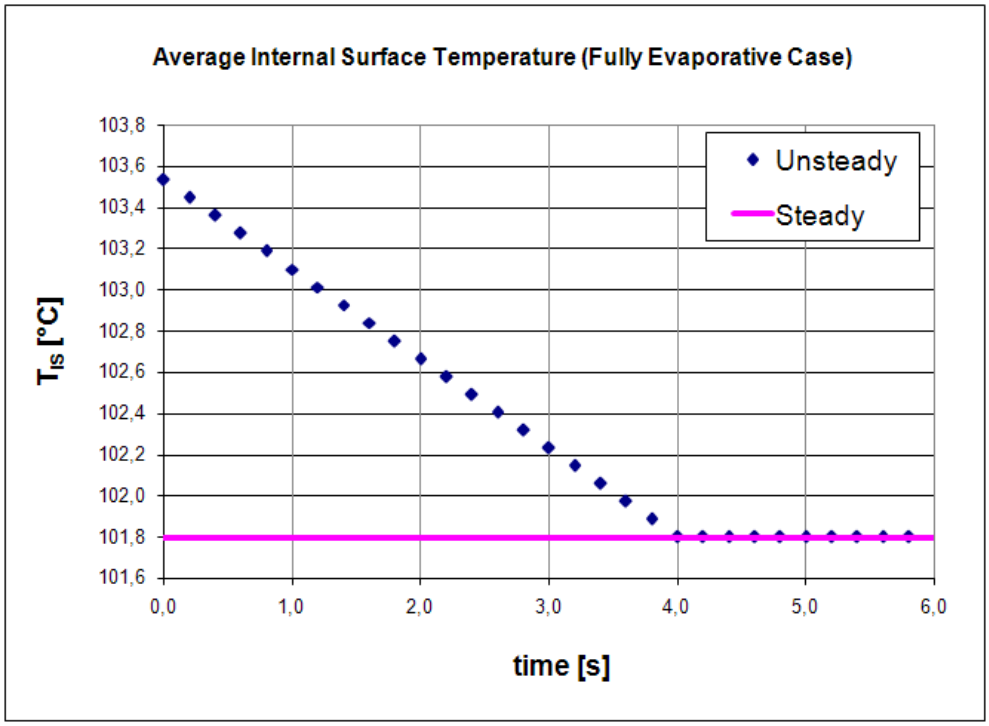

Fig.2.18 Unsteady analysis. EHCLE Average Internal Surface Temperature for the "Fully evaporative" case

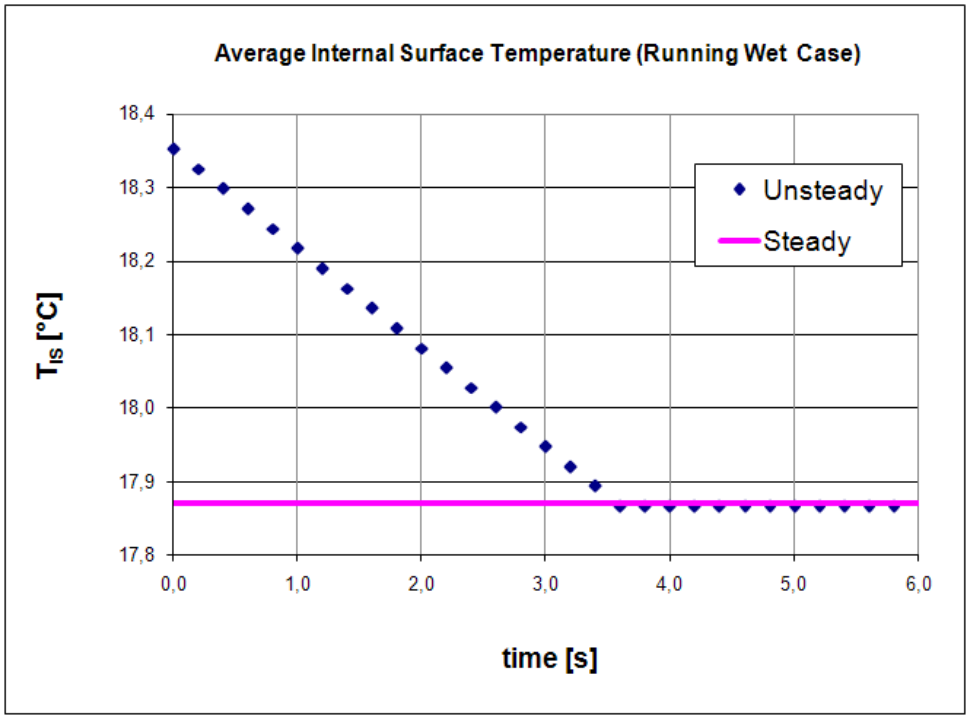

Fig.2.19 Unsteady analysis. EHCLE Average Internal Surface Temperature for the "Running Wet" case

Since the power Q_J has been assumed to be uniformly distributed over the area A_D we are considering "average temperatures" in the sense that they are averaged over the area A_D itself. In order to better analyze the unsteady behavior we identify on the real EHCLE layout the so called "worst case" location for unsteady temperature calculation as shown in Fig.2.20. This "worst case" location is defined as the most far point (or line in 3D) from the resistance path within the heating element area.

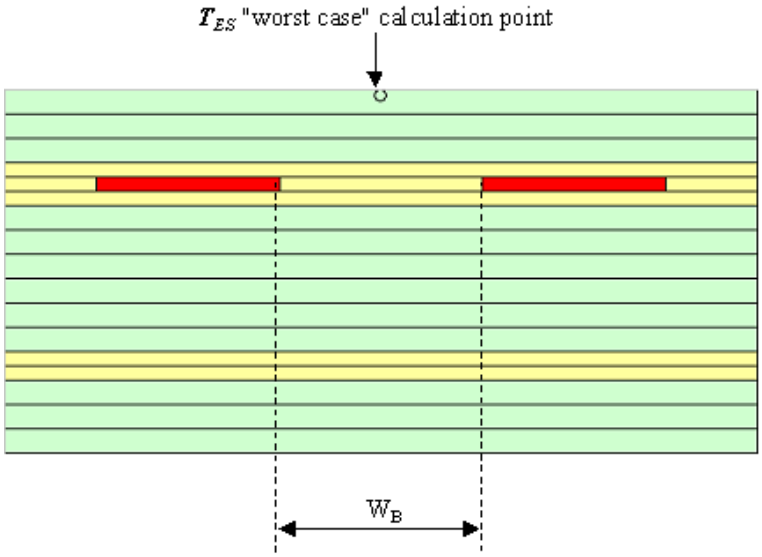

Fig.2.20 Unsteady analysis. EHCLE Average External Surface Temperature "worst case" calculation point definition

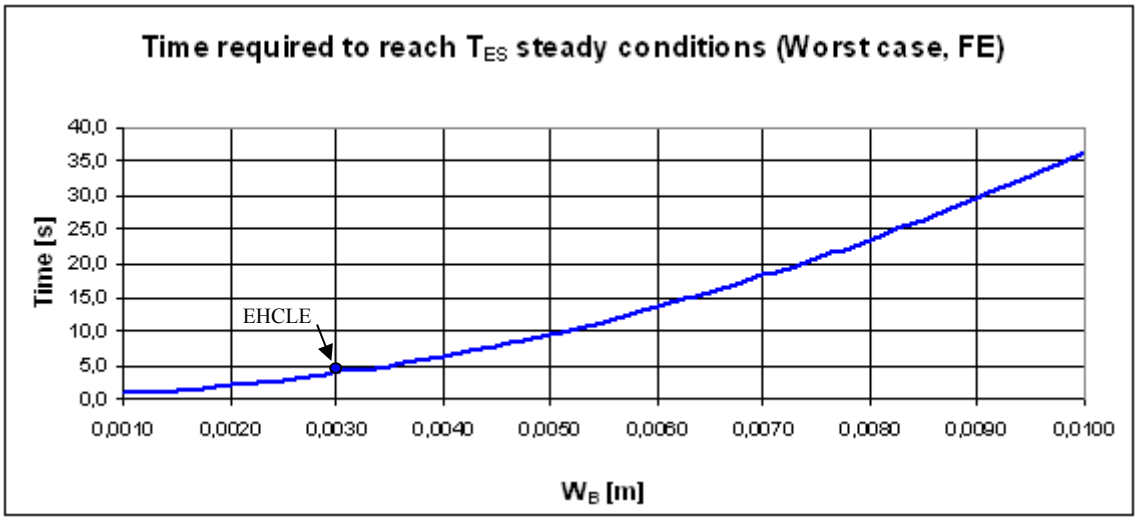

Fig.2.21 Unsteady analysis. EHCLE Time required to reach steady External Surface Temperature for the "Fully evaporative" case calculated at the "worst case" location in function of the resistance inter-space distance WB

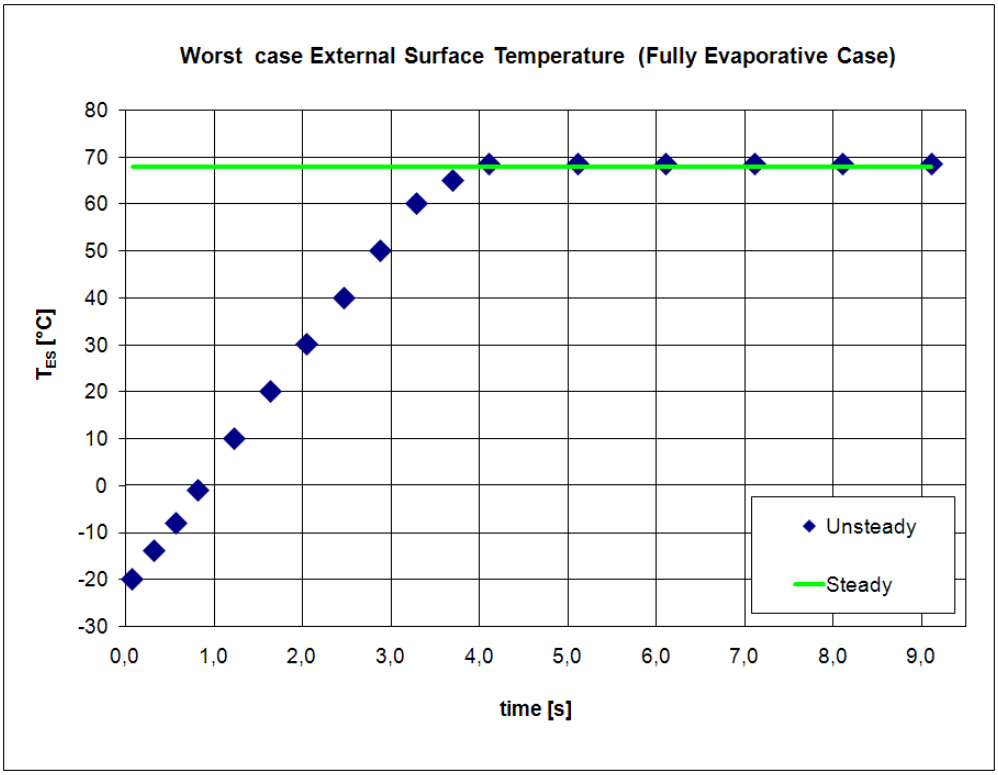

Fig.2.22 Unsteady analysis. EHCLE Average External Surface Temperature for the "Fully evaporative" case calculated at the "worst case" location

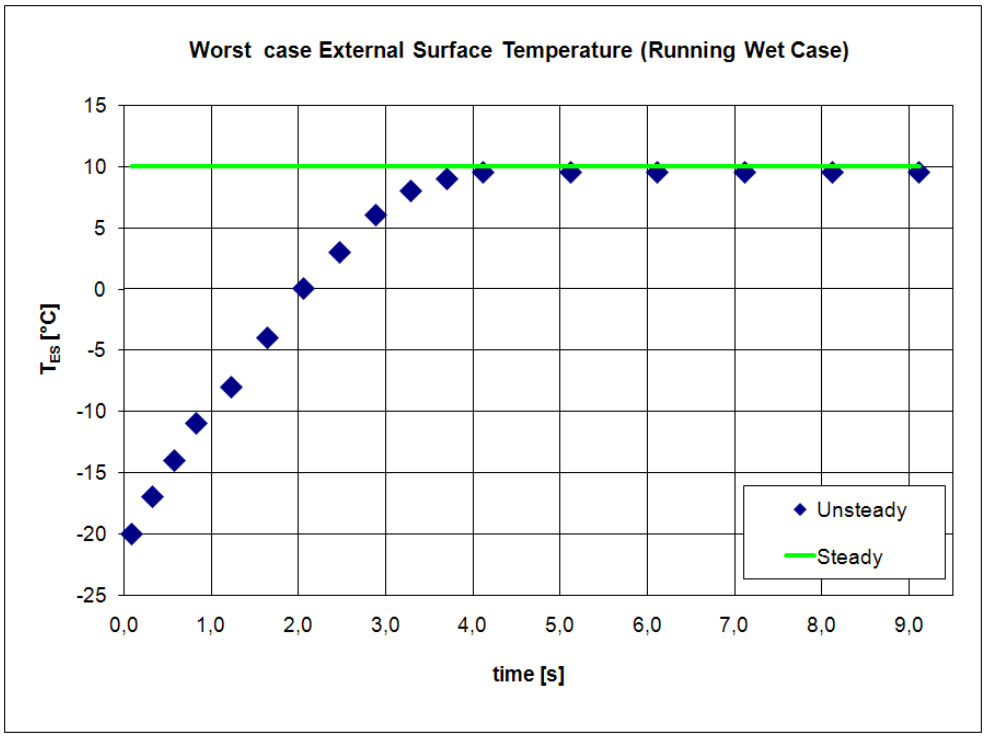

Fig.2.23 Unsteady analysis. EHCLE Average External Surface Temperature for the "Running Wet" case calculated at the "worst case" location

2.4 A critical point: Connecting the Heating Element to the Power Supply wiring

Being the Heating Element cooled by the strong external convection, the temperature of the Ni-Cr resistance do not exceed the values imposed for the integrity of the composite laminate. Nevertheless the resistance at certain point, in the EHCLE case at two extremities, need to get out of the laminate to be connected to the electric wiring whose cross section is obviously sensibly bigger than the Heating Element one so that they stay at much lower temperature. Proposing to weld the wiring on the flat resistance, which could stay then in contact with the laminate and kept cooled by the external flow would work for the experimental tests but it would be technically not correct for real cases because it would be non-reliable and hardly repairable.

For these reasons the Ni-Cr resistance shall be bent towards the leading edge cavity and get connected mechanically to the electrical wiring made out of copper (obviously the connector shall be secured to the leading edge to avoid unforeseen unplugging).

Once the resistance is bent toward the inside of the Leading edge it loses the contact with laminate and being not cooled anymore its temperature is rising up quickly, it is therefore necessary to limit the portion of heating element bent towards the inside and get it connected to the connector itself as close as possible to the laminate so it could still feel some cooling effect. Fig.2.24 shows that the heating element terminations have a cooled root in contact with laminate (imposed temperature $T=T_{HE}$), followed by a first portion of resistance in potted resin block (presumed at an average temperature of the laminate very close to T_{HE}) and rest of the resistance terminal in natural convection h_{INT} within the inner leading edge cavity. The height of the non-cooled resistance termination should be intended as the distance between the cooled resistance and the first point of contact with the connector, assuming that from the connector on the thickness of the components are sensibly bigger and therefore sensibly cooler. Despite the dimensions to play with are very small (in the range of millimeters) it was possible to design and build up a connector which reduced the exposed part of the fin to about 3[mm] before contact area. During the tests a thermocouple has been placed on both contacts (+ and -) in the resin potting area (see Fig.2.24) very close to the inner exposed part of the resistance termination, cemented to the resistance itself using the HT resin itself. Rise of temperature in the resistance termination has been monitored carefully because since the beginning this was foreseen as one of the major problem to face. For the fully evaporative case when the power supplied was 27 [kW m^{-2}] and the heating element was working at an average temperature T_{HE} =105 [°C] the contact has shown a temperature increase up to 25÷30% topping a maximum final temperature of 140[°C].

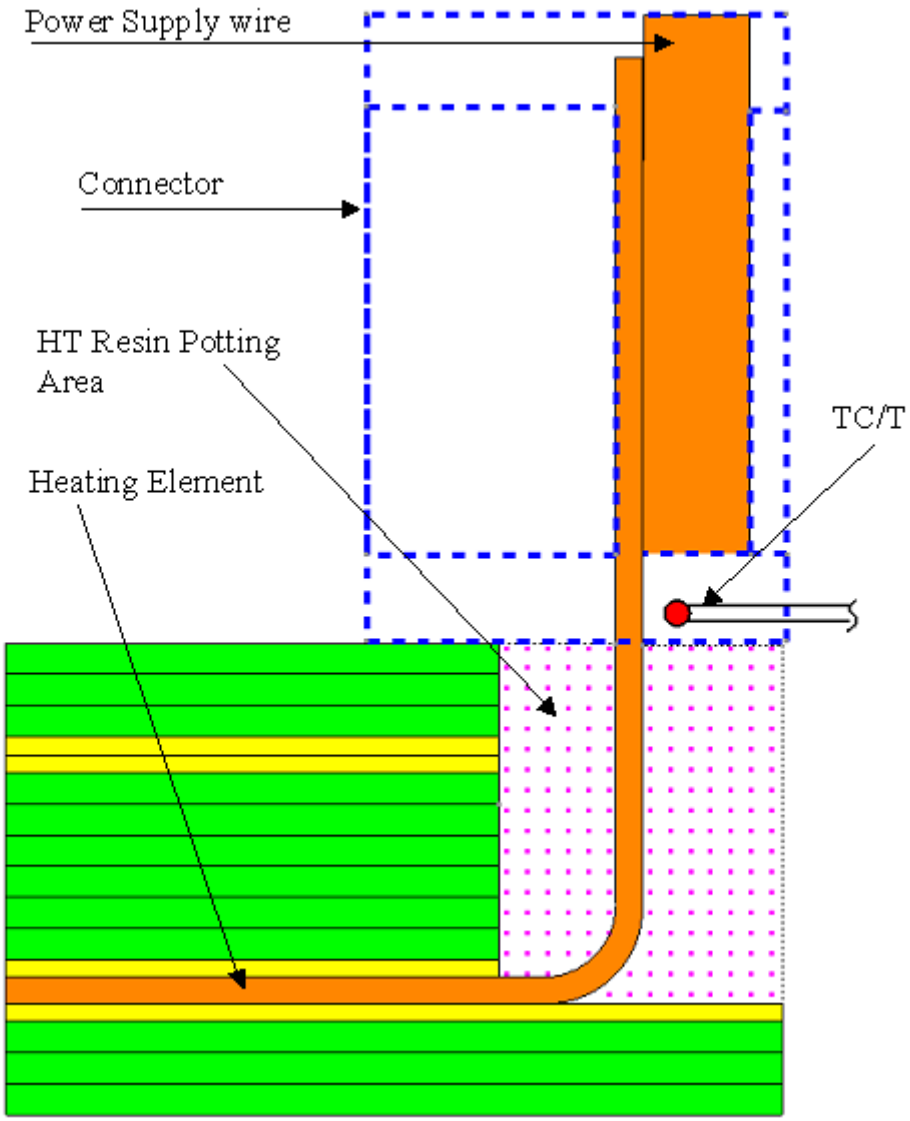

Fig.2.24 EHCLE Connection to the power supply. Temperature of the exposed portion of resistance termination has been monitored using a thermocouple T-type

3 EHCLE Prototypes and coupon Manufacturing

Based on the design described in the previous chapter, two identical composite EHCLE prototypes, EHCLE1 and ECHLE2, and one flat coupon were manufactured using the same material and the same process (Resin Infusion Technique) starting from dry plies. The EHCLE1 prototype has been used for the icing test campaign, the EHCLE2 has been kept as spare in case of malfunctions or accidents during the test campaign and the flat coupon has been used for a thermal endurance test (TET) and has been in the end cut for micrographic inspections.

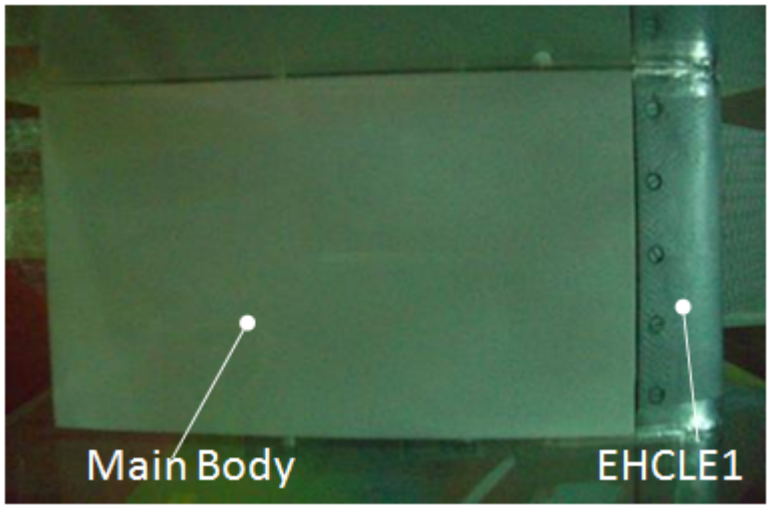

Fig.3.1 EHCLE1 prototype assembled

3.1 Materials Selection

As previously mentioned, the raw materials were selected on the basis of their properties but accounting for market availability and budget. The HT resin based on modified epoxy and basic carbon and glass fibers were selected according to the mentioned criteria as shown within the following table.

3.1.1 HT Resin

The High Temperature resin choice has been by far the most important and critical decision made at beginning of the project. Three resin types were evaluated in terms of thermal and

structural capabilities and cost effectiveness. Bismaleimide resins (BMI) resulted too difficult to process and nevertheless not cost-effective. Phenolic modified resins also showed processability and cost-effectiveness problems and therefore the modified epoxy resin type EP/Bisphenol-A/Epichlorhydrin was chosen and ordered for prototype manufacturing. Despite this resin requires and HT hardener and double curing process (low temperature curing and high temperature post-curing) it showed thermal properties in line best expectation and by far the easiest processability. The resin has a light yellow appearance after low temperature curing cycle which can be performed at 60÷100[°C] and a light brown appearance after high temperature post-curing cycle which can be performed at 200÷240[°C].

3.1.2 Carbon Fabrics

The carbon plies used for the manufacturing of prototypes and coupon were cut from a roll (see Fig.3.2) of dry carbon fabric 6K twill, areal weight of 200[g m^{-2}] and average cured thickness of 0.193[mm]. For cutting and handling of the dry layup the carbon sheet was bindered with HT resin applied in a quantity equivalent to around 2% of the final resin amount needed for the complete manufacturing.

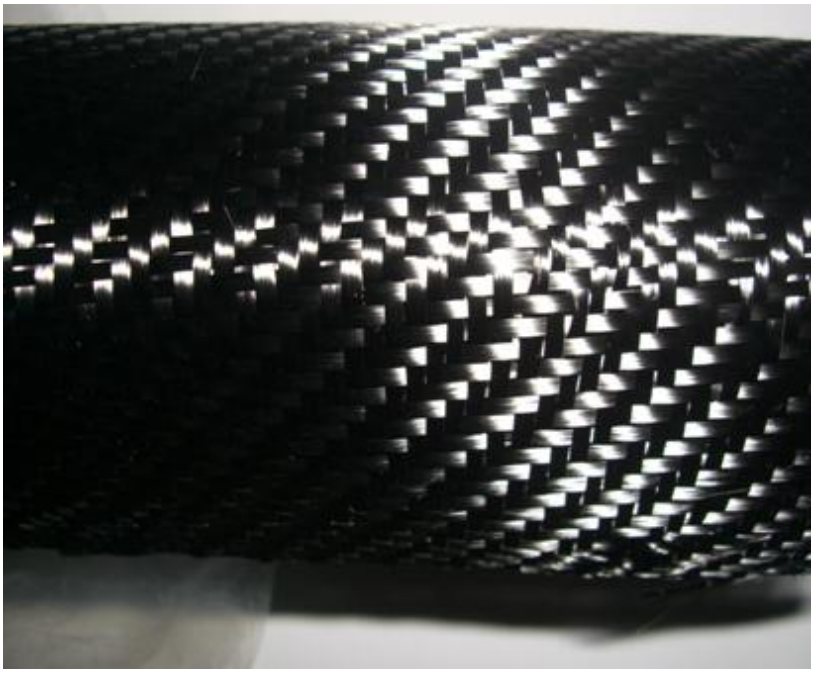

Fig.3.2 Carbon fabric

3.1.3 Glass Fabrics

The Glass fabric has been chosen among an enormous range of areal weights and types which gave no constrains for the adopted solution. The choice fell on the 80 [g m^{-2}] woven fabric because it is the lightest and is commonly used for galvanic corrosion in aerospace composite structures. In theory some trials should have been done using different areal weights and testing at coupon level the behavior during and after an endurance thermal test. For time constrains and scheduled activities this wasn't possible and therefore the criterion has been purely to limit the weight which for the EHCLE prototype would have been not a problem at all but for real applications it will be very critical especially because the fiberglass laminate density is around 2100[kg m^{-3}] whilst the carbon laminate density barely reaches 1500[kg m^{-3}]. Nevertheless a thermal endurance test (TET) was planned and performed for the preliminary analysis of the effects of the thermal stress to the integrity of the laminate in general and to the integrity of the fiberglass plies in particular because in direct contact with the heating element.

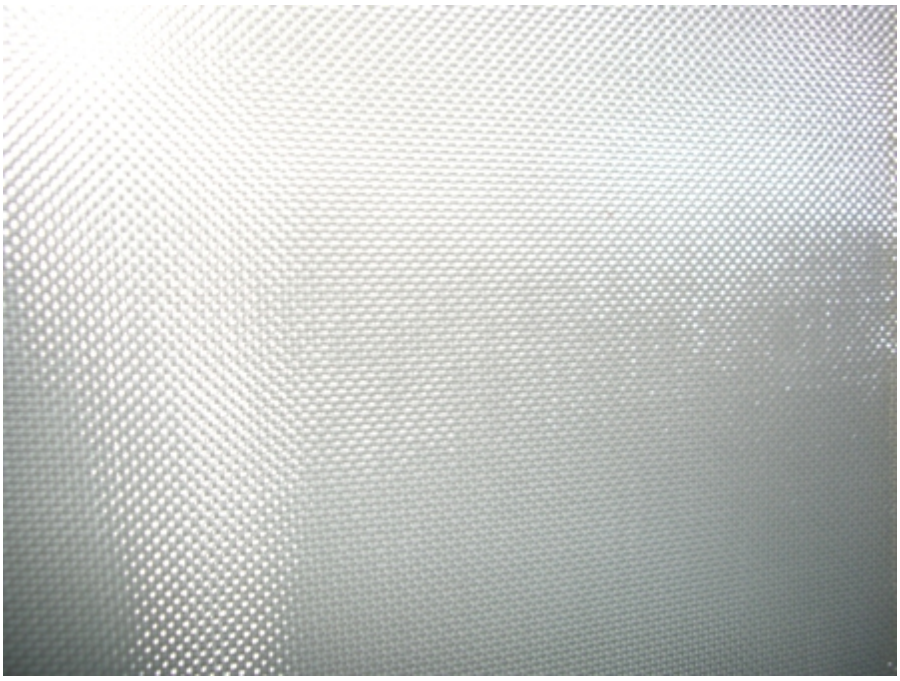

Fig.3.3 Fiberglass 120 style used for EHCLE manufacturing

3.1.4 Electrical Resistance

The Heating Element material was selected according to two basic needs. First of all the material should have a suitable electrical resistivity which would guarantee the max heating for the assigned available electrical power. Second, the material should have a coefficient of thermal expansion very close to that one of the composite laminate to avoid that the materials strain differently inducing dangerous internal static stresses. For these reasons the Ni80-Cr20 alloy was chosen and resistance was manufactured from a strip 3.2[mm] x 0.12[mm] and folded and bent to give the required shape and total length.

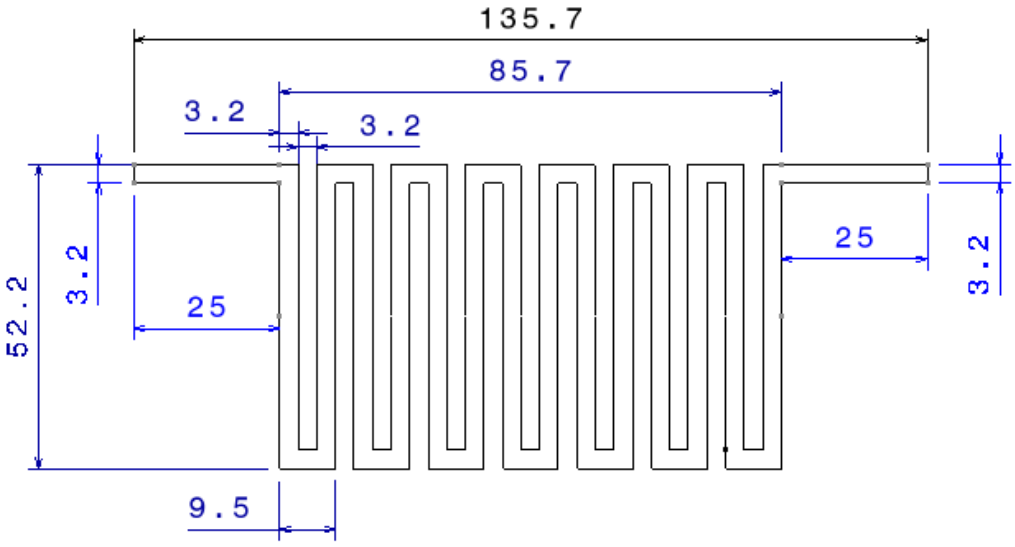

Fig.3.4 EHCLE Prototype Ni-Cr Heating Element as designed

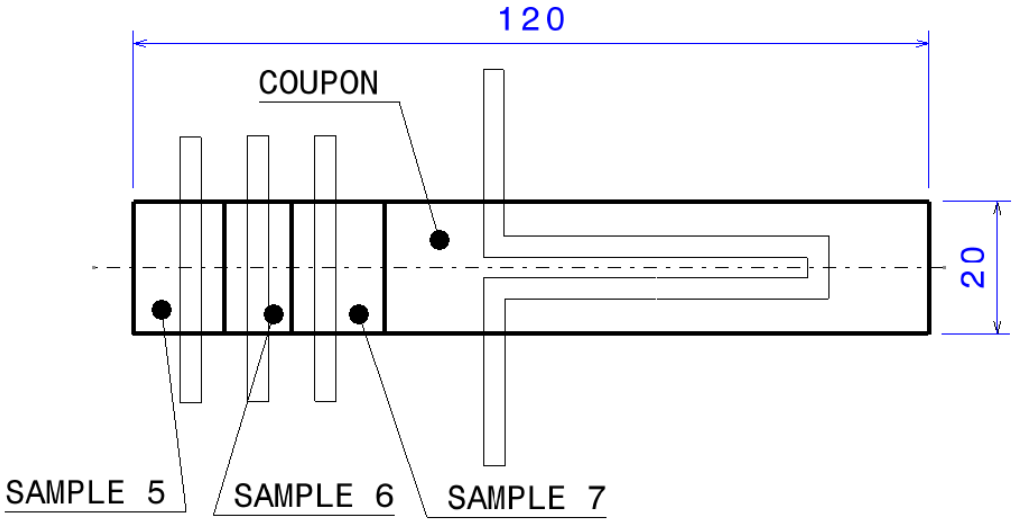

Fig.3.5 EHCLE Coupon Ni-Cr Heating Element as designed with coupon contour

During the layup of the wet laminate into the female tool the heating element was rolled to give a shape similar to the NACA0012 profile to avoid that it would move during the curing cycle as consequence of string back effect. The Ni80-Cr20 strip as received from manufacturer was finished up to surface roughness below 0.8[μm] Ra but, in order to improve the adhesion of the HT resin on it, the heating element was slightly sanded on all surfaces by abrasive paper grade 280 to bring the surface roughness approximately up to 1.6÷3.2[μm] Ra.

3.1.5 Main Body Materials

The main body was NC crafted out of oak wood plate. It was dried, impregnated with epoxy resin coating cured at room temperature for one day and finished by hand to reach the target tolerance which was set as ±0.35[mm] (1% of the airfoil max thickness) to the nominal loft (see dimensional control report in Fig.3.12).

3.2 Ply cutting

Dry fabric was bindered using the same HT resin used for the final manufacturing cycle in a percentage ranging 2÷5% of the total resin needed for the complete impregnation. After drying for one hour at RT conditions, all plies were cut from bindered roll by precision hand scissors using a template with an overall precision of ±0.5[mm]. Operation were not executed in a certified "clean-room" but in a room with controlled atmosphere and sufficient air recycling.

3.3 EHCLE prototype layup and stacking sequence

Once completely dried, the plies were laid up according to the layup defined within the Tab.2.1 with interposition of resin layers according to the calculated amount per ply with an over-resin of 20÷25% to guarantee the best laminate quality for the processing. Complete layup include also auxiliary materials which are not shown in Tab.2.1 because they are not part of the final laminate and are only used to help the processing and removed after it. Ply positioning within the laminate wet layup was affected by an accuracy of ±1[mm] but this has

not compromised the final quality because the manufactured part was not net-to-shape but the edges were trimmed to final contour through machining operations.

3.4 EHCLE prototype Tooling

Tooling was crafted out of ceramic using an existing aluminium airfoil NACA0012 with same dimensions of the EHCLE prototype. Soft ceramic was spread around the aluminium model, previously coated with release agent, reinforced with chordwise and spanwise soft ceramic supports and then cured in oven at 250[°C] for 3 hours. After curing it was removed from oven at same temperature, easily demoulded from the aluminium profile and gradually cooled back in oven (switched-OFF) down to RT condition in about 4 hours. Quality of inner surface of the ceramic tooling was almost perfect with no porosity and no superficial channels. Inner surface was cleaned with solvent to remove residual release agent traces.

3.5 EHCLE prototype Auxiliary materials

Basic auxiliary materials used for moulding purposes have been selected among those qualified for aerospace applications, they are non-contaminant with respect to the laminate and are approved for safety. AUX materials include peel ply, release film, bleeder, breather fabric, vacuum bag, release agent, seal and are shown in Fig.3.6 :

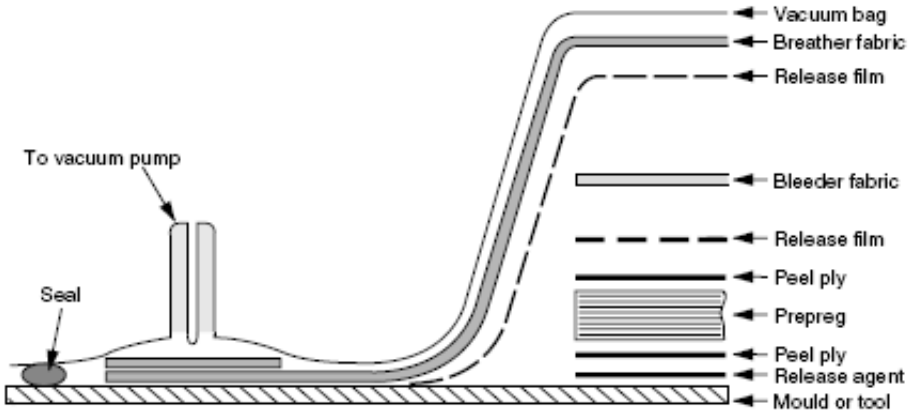

Fig.3.6 Stack up sequence adopted for the moulding of the EHCLE laminate

3.6 EHCLE prototypes and coupon Curing Cycle

Curing of coupons and prototypes has been performed in oven, model AT350, with operating range 0÷350[°C] with accuracy of ±1%. Heat up rate and vacuum rate are shown within curing cycle report in Fig.3.7. Pressure on the laminate was applied through vacuum bagging around the laminate itself with final inside-bag pressure of 20[Torr].

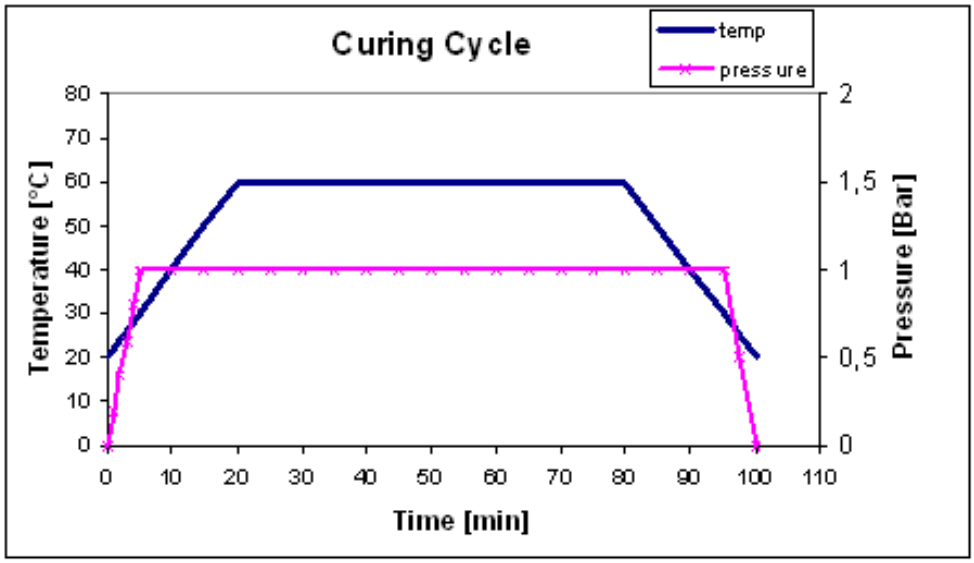

Fig.3.7 EHCLE Prototype curing cycle

Fig.3.8 EHCLE Prototype as demoulded after first curing cycle

3.7 EHCLE prototypes and coupon Post-curing Cycle

Post-curing of EHCLE coupon and prototypes has been done in the same oven as the curing cycle after complete cooling of the cured article which for the leading edges took 4 hours and for the coupon 2 hours only. Post-curing cycle was performed in air atmosphere, with articles completely demoulded and clean from any trace of AUX materials. Heat up rate is shown within post-curing cycle report in Fig.3.9.

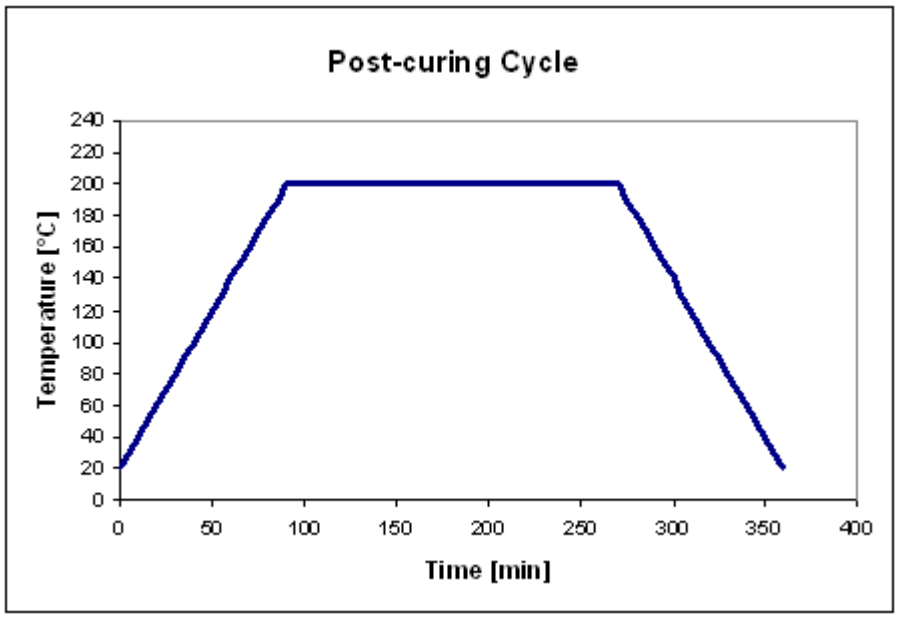

Fig.3.9 EHCLE Prototype post- curing cycle

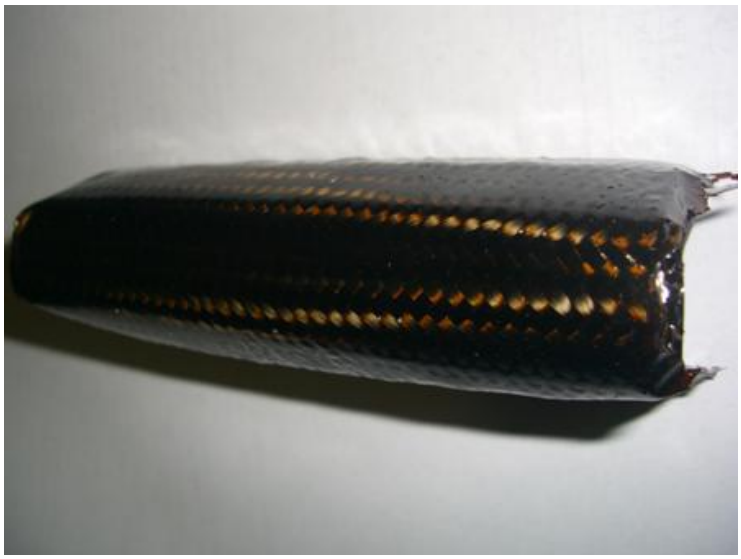

Fig.3.10 EHCLE Prototype after post-curing cycle

3.8 EHCLE prototypes and coupon Fiber Volume Fraction

The Fiber Volume Fraction has been calculated measuring all material and process parameters assuming negligible volatile contents. Each dry material and resin amount have been reported in a datasheet and the wet and dry weight of the laminate has been reported. The difference between the weight of the cured prototypes measured after curing and after post-curing has found negligible. The manufacturing summary is reported in Tab.3.1.

Tab.3.1 Manufacturing Summary Report and Fiber Volume Fraction

EHCLE 1 Prototype			EHCLE 2 Prototype			EHCLE Coupon		
Item	**Q.ty**	**Dim.**	**Item**	**Q.ty**	**Dim.**	**Item**	**Q.ty**	**Dim.**
Carbon plies	12	-	Carbon plies	12	-	Carbon plies	12	-
Glass plies	4	-	Glass plies	4	-	Glass plies	4	-
Ply Area	0,0138	m^2	Ply Area	0,0138	m^3	Ply Area	0,0020	m^3
Carbon Areal weight	200	g/m^2	Carbon Areal weight	200	g/m^2	Carbon Areal weight	200	g/m^2
Glass Areal weight	80	g/m^2	Glass Areal weight	80	g/m^2	Glass Areal weight	80	g/m^2
Resin density	1,2E+06	g/m^3	Resin density	1,2E+06	g/m^3	Resin density	1,2E+06	g/m^3
Carbon density	1,8E+06	g/m^3	Carbon density	1,8E+06	g/m^3	Carbon density	1,8E+06	g/m^3
Dry laminate measured weight	39,0	g	Dry laminate weight	41,3	g	Dry laminate weight	5,4	g
Resin for infusion	29,2	g	Resin for infusion	29,4	g	Resin for infusion	3,9	g
Resin absorbed by Absorbent fabric	6,3	g	Resin absorbed by Absorbent fabric	5,9	g	Resin absorbed by Absorbent fabric	0,9	g
Heating Element measured weight	2,5	g	Heating Element weight	2,5	g	Heating Element weight	0,4	g
Prototype measured weight after postcuring	64,4	g	Prototype measured weight after postcuring	67,3	g	Prototype measured weight after postcuring	8,8	g
Prototype measured weight after postcuring HE nett	61,9	g	Prototype measured weight after postcuring HE nett	64,8	g	Prototype measured weight after postcuring HE nett	8,4	g
Fiber Volume Fraction	0,63	g	Fiber Volume Fraction	0,64	g	Fiber Volume Fraction	0,64	g

3.9 EHCLE prototype demoulding and machining

After first curing cycle the prototypes were demoulded at room temperature. Having both tooling and laminate very limited thermal expansion within the considered temperature range, distortion and spring effects have been negligible as will be later on described within the dimensional control report.

Machining of the composite leading edge to final dimensions has been done by standard diamond disk cutter 2[mm] thick. Machining of the EHCLE1 prototype produced 5 items in total as shown in Fig.3.11:

- EHCLE1 Leading Edge to final dimensions, used for icing tests
- EHCLE1 Sample1, spanwise upper, used for micrographic inspection
- EHCLE1 Sample2, spanwise bottom, used for micrographic inspection
- EHCLE1 Sample3, chordwise INBD, used for micrographic inspection
- EHCLE1 Sample4, chordwise OUTBD, used for micrographic inspection

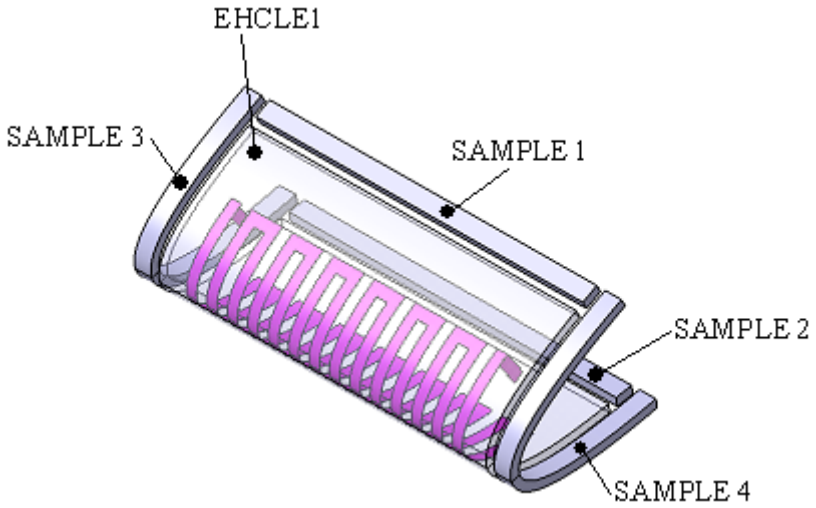

Fig.3.11 EHCLE1 prototype cutting Samples

Samples have been used to check laminate quality through micrographic inspection later on treated. Chordwise cutting obviously did not affect the heating element which was previously bent toward the leading edge cavity thanks to an inner slot created during the layup process. Within this slot the last 10 [mm] of the heating element were coated with release agent so that it was very easy after curing to peel them from the laminate and fold them normal to the laminate ready to be integrated within the electrical contacts.

Machining of the EHCLE Coupon (see Fig.3.5) produced 4 items in total:

- EHCLE Coupon to final dimensions, used for thermal endurance test
- EHCLE Sample5, used for micrographic inspection
- EHCLE Sample6, used for micrographic inspection
- EHCLE Sample7, used for micrographic inspection

3.10 Micrographic Inspection

Micrographic inspection was performed at ASTRA Srl laboratory using microscope model VISION SX45. Inspected samples were cut along chord and span directions to show all possible interfaces between laminate and Ni-Cr resistance. All samples were sequentially sanded with abrasive paper ranging from grade 200 up to grade 1000, cleaned with MEK qualified solvent and dried before inspection. Inspection was performed on the Samples 1÷7 cut from the EHCLE1 prototype and from the coupon to check the overall quality of the EHCLE1 laminate establishing an overall porosity correlation.

A second micrographic inspection was also performed on samples taken from the EHCLE Coupon itself which was cut chordwise and spanwise after the Thermal Endurance Test and the results have been compared to the results previously obtained by the inspection of samples 5÷7. This last micrographic inspection will be shown in paragraph 5.10.

Tab.3.2 Overall porosity correlation obtained from 2D micrographic inspection

Sample	Side	a	b	Section Area	Measured defect area														Total Porosity Area	Total Porosity
		[mm]	[mm]	[mm^2]	[mm^2]														[mm^2]	%
Sample 1	span	118,0	2,65	312,7	0,5	0,8	0,5	0,3	0,5	0,3	0,3	0,3	0,8	0,3	0,5	0,5	0,3	0,5	6,2	2,0%
Sample 2	span	118,0	2,65	312,7	0,5	0,5	0,3	0,5	1,0	0,3	0,3	0,5	0,5	0,3	0,5	1,0	0,5		6,6	2,1%
Sample 3	chord	80,0	2,65	212,0	0,5	0,3	0,3	0,5	0,5	0,8	0,3	0,3	0,3	0,8					4,6	2,2%
Sample 4	chord	80,0	2,65	212,0	0,3	0,3	0,5	0,8	0,3	0,5	0,3	0,3	0,3	0,5	0,3				4,3	2,0%
Sample 5	span	20,0	2,65	53,0	0,5	0,3													0,8	1,4%
	chord	10,0	2,65	26,5	0,5														0,5	1,9%
	chord	10,0	2,65	26,5															0,0	0,0%
Sample 6	span	20,0	2,65	53,0	0,5	0,5													1,0	1,9%
	span	20,0	2,65	53,0	0,5	0,3													0,8	1,4%
	chord	8,0	2,65	21,2															0,0	0,0%
	chord	8,0	2,65	21,2	0,3														0,3	1,2%
Sample 7	span	20,0	2,65	53,0	0,8	0,3													1,0	1,9%
	span	20,0	2,65	53,0	0,3	0,5													0,8	1,4%
	chord	10,0	2,65	26,5	0,5														0,5	1,9%
	chord	10,0	2,65	26,5	0,5	0,3													0,8	2,8%
Total inspected area				1462,8										Total Prosity Area					28,0	1,9%

As shown in Tab.3.2 the overall porosity of the laminate obtained from the 15 examined sections ranged 0÷2.8% with an average total porosity of 1.9%.

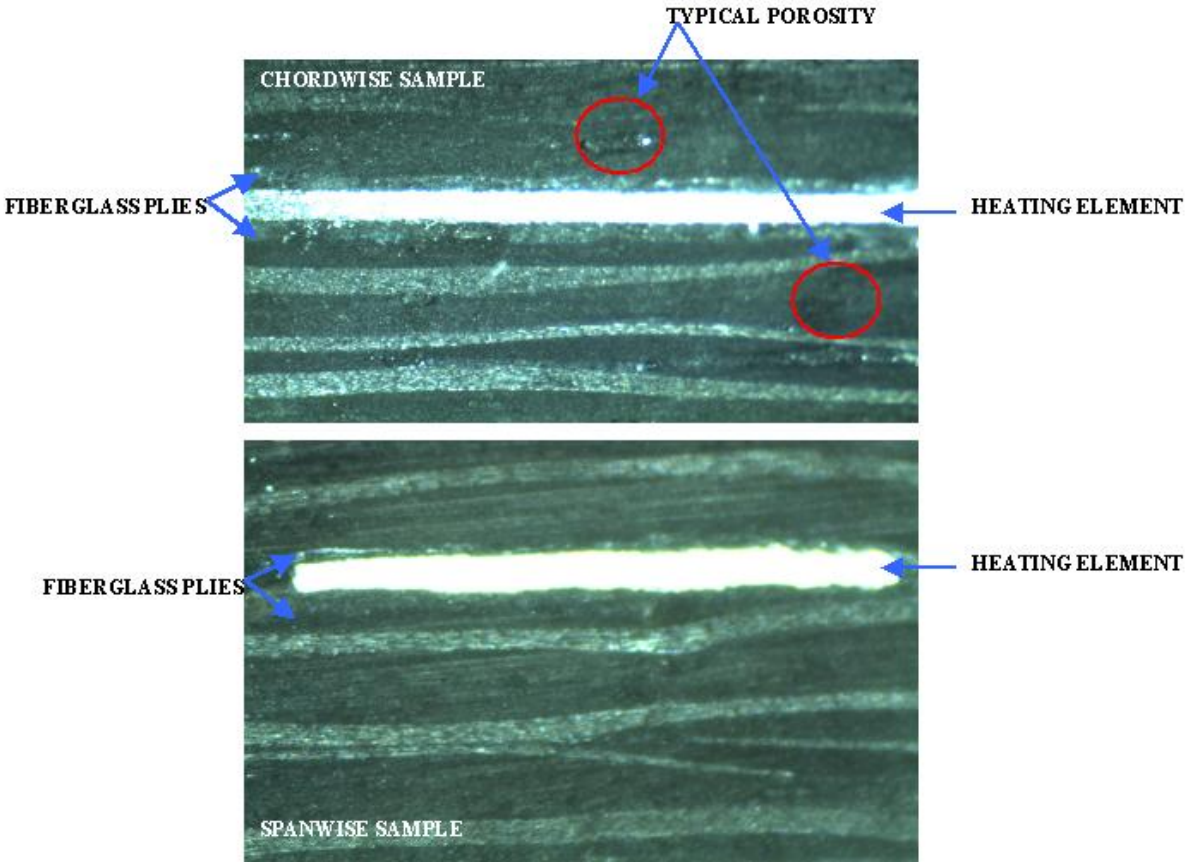

Fig.3.12 EHCLE micrographic inspection sample details

3.11 Painting Systems

Prototype main body, after degreasing and drying, was finished using bi-component Low VOC Polyurethane finish coating, qualified for aerospace applications within the temperature range -55 to 150 [°C], applied by spraying in controlled atmosphere chamber at Room Temperature and cured in the same controlled room for 6[h] at room temperature. According to manufacturer instructions and applied spraying time the final main body coating thickness was ranging 75÷100 [μm].

The finishing of the EHCLE1 prototype was more complex as expected by the nature of the application it was supposed to be exposed. After degreasing and drying, the external surface of the EHCLE prototype was finished with High Temperature Silicon-Alumina finish coating applied by spraying in controlled atmosphere chamber at Room Temperature, dried in the same chamber for 4[h] and cured in controlled atmosphere oven at 150[°C] for 1.5 [h] with heat up and cool down rates of 5[°C min^{-1}]. According to manufacturer instructions and applied spraying time, the EHCLE1 final coating thickness is ranging 30÷40 [μm]. Silicon-

Alumina finish coating could have been applied after treatment of the surface with primer achieving better durability results but for the purpose of the present work it was not necessary and the adhesion of the finishing on the HT resin surface was proven satisfactory.

3.12 Prototypes Dimensional Control Report

Dimensional check was performed at ASTRA Srl laboratory by laser scanning the airfoil half-thickness normally to chord plane.

For the main body the scan was performed by points identified dividing the span in 10 chordwise cross sections and taking 10 equidistant point on each cross section. This mapping resulted in a 100 points grid which has been measured three times assuming as valid measurement the average of the three measurements.

For the composite leading edge the scan was performed by points identified dividing the EHCLE span in 10 chordwise cross sections and taking 12 equidistant point on each cross section. This mapping resulted in a 120 points grid which has been measured three times assuming as valid measurement the average of the three measurements. Measurements where made after finishing and painting for both Main Body and Leading Edge in the assembled configuration

The measurements report summary is plotted in Fig.3.13 with chord distance along ***x*** axis and the airfoil half-thickness on the ***y*** axis, plot shows nominal values against the maximum deviation found spanwise.

The maximum spanwise deviation found for the composite leading edge was ±0.3[mm] to the nominal loft.

The maximum spanwise deviation found for the main body was ±0.5[mm] to the nominal loft.

As it was in certain way expected the deviation from nominal dimensions were in line with typical aeronautical airfoils but due to the reduced dimensions of the prototype deviations reached almost 2% of the total thickness of the airfoil. Nevertheless for the purpose of the present work the dimensional results achieved are more than satisfactory.

It is interesting to point out that the composite leading edge, despite was reaching a better geometrical tolerance than the main body, showed also that the maximum deviations were concentrated at the top and the bottom edges which means that this type of laminate has a tendency to spring-in in those locations. On a large scale prototype this may result in a larger

deviation which may end in an out-of-tolerance contour. This problem will need more deep investigations for future development of EHCLE type Ice Protection Systems.

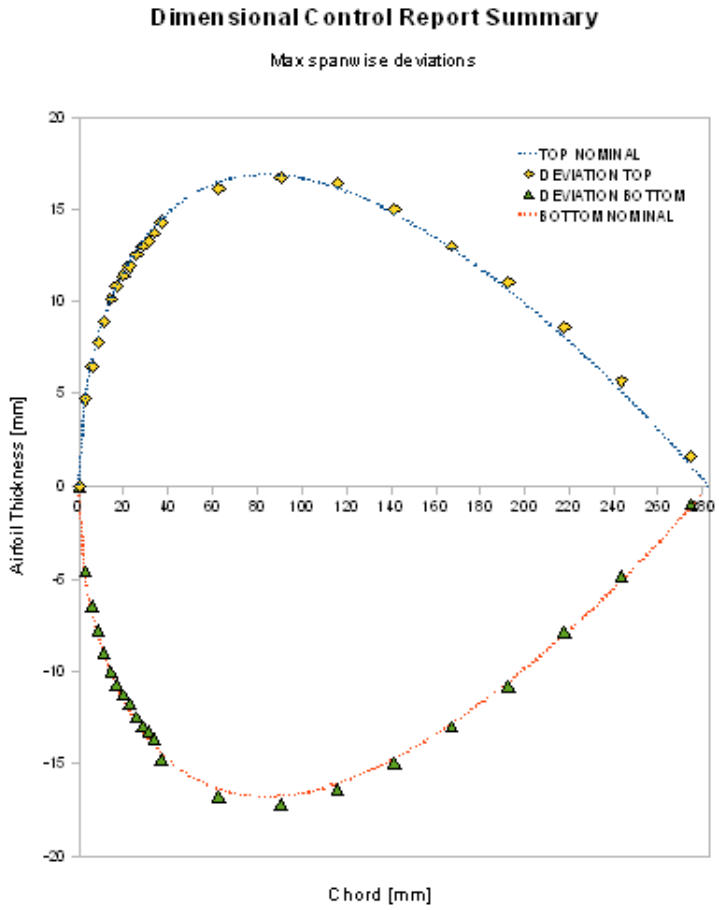

Fig.3.13 EHCLE Prototype maximum contour deviations

4 EHCLE Prototype Instrumentation and Assembly

EHCLE wind tunnel prototype is made basically of two components, the composite leading edge (around 10% of chord length) and the main body (around 90% of chord length). These two component are assembled by means of spanwise screwed joints on the top and bottom. Fixation is made by steel removable screws flush with top and bottom surfaces as shown in the following figure. The composite leading edges, EHCLE 1 and EHCLE 2, were perfectly interchangeable with reference to main body which they were supposed to be installed on. The leading edge was installed on the main body via steel bolts countersunk and hexagonal nuts.

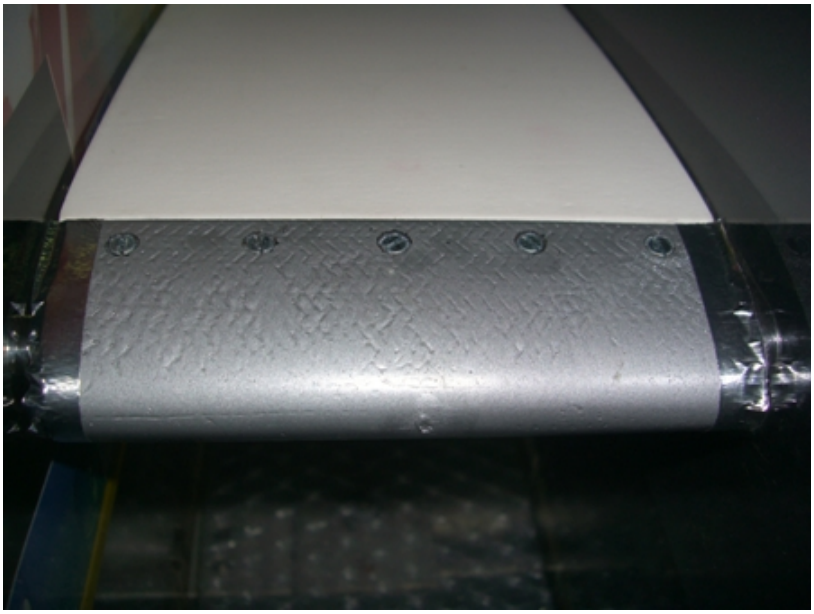

Fig.4.1 Prototype EHCLE1 assembled within IFF test chamber

4.1 Thermocouples

During the test phase the HECLE prototype was equipped with 8 thermocouples type T to monitor the evolution of the temperatures described in following table. Thermocouple wiring was shielded by plastic insulation and glass cloth for both environmental and electromagnetic protection. Thermocouple TC1 aiming to measure the temperature of the heating element T_{HE} in the stagnation point has been cemented to the heating element by drilling the laminate up to it from the inner side.

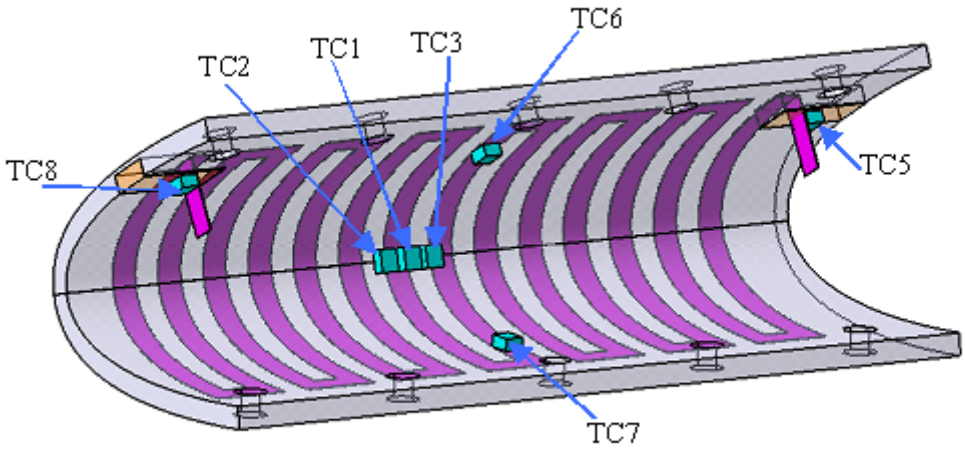

Fig.4.2 Thermocouple position and identification

Tab.4.1 Thermocouple position and identification

TEMP.	TC	DESCRIPTION
T_{HE}	TC1	Temperature of the heating element measured in the middle of the span lenght
T_{ES}	TC2	Temperature of the external surface of the leading edge measured in the middle of the span lenght
T_{IS}	TC3	Temperature of the internal surface of the leading edge measured in the middle of the span lenght
T_{WALL}	TC4	Temperature of the front spar web surface facing the leading edge cavity
T_{HEOUT}	TC5	Temperature of the heating element measured at negative contact within the leading edge cavity
T_{IS_TOP}	TC6	Temperature of the heating element measured in the middle of the span lenght at top extremity of the heating element
T_{IS_BOTTOM}	TC7	Temperature of the heating element measured in the middle of the span lenght at bottom extremity of the heating element
T_{HEIN}	TC8	Temperature of the heating element measured at positive contact within the leading edge cavity

Thermocouple TC2 aiming to measure the temperature of the external surface temperature T_{ES} in the stagnation point has been cemented to the laminate by drilling the laminate up to the external surface from the inner side, installing the TC2 flush with surface, filling gaps with HT resin painted with final coating touch up. TC2 thermocouple is measuring the temperature in the point previously defined as "worst case point" which right in the middle of two chordwise strips of the heating element.

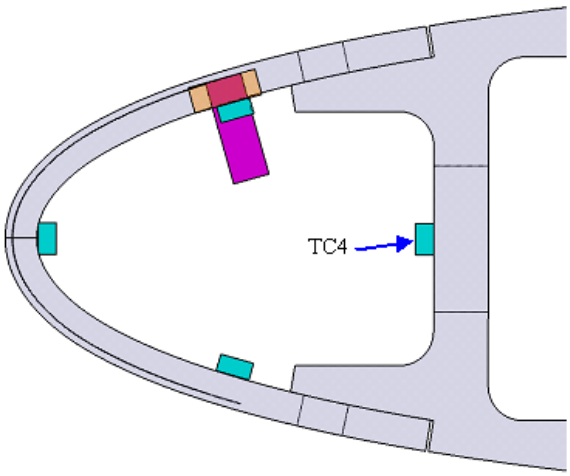

Fig.4.3 Thermocouple position and identification (TC4 located at mid span)

4.2 Acquisition System

An 8 channels acquisition system type NI-USB6210 was used to acquire the 8 thermocouples and it was powered and controlled through USB connector to a laptop. Acquisition sampling was set after first trials to 2.0 [points/s] to limit the amount of date to process and to reduce interferences and noise.

4.3 Power Supply

A 450[W] DC power supply Unit model ATE36-15M has been used for the EHCLE1 prototype thermal tests with max current limited at 15[A] and max voltage limited at 36[V]. Accuracy of measured voltage as declared by the manufacturer is ±0.1[V] whilst the accuracy of the measured current is 0.01[A]. Power supply Unit can be used both manually or interfaced with controller which enabled to preset final values and transient ramp. All thermal test have been performed with a programmed ramp ranging 3÷4 [W s^{-1}].

5 Experimental Methodology and Test Results

The EHCLE test campaign has been primarily focusing on thermal tests under icing conditions to evaluate and identify the system performance under the most severe icing condition offered by the test facility IFF. No aerodynamic test activity has been performed on the airfoil because out of scope for this work and all thermal tests have been done with the airfoil at 0 degrees AOA. The force-balance plate was not installed at all, the strong vibrations of the IFF where absorbed by the test chamber supports (dampers) and the test chamber itself was connected through flexible seals to the rest of the facility.

As part of the system development a thermal endurance test at room temperature has been also performed on EHCLE coupon. Main scope of the endurance test was to preliminary evaluate the interaction composite-resistance after long thermal stress. Coupon has been cut in slices after test for micrographic inspection and comparison with non-stressed coupon.

5.1 Test Facility

The supersonic blow-down wind tunnel has been long used for subsonic icing activity within the Department of Aerospace Engineering. The configurations are interchangeable by replacing the supersonic 2D convergent and test chamber 40[mm]x80[mm] (span, height), by a conical insulated convergent and a subsonic test chamber 120[mm]x300[mm] (span, height). The layout of the wind tunnel in the configuration IFF is shown in Fig.5.1.

The air is compressed by two reciprocating compressors (1 and 2), is then cooled in a heat exchanger where large water drops are formed and separated passing through vanes, filtered in a porcelain filter where all smaller drops are trapped and water vapour is absorbed by a column of granular silica-gel, and in the end is stored in a 4.5 [m^3] steel tank, with a maximum pressure of 30 [bar]. The resulting residual relative humidity of the stored air in the tank is around 5%. The tank is connected through a shut-OFF valve and trough a control valve to a divergent duct followed by a stagnation chamber and a conical convergent nozzle which is exhausting in the test chamber. Downstream of the test chamber the flow is exhausted to atmosphere through a simply divergent diffuser. In order to reduce the heat exchange between the cold stream and the environment the stagnation chamber, the diffuser, the flanges, the valves and the test chamber are coated with a layer of insulating material (polyethylene). An IFF detailed description can be found in [13].

The functional principle of the IFF is based on a very strong initial expansion following a partial opening of the control valve which makes the temperature of the air in the tank to decrease quickly. During high speed expansion Mach number is around 0.5÷0.6 and the temperature drops down at an average rate of 0.5[°C s^{-1}] and the highest is the expansion speed the fastest is the temperature drop. Monitoring the pressure and the temperature in the stagnation chamber it is possible to set a fixed value of the stagnation temperature T_0 programming the PID to close gradually the control-valve to keep it constant as long as possible once it has been reached.

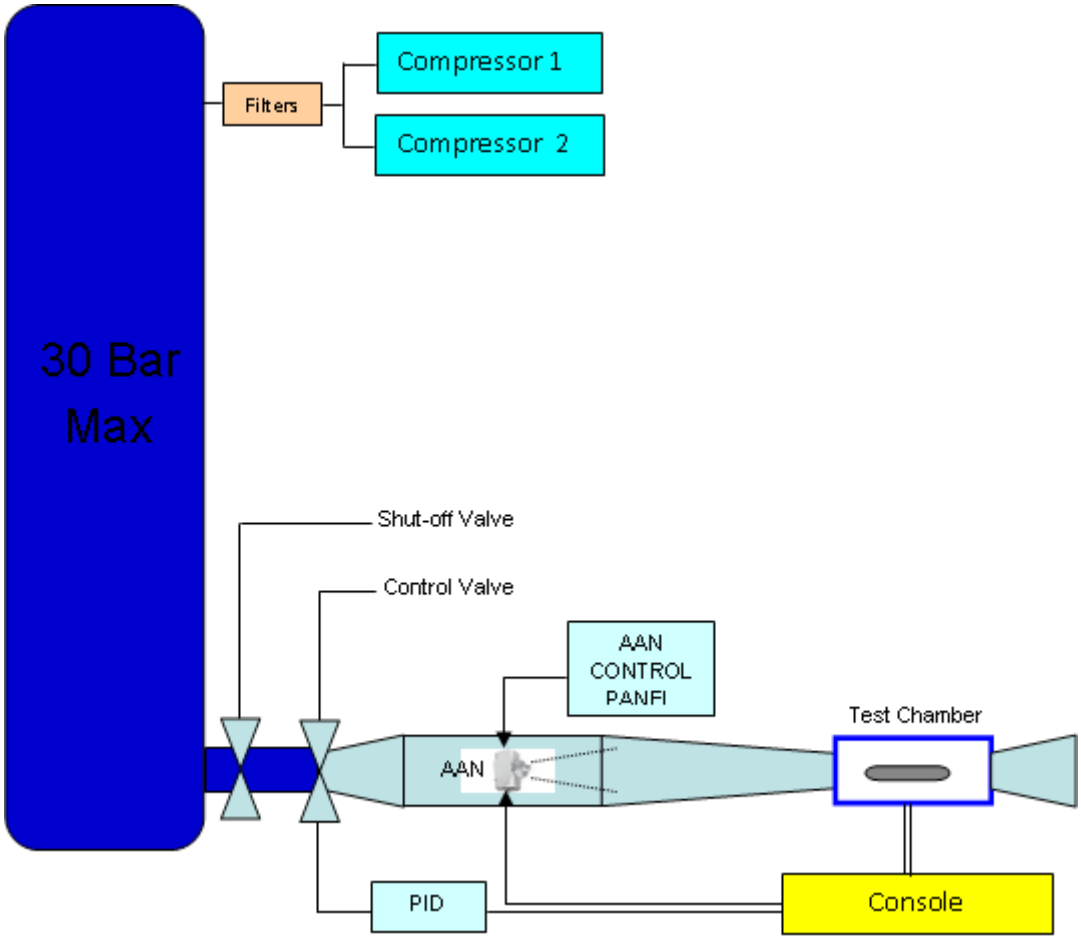

Fig.5.1 Scheme of the IFF (Icing Flow Facility) available at University of Naples, Department of Aerospace Engineering DIAS

Obviously when the tank is almost empty, around 2 [bar], the flow becomes unstable and there is no more control of temperature which starts to increase ending the useful part of the test. During both the high speed expansion and the effective RUN the flow can be either dry or wet with the Water Spraying System (model AAN1/8JJ) set in OFF or ON position respectively.

When a stable value of T_0 is reached, the effective RUN starts and immediate icing conditions are created when the Water Spraying System is ON. The total useful duration of a RUN is in the range of 4÷5[min] pending on the ambient temperature. Due to nature of the IFF facility for each value of T_0 there is a correspondent and unique value of the Mach number driven by the pressure P_0 in the stagnation chamber and the IFF components areal ratios. As previously stated all test campaign for the EHCLE IPS has been performed under ITC5 conditions where the IFF is imposing T_0 =-20 [°C] and Mach number M=0.2.

Obviously the water content makes the temperature in the stagnation chamber to decrease and to limit this variation a calibration of the IFF was performed. The resulting LWC and MVD for the generated clouds at the target temperatures are reported in Tab.5.1.

Tab.5.1 IFF calibrated Icing Test Conditions

Icint Test Condition	Stagnation chamber	AAN1/8JJ		Test Chamber Flow		
	Total Temp T_0	Air Pressure P_{NA}	Water Pressure P_{NW}	MVD	LWC	Mach Number
-	°C	bar	bar	μm	g/m³	-
ITC1	-20	0,60	0,20	35	0,3	0,2
ITC2	-20	0,60	0,30	35	0,4	0,2
ITC3	-20	0,60	0,40	50	0,7	0,2
ITC4	-20	0,70	0,20	30	0,2	0,2
ITC5	**-20**	**0,80**	**0,40**	**35**	**0,6**	**0,2**
ITC6	-10	0,80	0,60	50	1,0	0,2
ITC7	-10	0,90	0,10	25	0,2	0,2
ITC8	-10	0,90	0,40	30	0,5	0,2
ITC9	-10	1,00	0,10	20	0,1	0,2
ITC10	-10	1,00	0,60	35	0,8	0,2
ITC11	-10	1,00	0,80	50	1,1	0,2
ITC12	-10	1,20	0,20	20	0,2	0,2
ITC13	-10	1,20	0,60	30	0,6	0,2
ITC14	-10	1,20	1,00	50	1,2	0,2
ITC15	-10	1,40	0,80	30	0,8	0,2

Two temperature, -10[°C] and -20[°C], have been calibrated for various type of clouds showing that the top performance of the IFF is reached at -20[°C] with LWC=0.6 [g m^{-3}] resulting in a MVD of 35[μm] (see ITC5).

Nevertheless it is important to point out that it is very difficult to quantify the percentage of drops which have diameter far from 35 [μm] because this number represents anyway an average. We should more precisely state that the drop diameter distribution showed a prevailing size in the range of 35 [μm] but other drop diameters where anyway present in the flow, in fact, the ice type which was observed on the EHCLE prototype was mixed and not rime as it should have been in relation to the small drop diameters. This fact gives an indication that a sensible percentage of large droplet is present under condition ITC5.

LWC and MVD measurements were made with a Phase Doppler Particle Analyzer (PDPA). In the PDPA a system of lens, mirrors and optical fibers called "Fiber Drive" (FD) splits the original beam emitted by a 5[W] Argon-ion laser in 3 couples of rays, since 3 components of velocity are to be measured. In each couple the first ray of order zero and the second one of order one are shifted by a frequency of 40[MHz] through a "Bragg Cell". Thanks to the frequency shift between the two beams the interference fringes move in the volume of measure allowing the measure of null or negative components of velocity. All the beams are sent, through the optical fibers to the transmission optics that put them into focus in the volume of measure. In the reception optics the signal scattered by the particles passing in the volume of measure is sent to three photomultipliers. The light signal, transformed in electric analog signal by each photomultiplier, is firstly filtered from the low frequency component due to the Gaussian shape of light intensity in the volume of measure (frequency of pedestal) and therefore mixed (procedure of down mixing) with another signal in order to subtract the component of frequency introduced by the Bragg Cell so that the resultant frequency is the Doppler frequency proportional to the speed of the particles passed in the volume of measure. Each photomultiplier points out therefore the same signal shifted this time in phase because of their relative distance. Thanks to the method of the PDPA, utilizing the linear theory of geometrical optics, from the measure of the phase difference between the signals of each photomultiplier is possible to determine the diameter of each drop. The PDPA can therefore provide both the LWC and the MVD of the drops

5.2 Icing Test Method

The IFF limited operation time in well established and stable conditions was imposing a massive man-work-load due to continuous charging and emptying of the air reservoir up to 30[bar] in change of around 4 minutes of icing test useful time. For the EHCLE test campaign the IFF was always set at icing condition as defined by ITC5 in Tab.5.1. Majority of test were performed in winter to maximize the duration of the runs and the temperature T_0 was always set at -20[°C] whilst the model was kept at a temperature of around -15/-18 [°C] before run starting. During the high speed expansion the EHCLE prototype was undergoing first to a moderate heating and was then cooled as soon as the temperature dropped down to approximately T_0 = -20[°C]. The cooling phase of the model was lasting till the temperature T'_{ES} measured on the model surface was stable at -20[°C] and after that point the Water Spraying System was turned ON and the thermal test was started. The cooling phase of the model was lasting around 30÷60[s] depending on the initial temperature of the model itself. In theory, after the cooling phase, all temperatures measured on the model should have been at -20[°C] but some higher temperature was recorded. Due to the limited duration of the IFF RUN, in fact, it would have taken too long to get the inner cavity cooled down to -20[°C] and it would have taken away some time essential to the thermal test. Before a thermal test was started, temperature within the inner cavity of the leading edge where in the worst cases in the range of -12/-15 [°C]. It will be anyway shown that this difference is producing a negligible effect on the total power needed to reach operative functionality of the EHCLE system mostly because once it is ON there is a negligible gradient of temperature towards the inner cavity. This means that whatever the temperature within the inner cavity is, as soon as the system is ON, the inner surface will immediately reach a temperature very close to the heating element one because on the inner surface of the EHCLE system there is almost no thermal resistance (natural convection).

Secondarily it should be pointed out that in real aircraft the temperature within the inner cavity is not mandatorily the same as the temperature on the external surface (when anti-icing is OFF) but it is few degrees higher due to the thermal shield offered by the skin and some heating provided by some equipment and systems.

As I've previously said, once the temperature T'_{ES} measured on the model was stable at -20 [°C] the thermal test was started activating the power supply unit which was previously programmed to reach the target power by a linear ramp at a rate of 3÷4 [W s^{-1}]. For some test the ramp has been operated manually with approximately the same rate without any significant difference. After the target power density Q_J was reached the surface temperature

reached an equilibrium temperature with a certain delay which can be measured from the RUN plots. Once at equilibrium the RUN can be considered finished but the equilibrium condition is kept until the end of the ITC5 stable conditions for measurements and image-video captures. Temperature have been recorder during the complete duration of the RUNS, but only the significant part of them will be presented.

It should be noticed that, as shown in Fig.5.2, the difference between a run performed during the summer and one performed during the spring or the winter yields only slightly shorter test duration with no effective change in performance. Curve above shown have been filtered to remove noise and interference due to the high amount of equipment around the IFF wind tunnel. Test temperature have to considered with an uncertainty of ±2[°C] due mostly to the reaction time of the electro-pneumatic-valve which needs to feel at least 0.5[°C] variation before moving to compensate it.

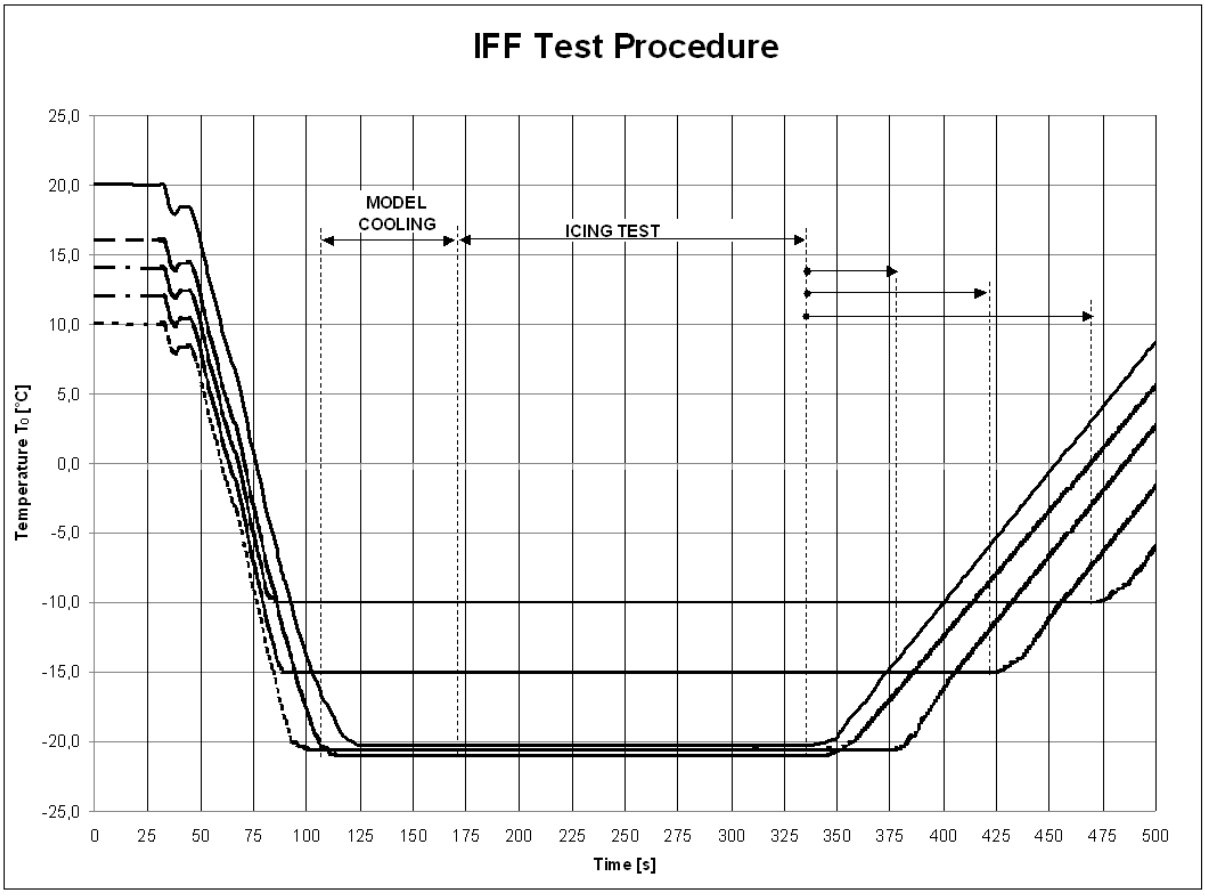

Fig.5.2 Typical IFF icing test procedure for different ambient temperatures

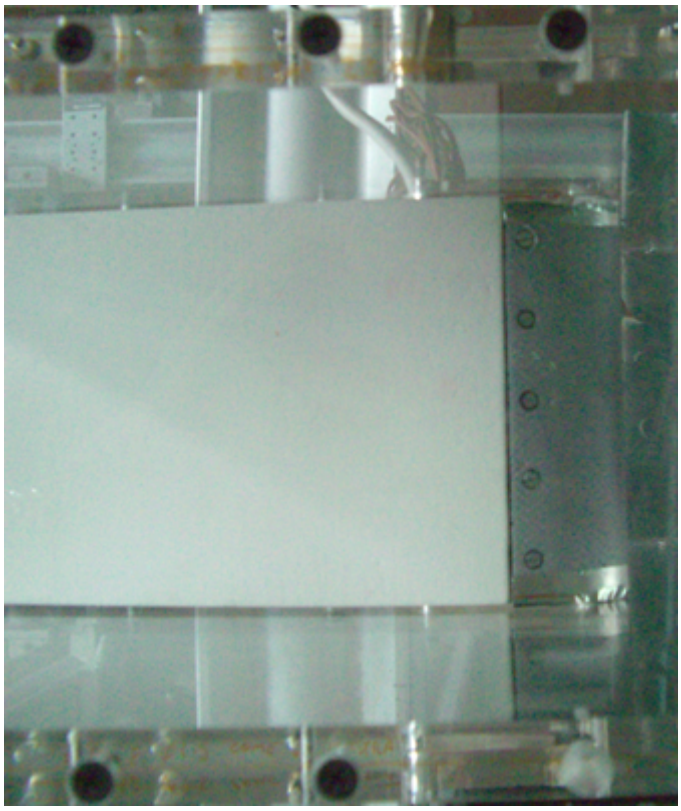

Fig.5.3 EHCLE prototype assembled within the IFF test chamber

5.3 Uncertainty analysis

The temperature measurements has been essential to the present work and in this paragraph a preliminary uncertainty analysis is proposed assuming a linear combination of all single contributions. In theory a rigorous analysis would account also for the interaction between various components which may result not linear combination of effects but for the purpose of the present work a simplified approach is acceptable [62]. The effects which have been accounted for the uncertainty analysis are related mainly to the "position accuracy" of the thermocouples estimated in about ±2[°C] mostly due the difficult through thickness positioning, the data acquisition system overall accuracy estimated in about ±0.5[°C], the thermocouple accuracy itself as declared by the manufacturer ±1[°C] and the electromagnetic interference intensity estimated in about ±0.5[°C].

As a result of this uncertainty analysis, the temperature measurements are affected by an overall accuracy of ±4[°C] for the power densities ranging 10÷30 [kW m^{-2}] and slightly smaller for lower power densities.

5.4 Icing Test Matrix

Icing test Matrix was planned with the aim of scanning a wide range of energies Q_J provided to the heating element and monitor the consequent thermal behavior of the EHCLE laminate focusing on the measured external surface temperature T'_{ES}. During the test campaign some new test was introduced to better scan energy ranges which showed to be interesting. A total of 78 icing RUNS have been performed on the EHCLE1 prototype including setup tests, aborted tests and tests with anomalies which have been repeated. In Tab.5.2 only 35 significant RUNs are reported, named by IFF sequential number and identified by the supplied power Q_J, the measured external surface temperature T'_{ES} and a comment about the general outcome of the test.

Tab.5.2 EHCLE Icing Test Matrix

IFF RUN Number	Icing Test Condition	EHCLE Functional Mode	EHCLE Measured Power density Q_J	EHCLE Measured Surface Temp. T'_{ES}	Description
	ITC		[kW/m²]	[°C]	
EHCLE1-IFF-RUN-1	ITC5 (LWC=0)	FM13	5,1	11,0	DRY – HTC calculation
EHCLE1-IFF-RUN-2	ITC5 (LWC=0)	FM14	9,6	39,9	DRY – HTC calculation
EHCLE1-IFF-RUN-3	ITC5 (LWC=0)	FM15	15,6	70,0	DRY – HTC calculation
EHCLE1-IFF-RUN-4	ITC5 (LWC=0)	FM13	5,2	12,0	DRY – HTC calculation – Repeatibility
EHCLE1-IFF-RUN-5	ITC5 (LWC=0)	FM14	9,5	40,3	DRY – HTC calculation – Repeatibility
EHCLE1-IFF-RUN-6	ITC5 (LWC=0)	FM15	15,5	69,0	DRY – HTC calculation – Repeatibility
EHCLE1-IFF-RUN-7	ITC5 (LWC=0)	FM13	5,0	10,0	DRY – HTC calculation – Repeatibility
EHCLE1-IFF-RUN-8	ITC5 (LWC=0)	FM14	9,5	41,2	DRY – HTC calculation – Repeatibility
EHCLE1-IFF-RUN-9	ITC5 (LWC=0)	FM15	15,8	72,0	DRY – HTC calculation – Repeatibility
EHCLE1-IFF-RUN-10	ITC5	Tentative	1,1	-14,3	Insufficient for Running Wet
EHCLE1-IFF-RUN-11	ITC5	Tentative	2,0	-10,5	Insufficient for Running Wet
EHCLE1-IFF-RUN-12	ITC5	Tentative	3,3	-4,6	Insufficient for Running Wet
EHCLE1-IFF-RUN-13	ITC5	Tentative	4,1	1,2	Insufficient for Running Wet
EHCLE1-IFF-RUN-14	ITC5	Tentative	5,3	6,9	Insufficient for Running Wet
EHCLE1-IFF-RUN-15	ITC5	Tentative	5,7	8,1	Insufficient for Running Wet
EHCLE1-IFF-RUN-16	ITC5	Tentative	6,1	8,9	Insufficient for Running Wet
EHCLE1-IFF-RUN-17	ITC5	Tentative	6,1	9,3	Insufficient for Running Wet / Repeatibility
EHCLE1-IFF-RUN-18	ITC5	FM12	6,5	9,9	Running Wet
EHCLE1-IFF-RUN-19	ITC5	FM12	6,5	10,5	Running Wet / Repeatibility
EHCLE1-IFF-RUN-20	ITC5	FM12	6,5	10,4	Running Wet / Repeatibility
EHCLE1-IFF-RUN-21	ITC5	FM11	8,6	12,2	Running Wet / Insuffcient for Full Evaporation
EHCLE1-IFF-RUN-22	ITC5	FM10	11,5	16,5	Running Wet / Insuffcient for Full Evaporation
EHCLE1-IFF-RUN-23	ITC5	FM9	12,9	20,1	Running Wet / Insuffcient for Full Evaporation
EHCLE1-IFF-RUN-24	ITC5	FM8	14,4	23,9	Running Wet / Insuffcient for Full Evaporation
EHCLE1-IFF-RUN-25	ITC5	FM7	16,0	28,9	Running Wet / Insuffcient for Full Evaporation
EHCLE1-IFF-RUN-26	ITC5	FM6	17,6	33,6	Running Wet / Insuffcient for Full Evaporation
EHCLE1-IFF-RUN-27	ITC5	FM5	19,3	39,2	Running Wet / Insuffcient for Full Evaporation
EHCLE1-IFF-RUN-28	ITC5	FM4	21,1	45,5	Running Wet / Insuffcient for Full Evaporation
EHCLE1-IFF-RUN-29	ITC5	FM3	23,0	52,6	Running Wet / Insuffcient for Full Evaporation
EHCLE1-IFF-RUN-30	ITC5	FM2	25,0	60,0	Running Wet / Insuffcient for Full Evaporation
EHCLE1-IFF-RUN-31	ITC5	FM16	26,2	66,2	Running Wet / Insuffcient for Full Evaporation
EHCLE1-IFF-RUN-32	ITC5	FM1	27,0	69,5	Fully Evaporative
EHCLE1-IFF-RUN-33	ITC5	FM1	27,1	70,5	Fully Evaporative / Repeatibility
EHCLE1-IFF-RUN-34	ITC5	FM1	27,0	72,1	Fully Evaporative / Repeatibility
EHCLE1-IFF-RUN-35	ITC5	FM17	30,0	77,0	Fully Evaporative / Overheating

Significant test have been repeated 3 times to evaluate the repeatability of the results. It is important to point out that due to limitation imposed by the IFF in terms of RUN duration it was impossible to run icing tests with variable values of the power density $\boldsymbol{Q_J}$. Despite, in fact, the reaction of the EHCLE system to the input current is almost immediate 2÷4 [s] the power needs to be supplied with a ramp to avoid dangerous peaks which could damage structure and instrumentation. As previously described the ramp has been set to climb at an average of 3÷4 [W s^{-1}] and therefore it was possible to test two values of $\boldsymbol{Q_J}$ in the same test but with a very tight procedural schedule which could lead easily to partial results or human errors. For these reasons it was decided to test a single value of $\boldsymbol{Q_J}$ per RUN, having large time for operations and giving enough times to the EHCLE system to reach the relevant equilibrium.

5.5 Preliminary DRY-Tests

Dry test were performed at beginning of the test campaign mostly to check the functionality of components and instrumentation. When setup was finished and all procedures were frozen, relevant DRY RUNS have been performed to measure the effective convection coefficient $\boldsymbol{h_{CDRY}}$ on the external surface for various values of $\boldsymbol{T_{ES}}$ under conditions ITC5-DRY at -20[°C] and LWC=0. Within these tests, the surface temperature $\boldsymbol{T_{ES}}$ for the Running Wet and Fully Evaporative cases, know from preliminary sizing, was reproduced under ITC5-DRY conditions by using a reduced power $\boldsymbol{Q_J}$ as shown within the test matrix table 5.2. These tests showed values of $\boldsymbol{h_{CDRY}}$ in reasonable agreement with the analytical ones as shown in Fig.5.13.

Hereinafter 9 RUNs relevant to DRY tests under ITC5-DRY conditions are reported both for completeness and to keep the traceability of the monitored temperatures. Three power densities $\boldsymbol{Q_J}$ have been explored each of which is repeated 3 times to validate the repeatability.

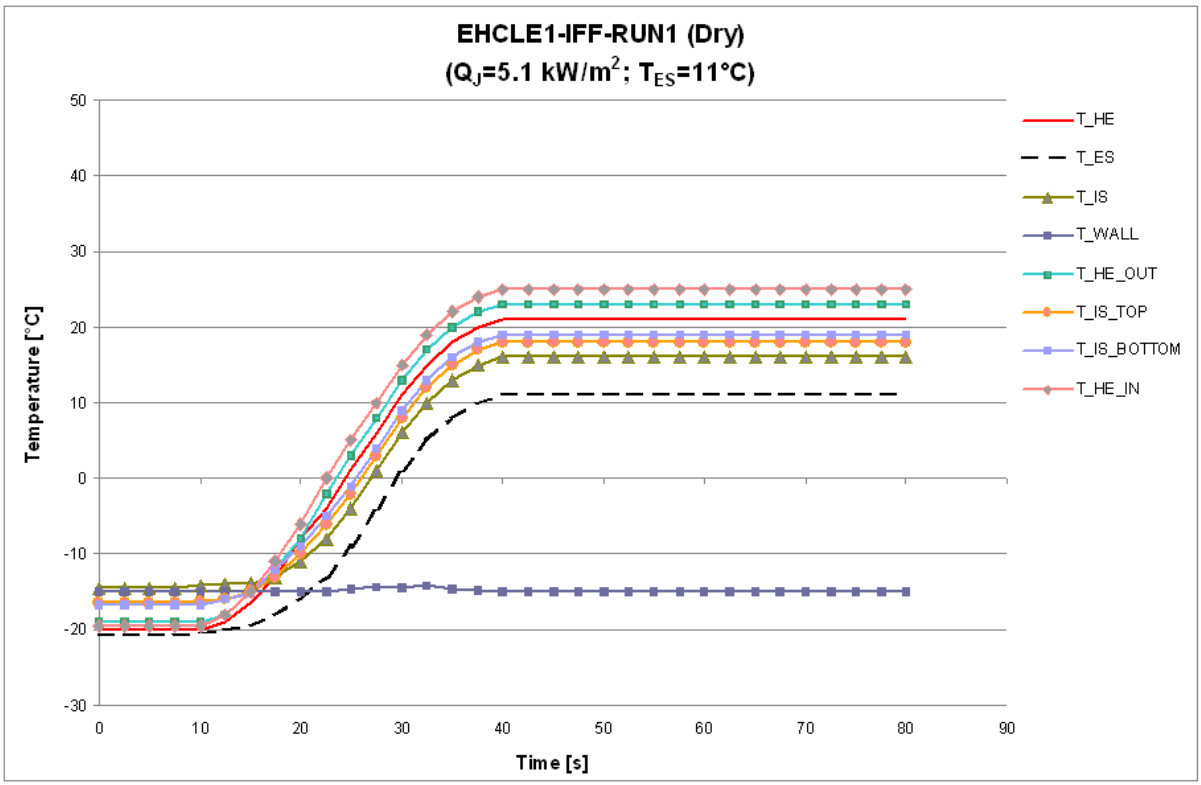

Fig.5.4 Temperature plot relevant to the run EHCLE1-IFF-RUN-1 measurements

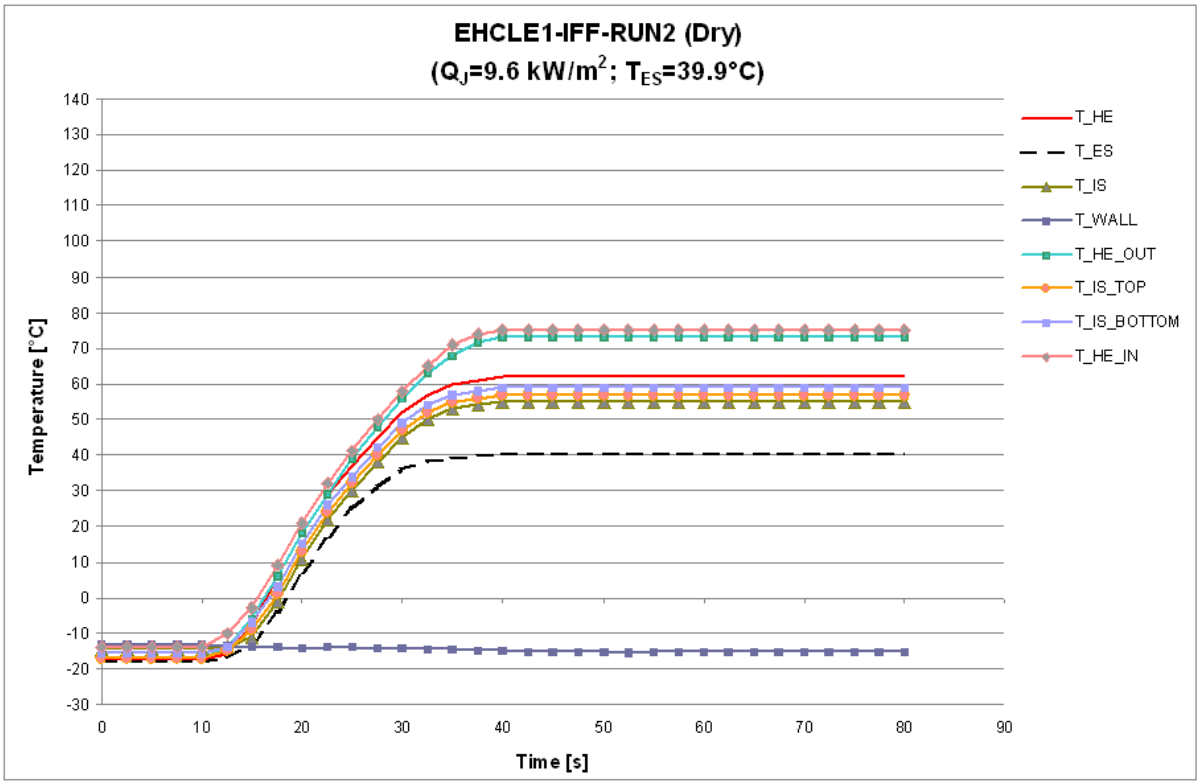

Fig.5.5 Temperature plot relevant to the run EHCLE1-IFF-RUN-2 measurements

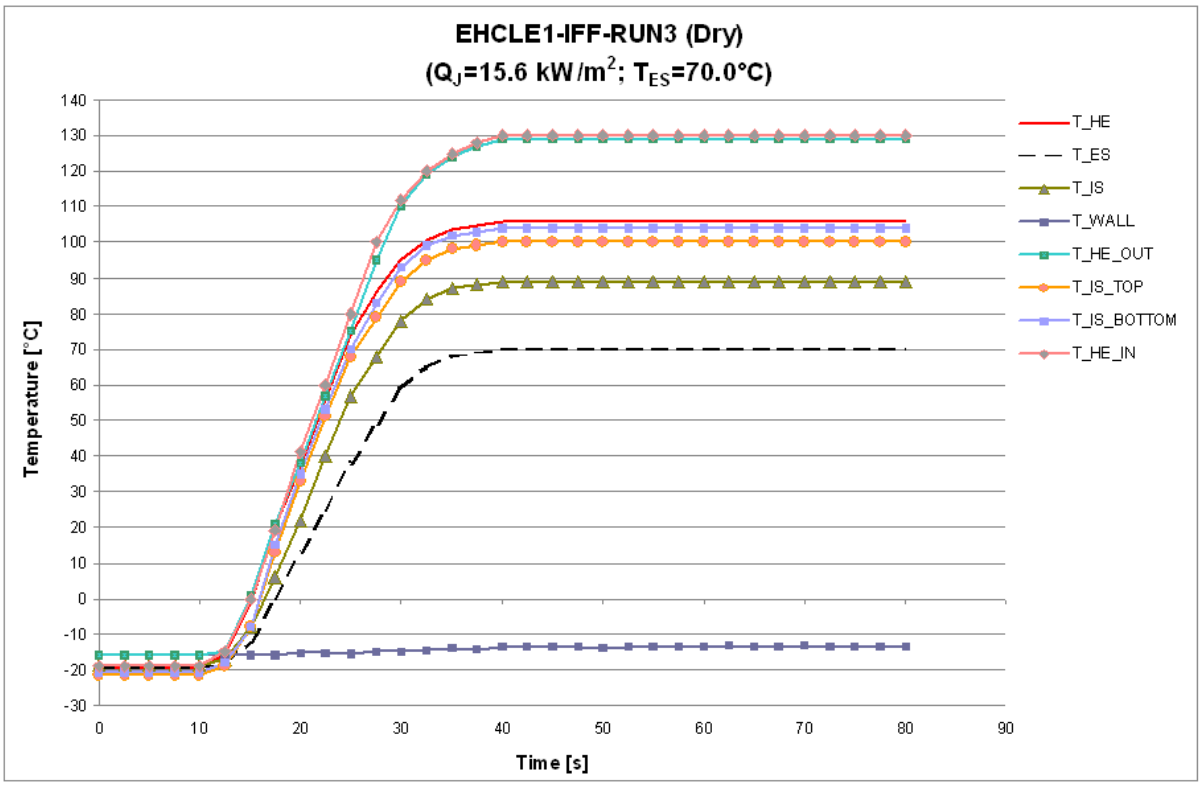

Fig.5.6 Temperature plot relevant to the run EHCLE1-IFF-RUN-3 measurements

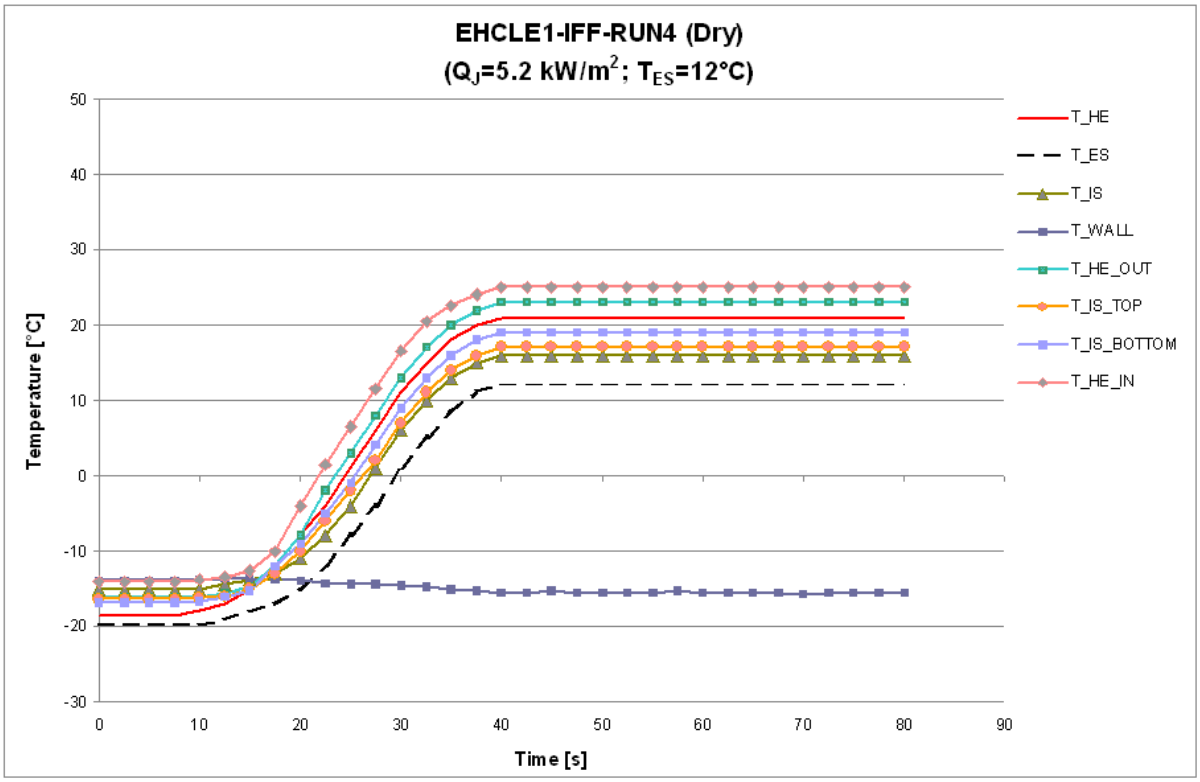

Fig.5.7 Temperature plot relevant to the run EHCLE1-IFF-RUN-4 measurements

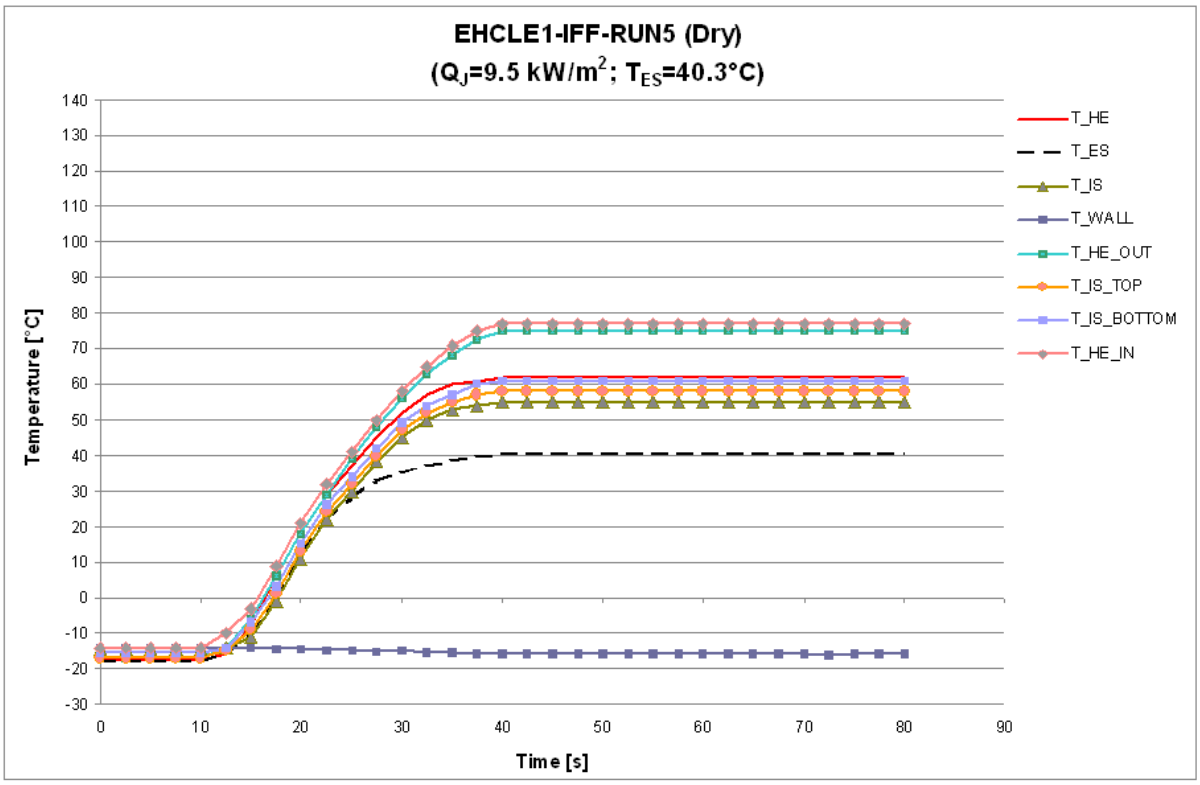

Fig.5.8 Temperature plot relevant to the run EHCLE1-IFF-RUN-5 measurements

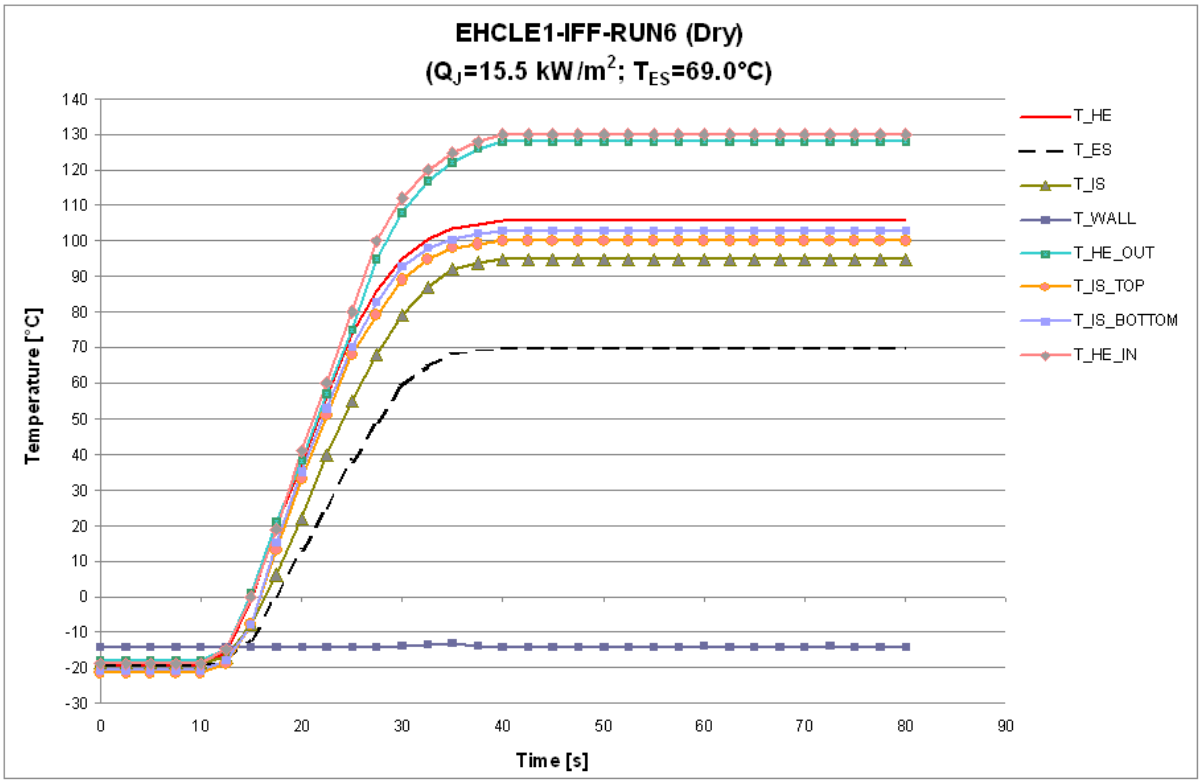

Fig.5.9 Temperature plot relevant to the run EHCLE1-IFF-RUN-6 measurements

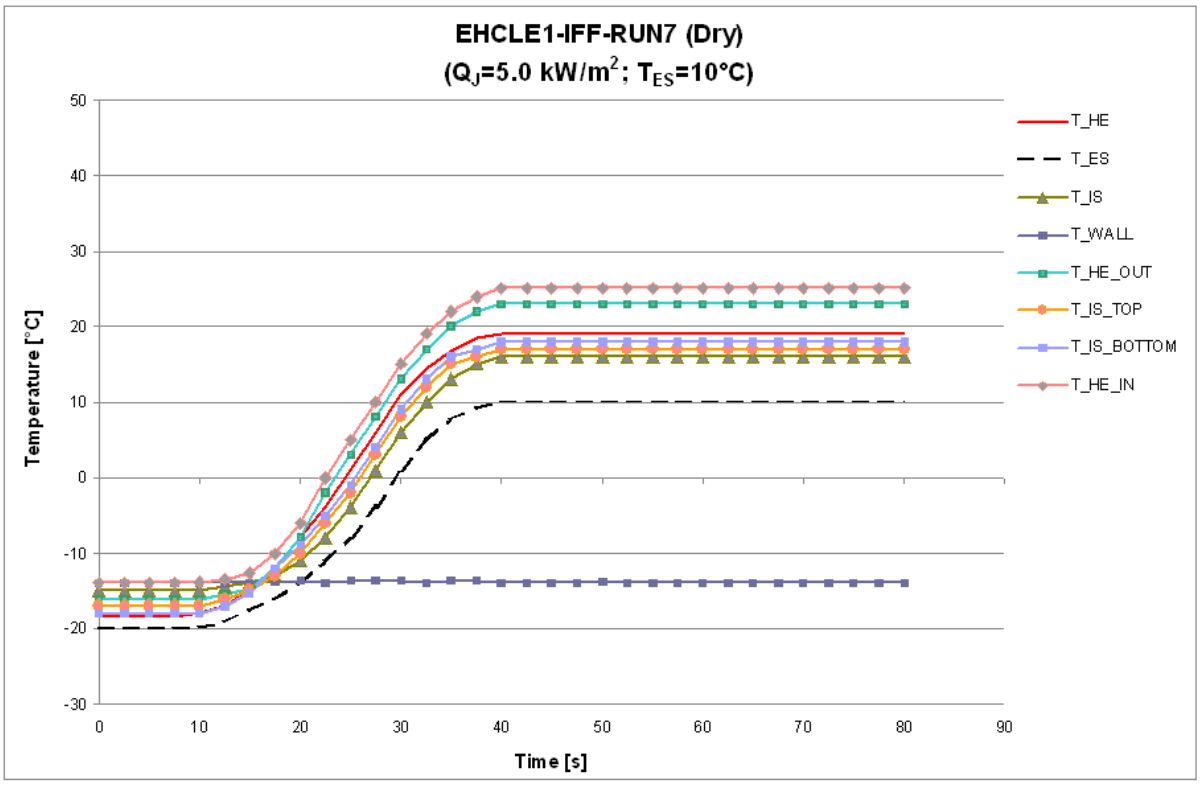

Fig.5.10 Temperature plot relevant to the run EHCLE1-IFF-RUN-7 measurements

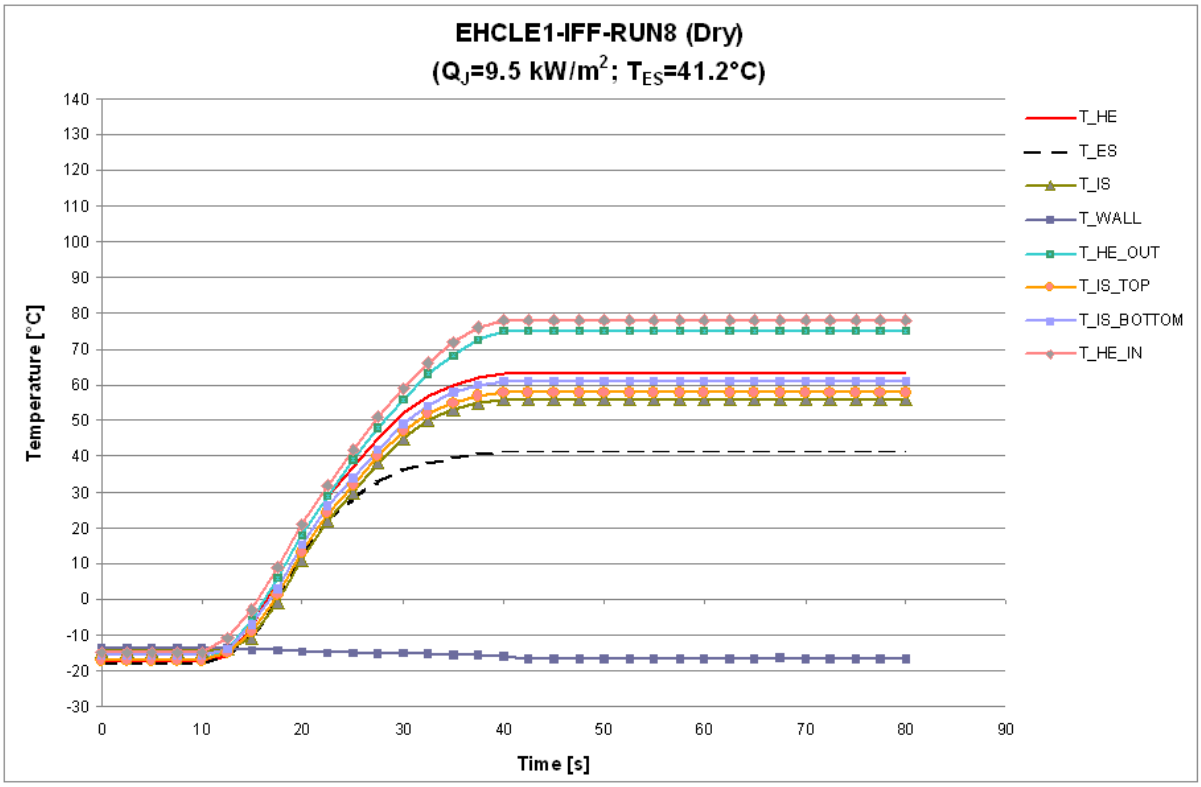

Fig.5.11 Temperature plot relevant to the run EHCLE1-IFF-RUN-8 measurements

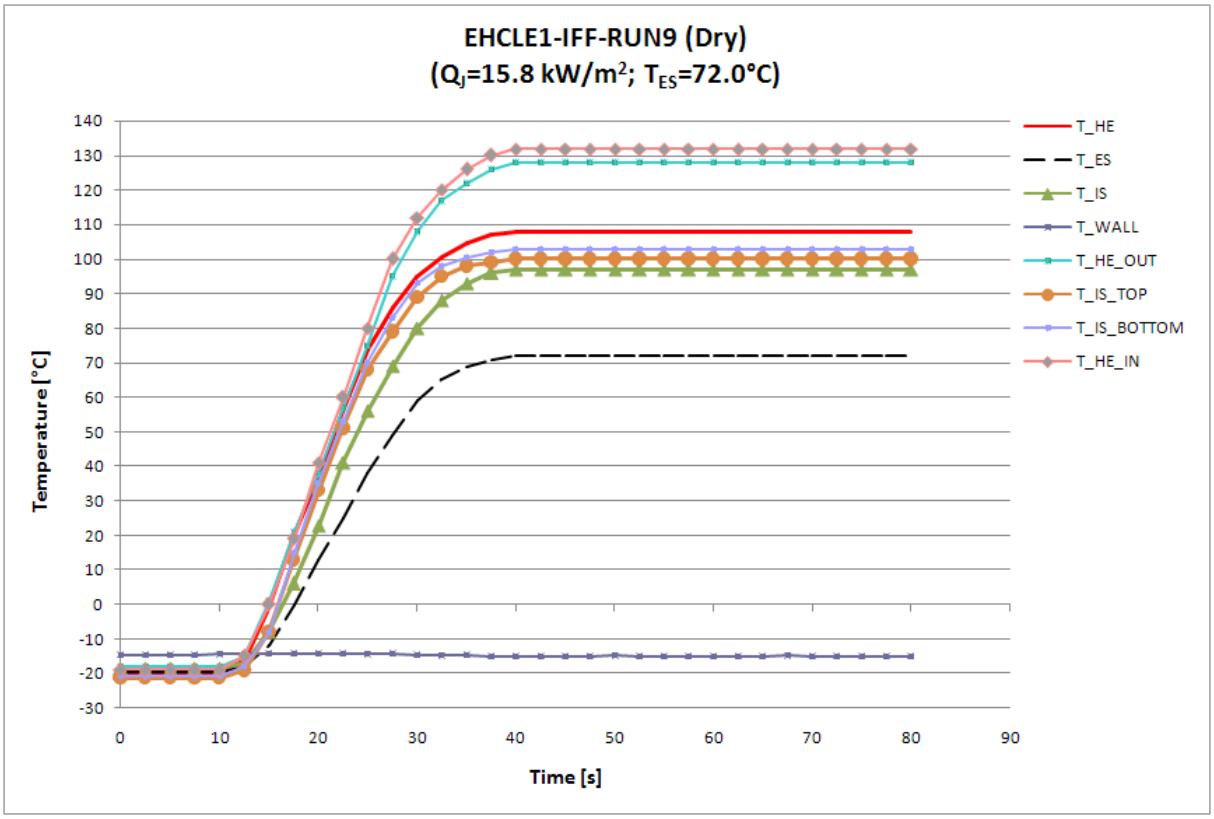

Fig.5.12 Temperature plot relevant to the run EHCLE1-IFF-RUN-9 measurements

DRY convection coefficient measurements. Despite there is an acceptable agreement between analytical and experimental results it is evident from Fig.5.13 that the coefficient h_{CDRY} measured in the stagnation point is constantly higher than the one measured at top and bottom extremities of the protected area. This is due to the fact that the temperature measured at top and bottom extremities is constantly higher than the one measured in the stagnation point. Being the coefficient calculated as:

$$h_{CDRY} = \frac{Q_1}{T'_{ES} - T'_{EXT}} \tag{5.1}$$

where T'_{ES} is the measured value of the external surface temperature, Q_1 as defined analytically by eq. (2.19) (written in this case for h_{CDRY} and not for h_{EXT}) and T'_{EXT} = -20[°C] as measured per ITC5-DRY, it is obvious that being the ΔT measured at top and bottom extremities higher than the one measured in the stagnation point the eq. (5.1) yields higher value of h_{CDRY} for those locations.

It is important to point out that the temperature measured at stagnation point is effectively measured by a thermocouple mounted flush to the external surface whilst the temperature measured at top and bottom extremities is not a direct measure of the external surface temperature but it is measured at same location on the inner surface and then converted in external surface temperature using the gradient calculated through the analytical model described within previous chapters. The physical consistency of this result can be simply explained by the fact that in the vicinity of the stagnation point the body can be geometrically approximated to a cylinder and therefore the heat exchanged is higher than the top and bottom extremities where the body can be geometrically approximated to a flat plate at small incidence.

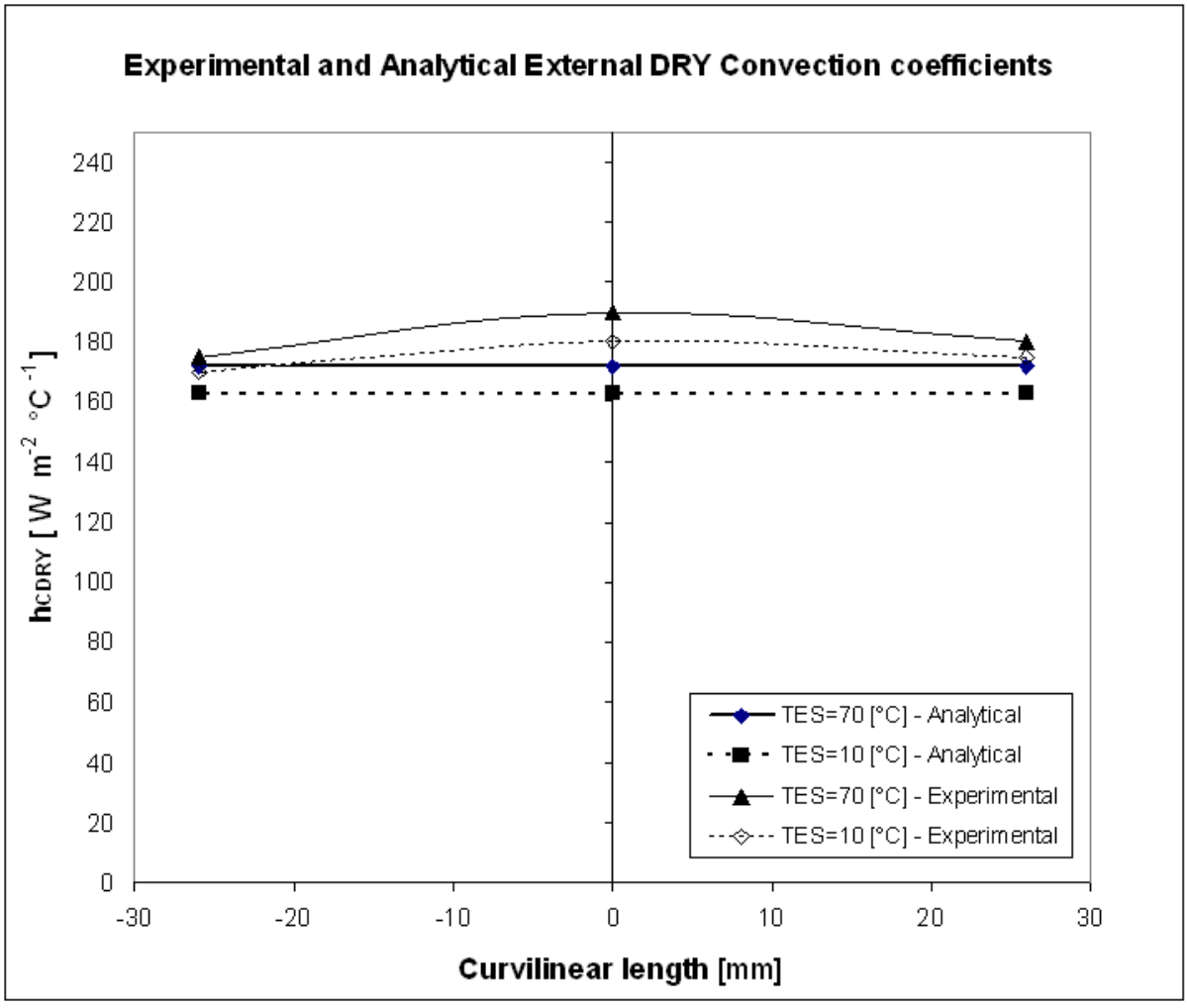

Fig.5.13 Experimental and analytical external DRY convection coefficients (negative curvilinear length refers to the intrados and positive to the extrados)

Nevertheless being the difference between analytical and experimental results smaller than 10% this result is anyway in acceptable agreement. It is important to point out that within the analytical model the convective coefficient is calculated as an average over the whole heated area A_D considered as a cylinder and therefore it is constant all along the heated area as shown in Fig.5.13.

5.6 Preliminary Icing tests

Preliminary Icing tests have been performed to evaluate ice shapes and ice accretion mechanism. Under ITC5 conditions temperature measured on the EHCLE prototype were almost stable at -20 [°C] with exception of the T_{WALL} , measured on the front spar web, which has been ranging between -20 and -11[°C] due to the thermal inertia of the material which would have required very long exposure to cool down to -20 [°C]. This circumstance, as shown by analytical calculations, had anyway a negligible effect on the overall behaviour of the Icing Protection System.

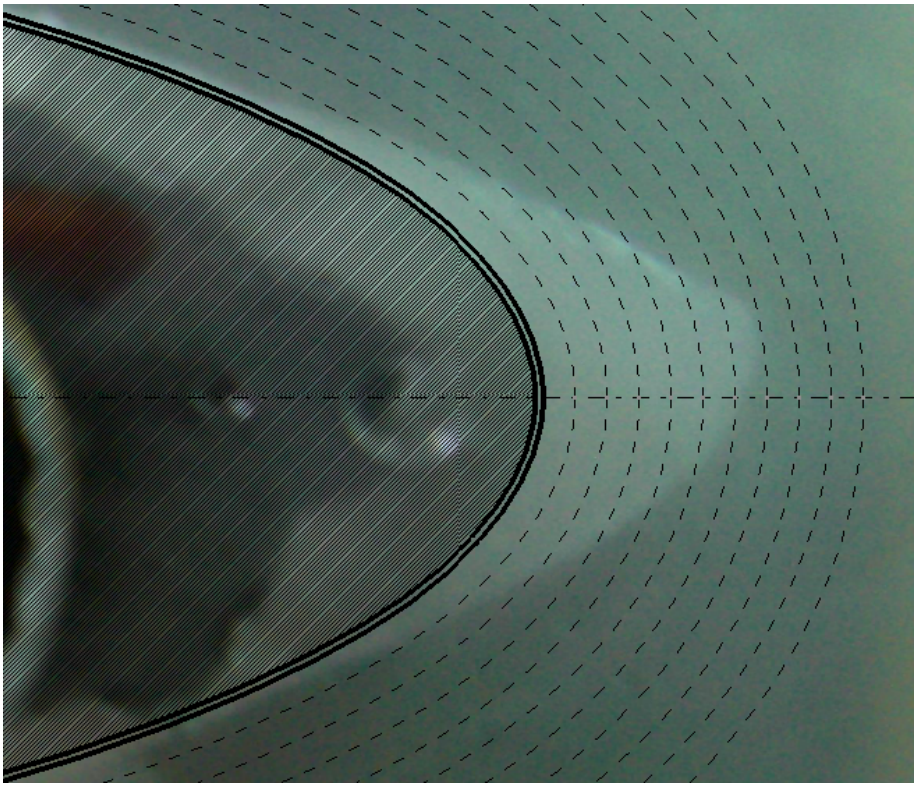

Fig.5.14 Typical ice shape accreted on the EHCLE prototype under icing conditions ITC5 with power-OFF (4 minutes RUN duration, dashed lines show 1[mm] offset)

Preliminary Icing test showed regular ice shapes following the leading edge profile with constant tendency to form a single horn on the top surface. Ice type was observed to be mixed type with a tendency to start accretion as rime type and continuing as mixed type with prevailing glaze appearance on top and bottom ice shape extremities. Preliminary Icing tests have been performed several times both to check the repeatability of measured temperatures and to measure the ice shape geometry and weight for ice accretion rate calculation.

Ice accretion rate as already shown within paragraph 2.2 was of $\boldsymbol{M_A}$= 0.025 [g s^{-1}] with highest thickness ranging 6÷10[mm] in the zone on top of the stagnation point and lowest thickness ranging 1÷2[mm] in the area at top and bottom limits of the heated area.

Hereinafter the typical ice shape is shown as accreted and as detached from the prototype.

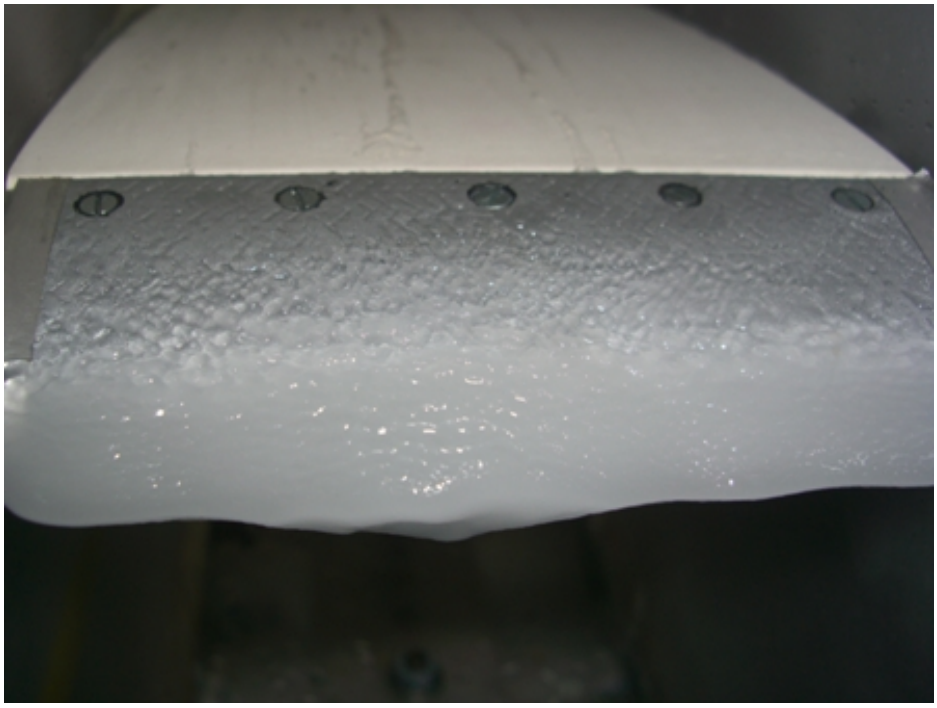

Fig.5.15 Typical ice shape on the EHCLE prototype (ITC5 conditions)

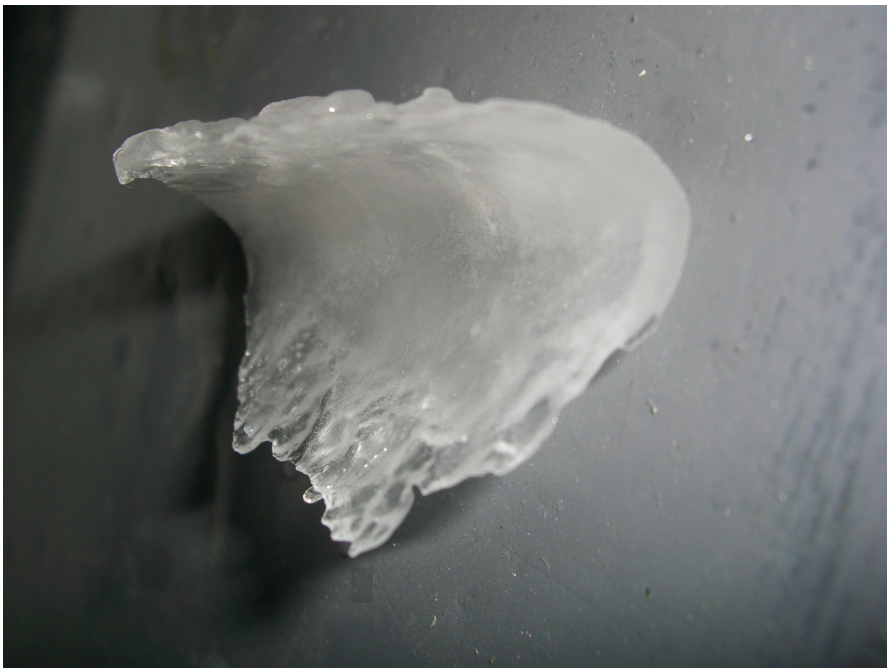

Fig.5.16 Typical ice shape detached from the EHCLE prototype (ITC5 icing conditions)

5.7 Preliminary tests with insufficient power for "Running Wet"

When measured external surface temperature was below 0[°C], under ITC5 icing conditions, continuous ice accretion was observed all over the leading edge, with an accretion peak around the stagnation point and some accretion reduction at top and bottom limits of the heated area. In these last locations the reduced accretion was quite irregular and difficult to quantify in relation to the increase of the supplied power density.

When measured external surface temperature was above 0[°C] temporary ice accretion was observed in the area between the stagnation point and the top limit of the heated area (with an ice accretion peak in the stagnation point area) but it was cyclically wiped away by the wind. This interesting result was essential to the complete understanding of the EHCLE IPS functionality. It shows, in fact, that the power required for a "running wet" functional mode could be reduced increasing the power density only in the stagnation point area, reducing it at top limit of the heated area and reducing it even more at bottom limit of the heated area whilst the EHCLE IPS tested in the present work has an uniform power density distribution. This was an expected result which couldn't be avoided because of the prototype reduced dimensions its consequent manufacturing complications.

Along with the cyclic accretion and wiping of ice a consistent amount of runback ice was observed for this type of tests. Relevant RUNS are hereinafter reported with some explanatory picture taken during and after this type of tests.

It is interesting to point out that the T_{IS} measured during the tests with insufficient power for running wet differ from top to bottom and the T_{IS} measured behind the stagnation point is always higher than those at top and bottom limits of the heated area. As we already explained previously the T_{IS} measured on the inner surface can be transformed in external surface temperature knowing the temperature gradient, which we do thanks to the good accuracy of the analytical model. Therefore the higher T_{IS} measured behind the stagnation point goes in parallel with an higher temperature of the external surface in the stagnation point which at first look could appear hard to explain. This increase of temperature can be explained though thanks to visualization of the phenomena registered during these type of tests. Ice in fact was accreting at stagnation point first and then all along the leading edge offering a shield to the leading edge itself which could not exchange heat anymore with a consequent increase of temperature behind the ice shape. Even when the power supplied was able to bring the surface temperature above 0[°C] ice was still accreting but it was wiped away by the stream offering a temporary shield repeatedly with same effect which obviously is fading down approaching the running wet power functionality.

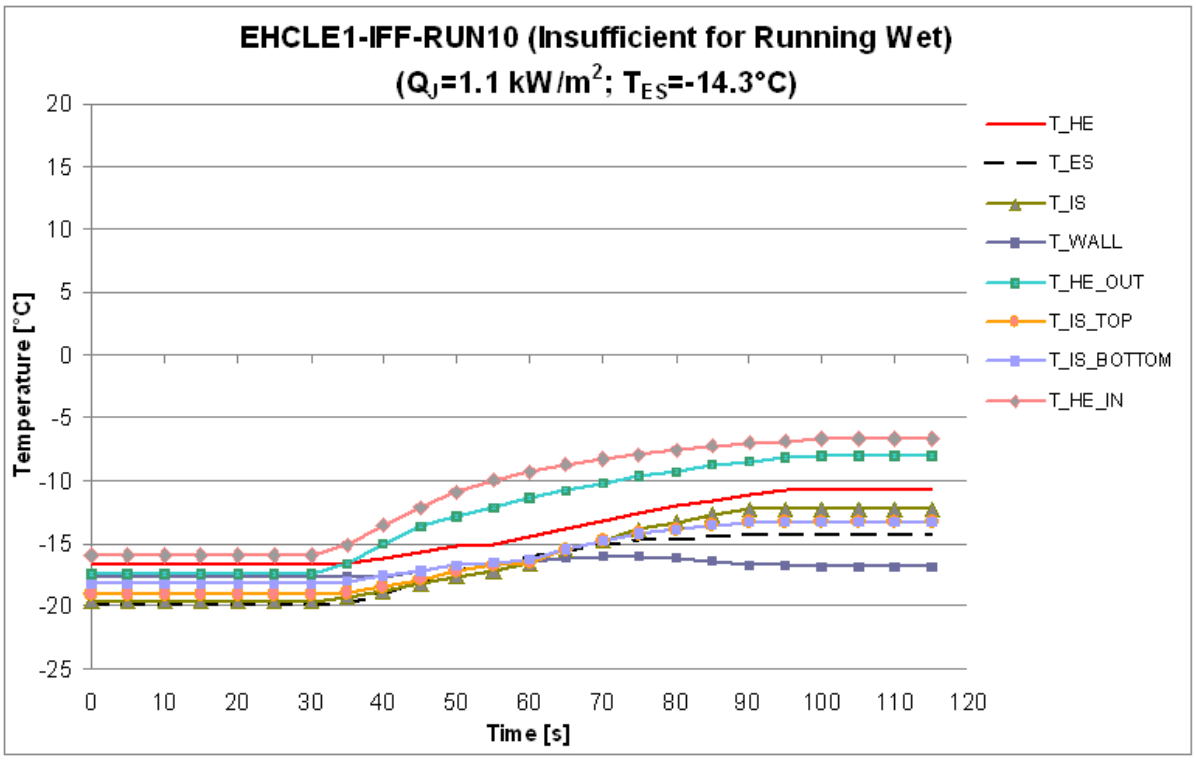

Fig.5.17 Temperature plot relevant to the run EHCLE1-IFF-RUN-10 measurements

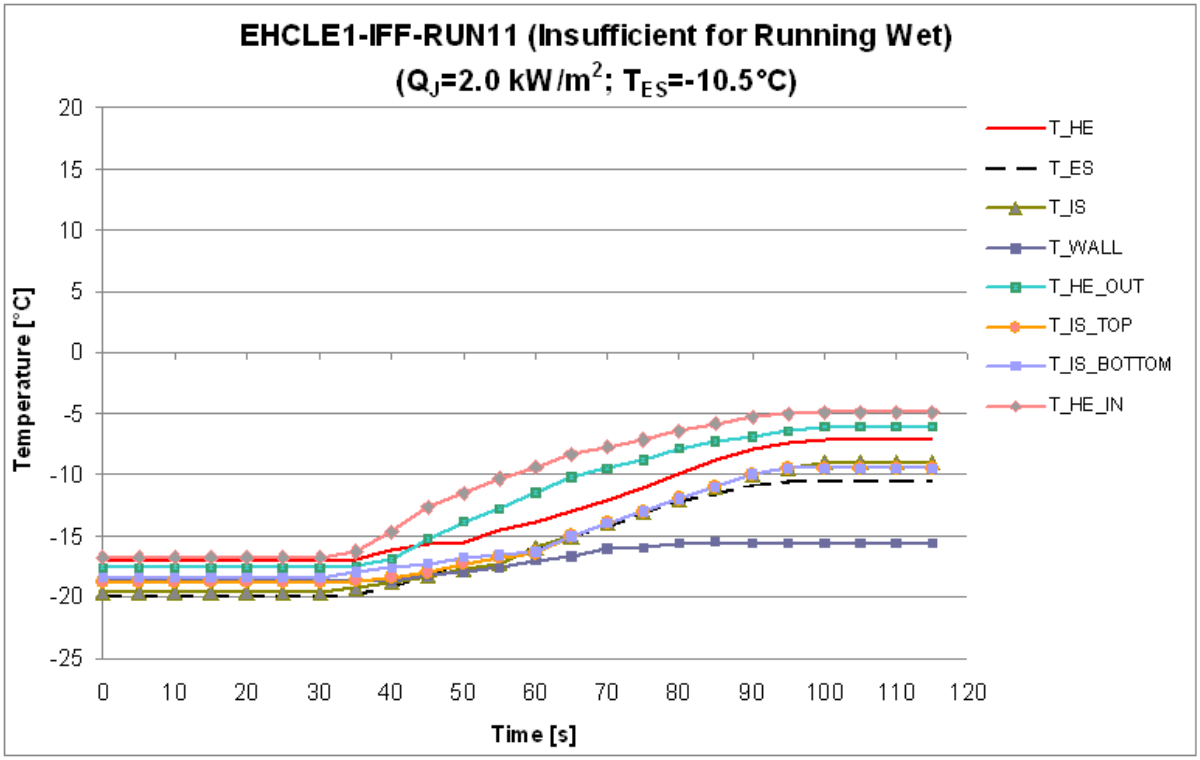

Fig.5.18 Temperature plot relevant to the run EHCLE1-IFF-RUN-11 measurements

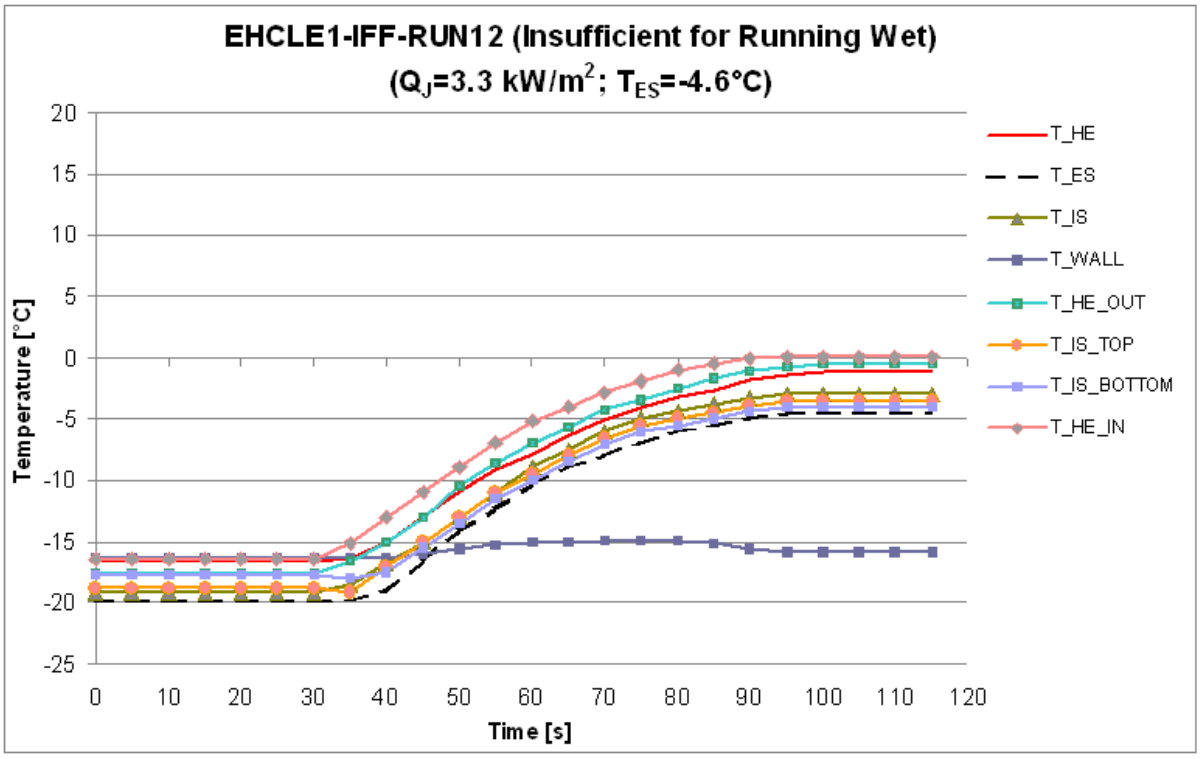

Fig.5.19 Temperature plot relevant to the run EHCLE1-IFF-RUN-12 measurements

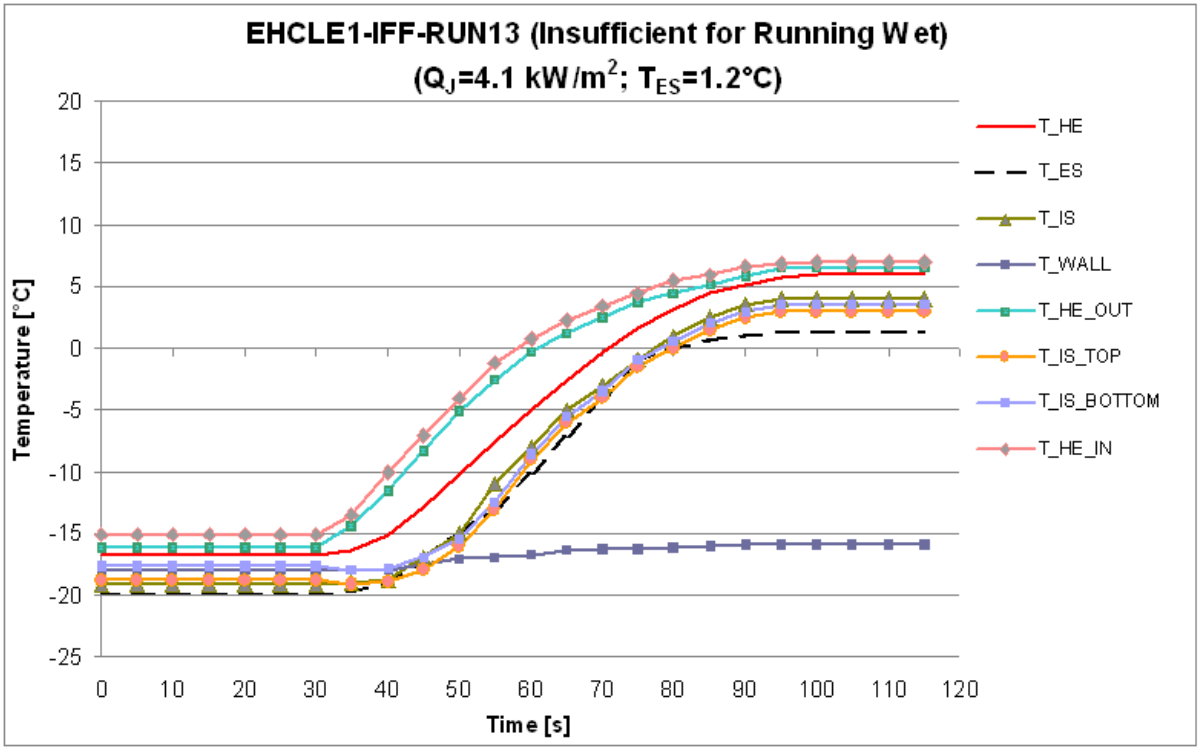

Fig.5.20 Temperature plot relevant to the run EHCLE1-IFF-RUN-13 measurements

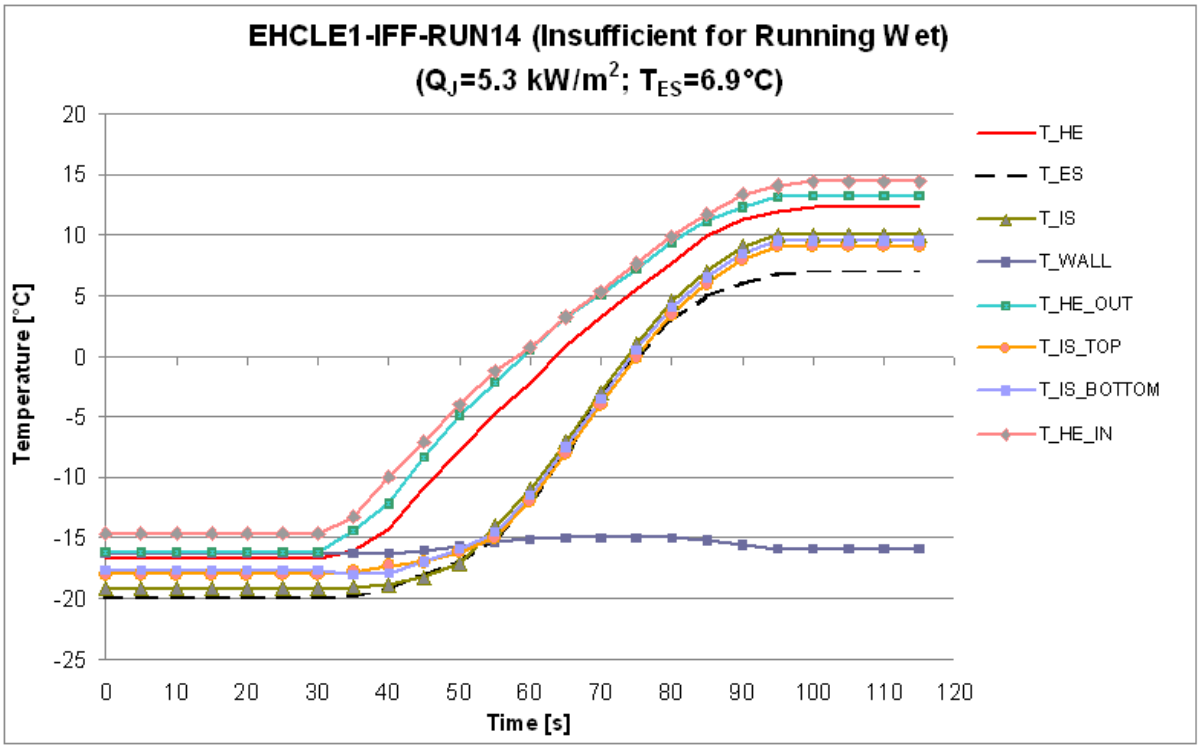

Fig.5.21 Temperature plot relevant to the run EHCLE1-IFF-RUN-14 measurements

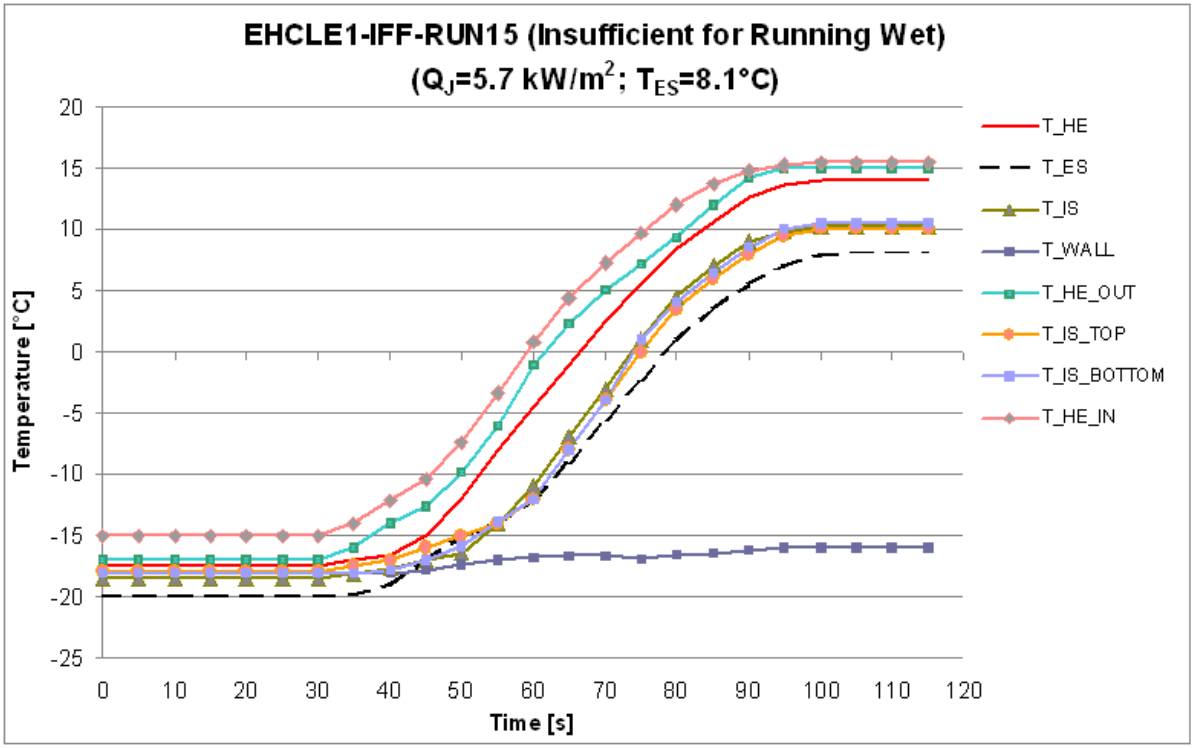

Fig.5.22 Temperature plot relevant to the run EHCLE1-IFF-RUN-15 measurements

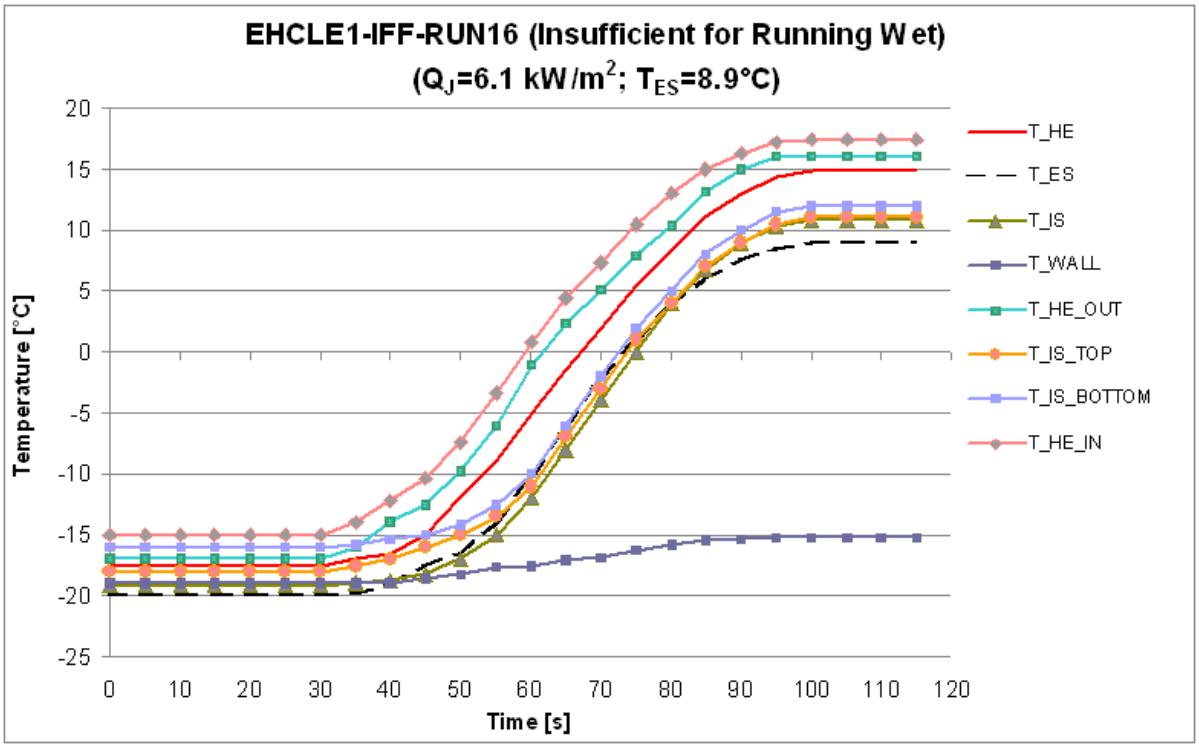

Fig.5.23 Temperature plot relevant to the run EHCLE1-IFF-RUN-16 measurements

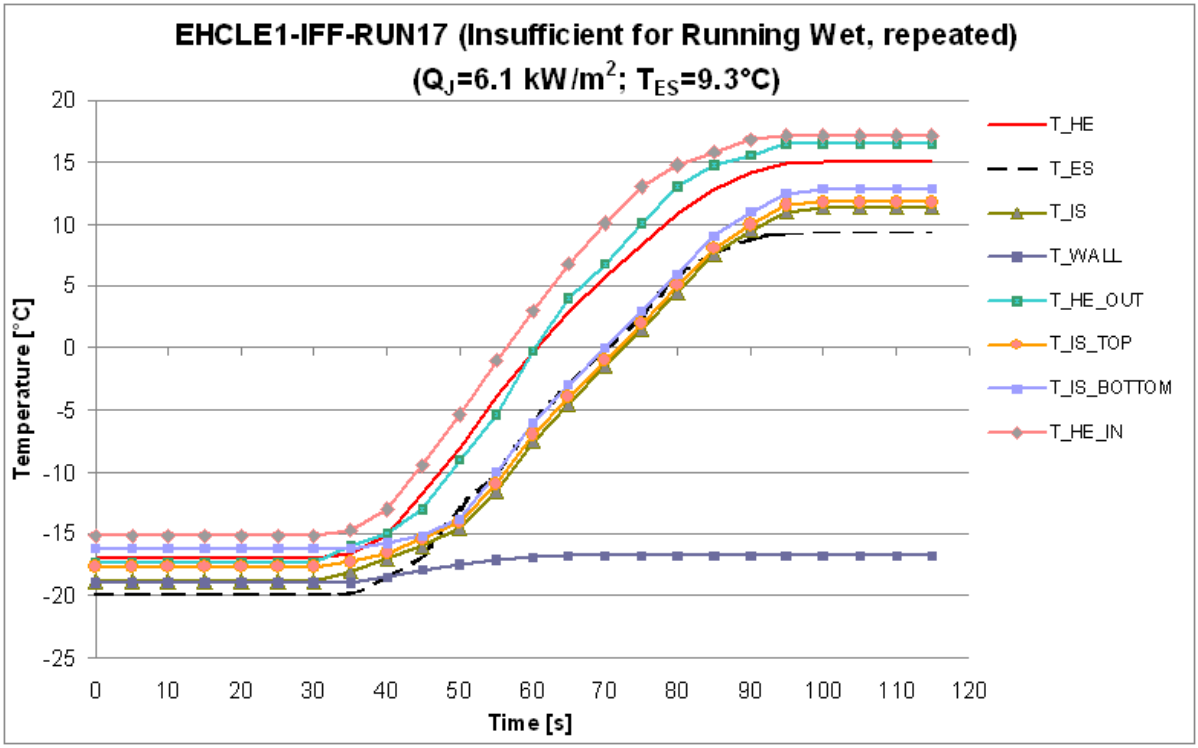

Fig.5.24 Temperature plot relevant to the run EHCLE1-IFF-RUN-17 measurements

Fig.5.25 Residual ice left after a run with barely insufficient power for Running Wet

5.8 Running Wet Tests

When measured external surface temperature was approaching 10[°C], under ITC5 icing conditions, the cyclic phenomena previously described was vanishing, no ice accretion was observed on the leading edge and liquid water was flowing over the leading edge surface itself quite visibly. In these conditions we could assess the "Running Wet" functional mode was achieved. This type of test, characterized by a power density of around 6.5 [kW m^{-2}] was repeated several times and during some of the repetitions an almost instantaneous and almost inappreciable ice accretion was observed in the area of the stagnation point but it vanished in less than a second. This little anomaly shows that it is very difficult to assess a precise and definitive value of the needed power density to achieve running wet functionality but nevertheless the result can be considered achieved at mentioned power density level.

Running wet functionality keeps the leading edge ice-free but the evaporation of impacting water is minimal and runback ice was in fact observed downstream the heated zone with localized ridges in correspondence of the EHCLE top and bottom limits. Relevant RUNs are hereinafter reported with some explanatory picture taken during and after this type of tests.

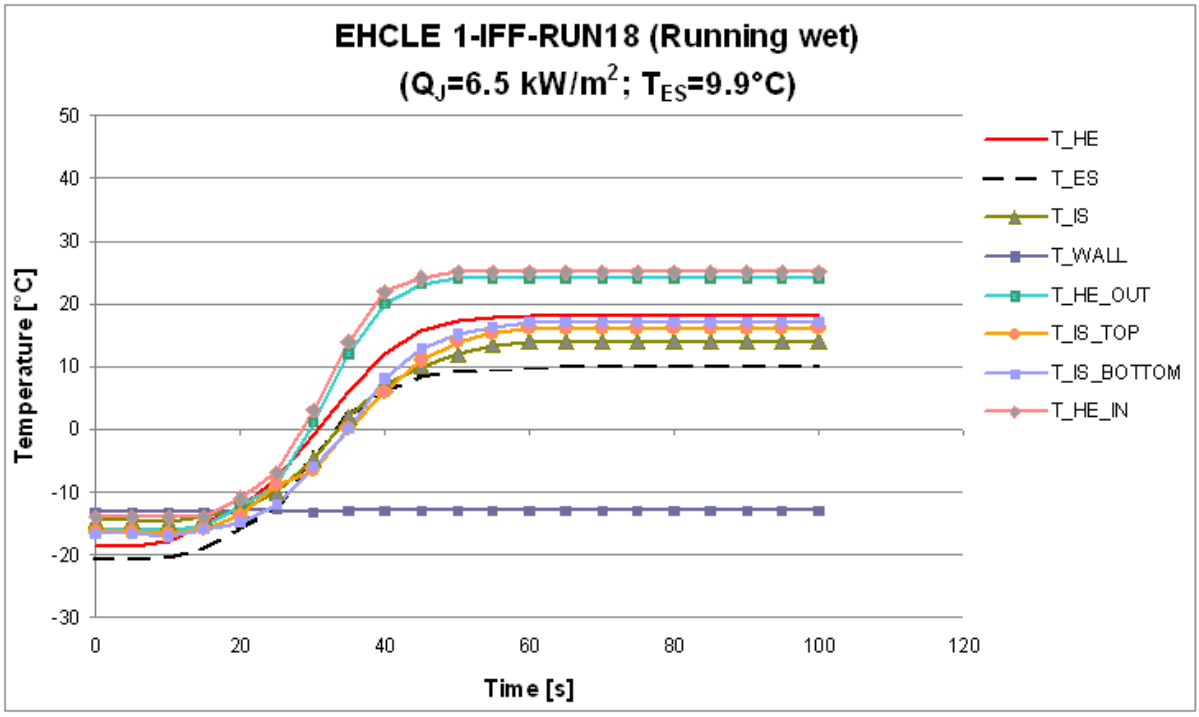

Fig.5.26 Temperature plot relevant to the run EHCLE1-IFF-RUN-18 measurements

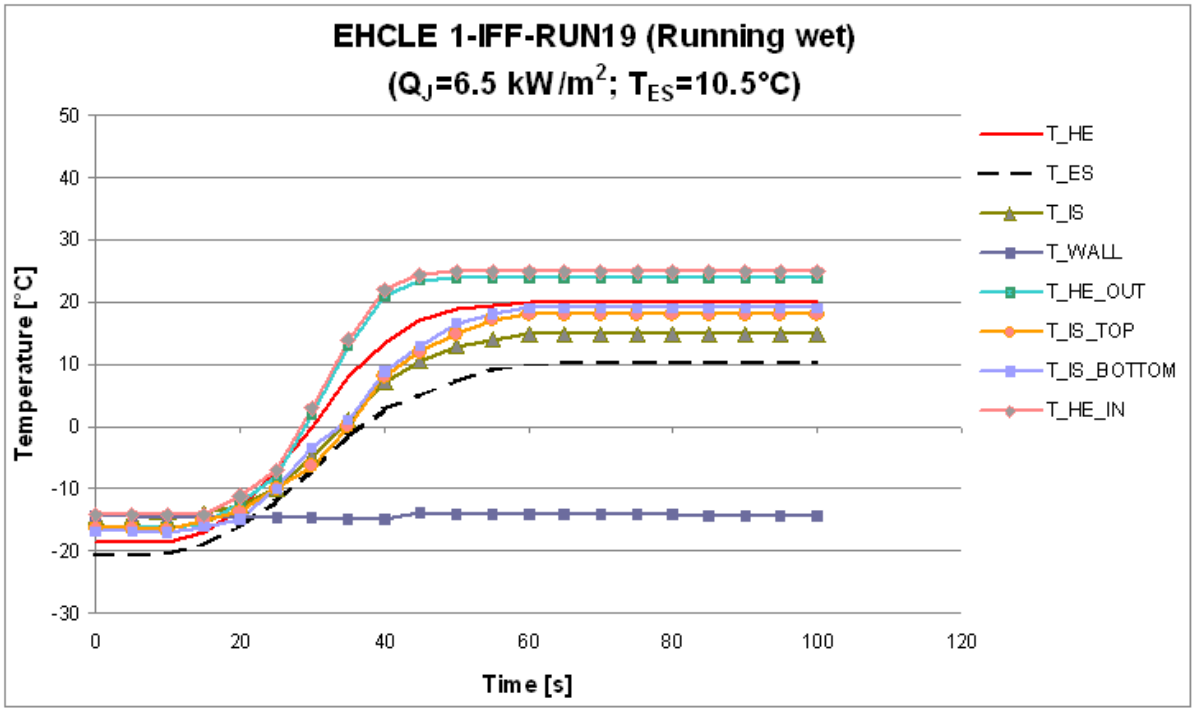

Fig.5.27 Temperature plot relevant to the run EHCLE1-IFF-RUN-19 measurements

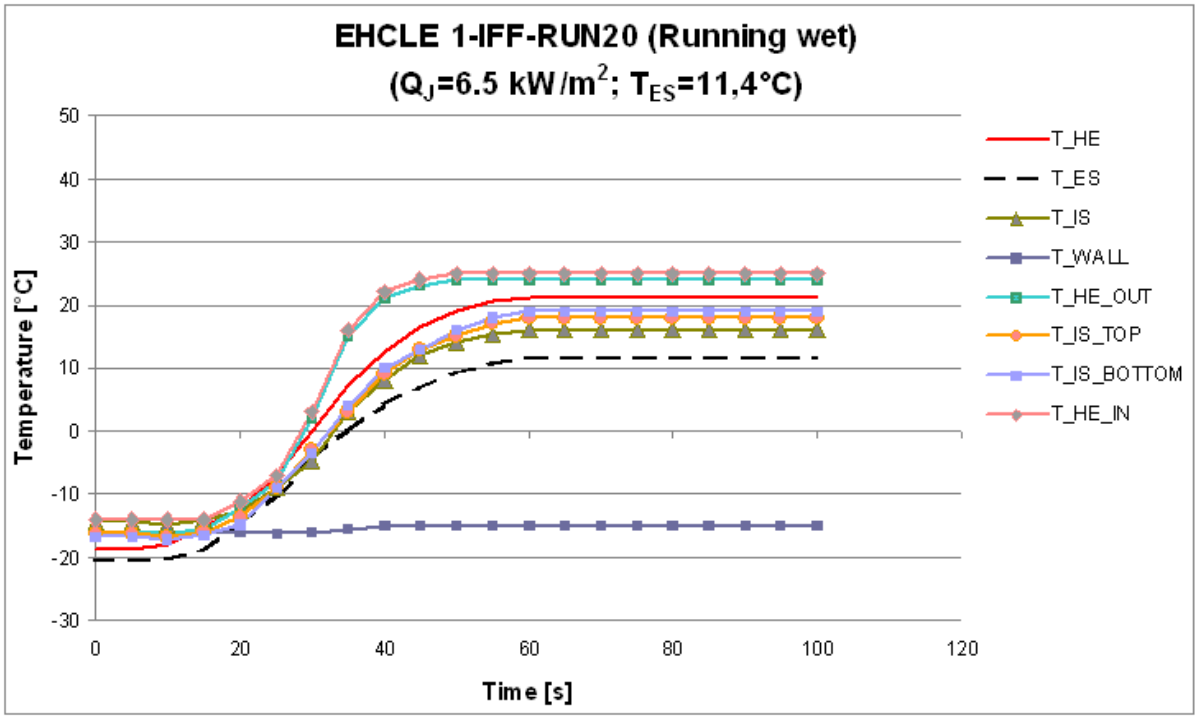

Fig.5.28 Temperature plot relevant to the run EHCLE1-IFF-RUN-20 measurements

Fig.5.29 Typical runback ice left after a Running Wet run (Top)

Fig.5.30 Typical runback ice left after a Running Wet run (Bottom)

5.9 Tests with insufficient power for "Full Evaporation"

When measured external surface temperature was above 10[°C], under ITC5 icing conditions, part of the liquid water was evaporated but this was not visible and no inspections where performed because the phenomena are well known and there was no interest in knowing the amount of water which was evaporating. This amount could anyway be approximately calculated with method previously discussed. Increasing the power density supplied to leading edge from 6.5[kW m^{-2}] to approximately 26.0[kW m^{-2}] liquid water was observed to slip over the leading edge surface and runback ice was also observed to accrete downstream the heated zone. Approaching the surface temperature of 50[°C] it was impossible to observe liquid water slipping on the surface of the leading edge but this circumstance, despite factual, wouldn't represent a real result. Nevertheless runback ice was still observed downstream the heated zone but in continuous decreasing amount along with the increase of the power densities which were supplied. This observation was the clear confirmation that almost all the impinging water was evaporated. Relevant RUNs are hereinafter reported with some explanatory picture taken during and after this type of tests.

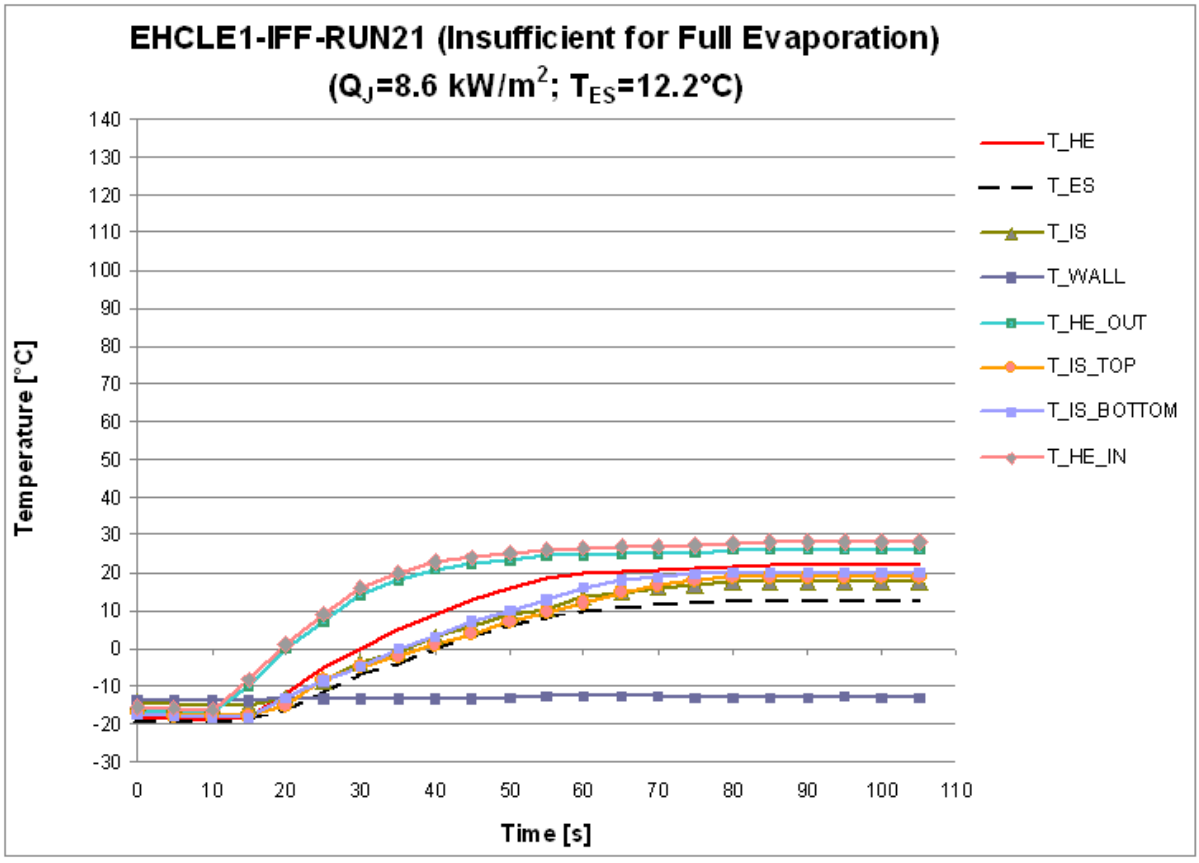

Fig.5.31 Temperature plot relevant to the run EHCLE1-IFF-RUN-21 measurements

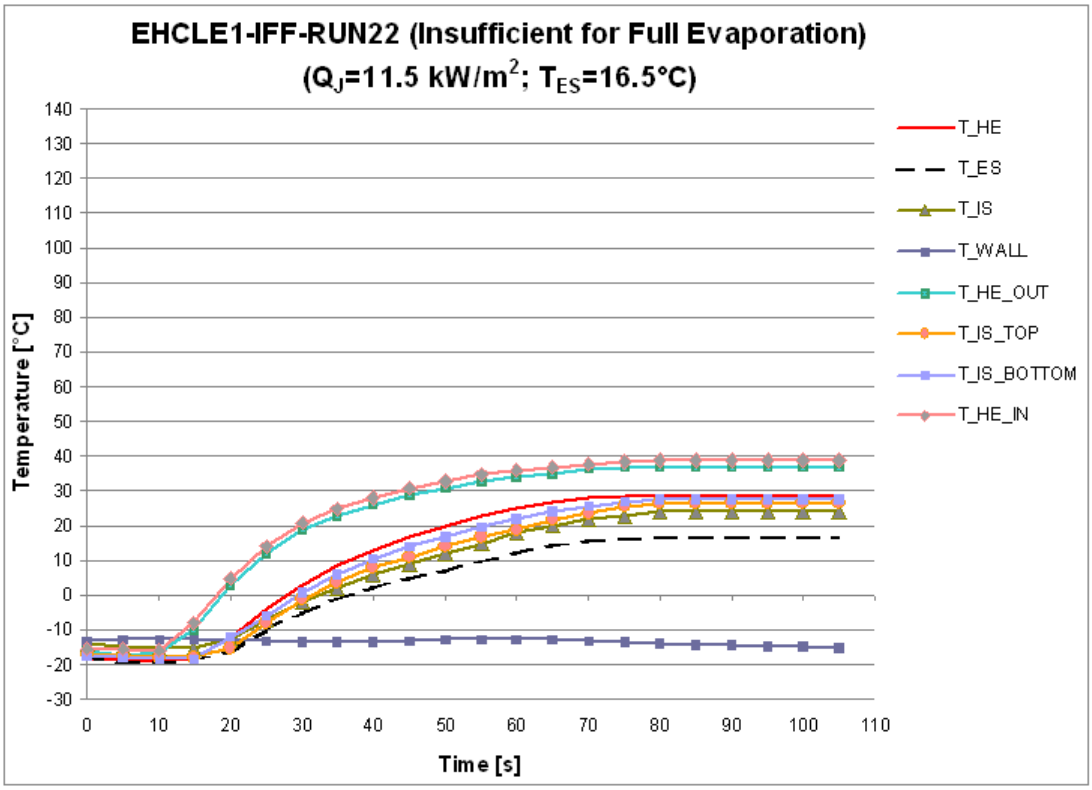

Fig.5.32 Temperature plot relevant to the run EHCLE1-IFF-RUN-22 measurements

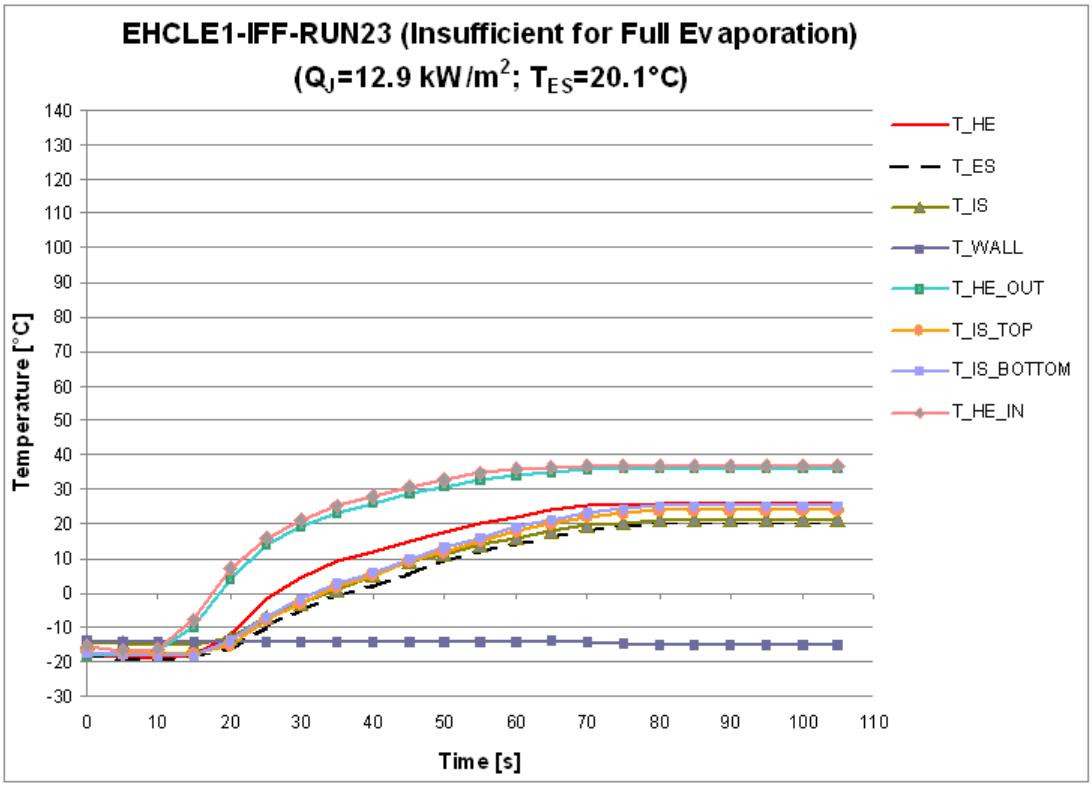

Fig.5.33 Temperature plot relevant to the run EHCLE1-IFF-RUN-23 measurements

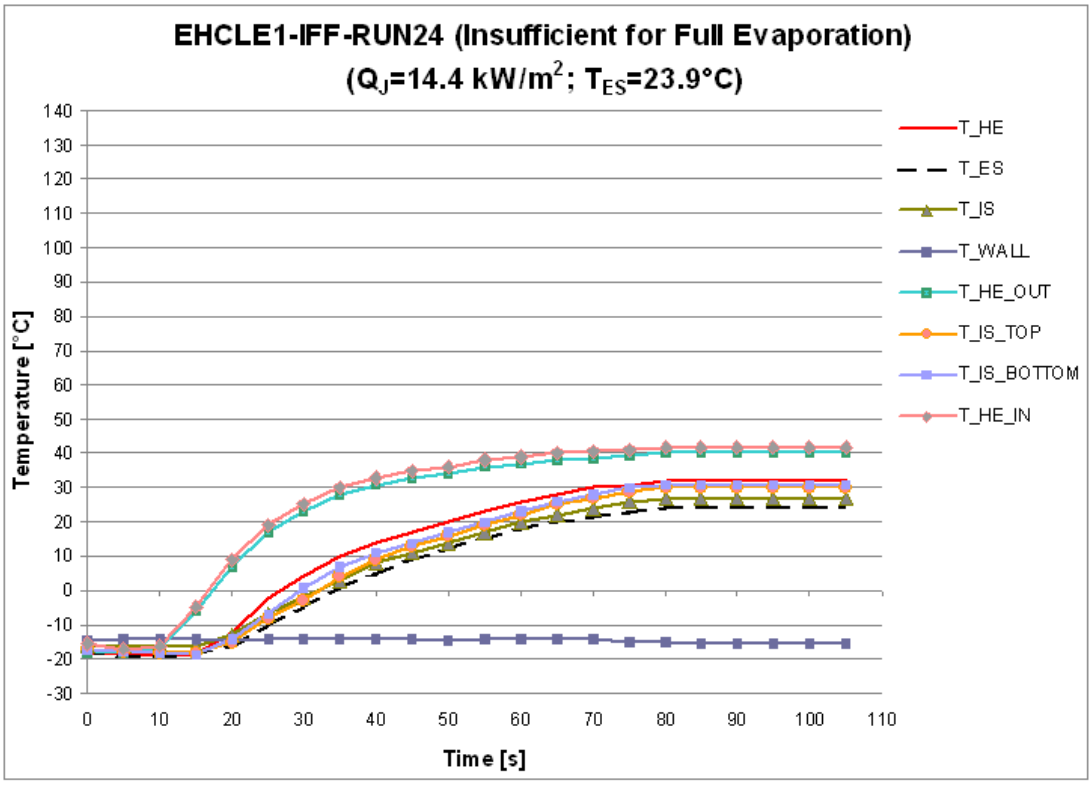

Fig.5.34 Temperature plot relevant to the run EHCLE1-IFF-RUN-24 measurements

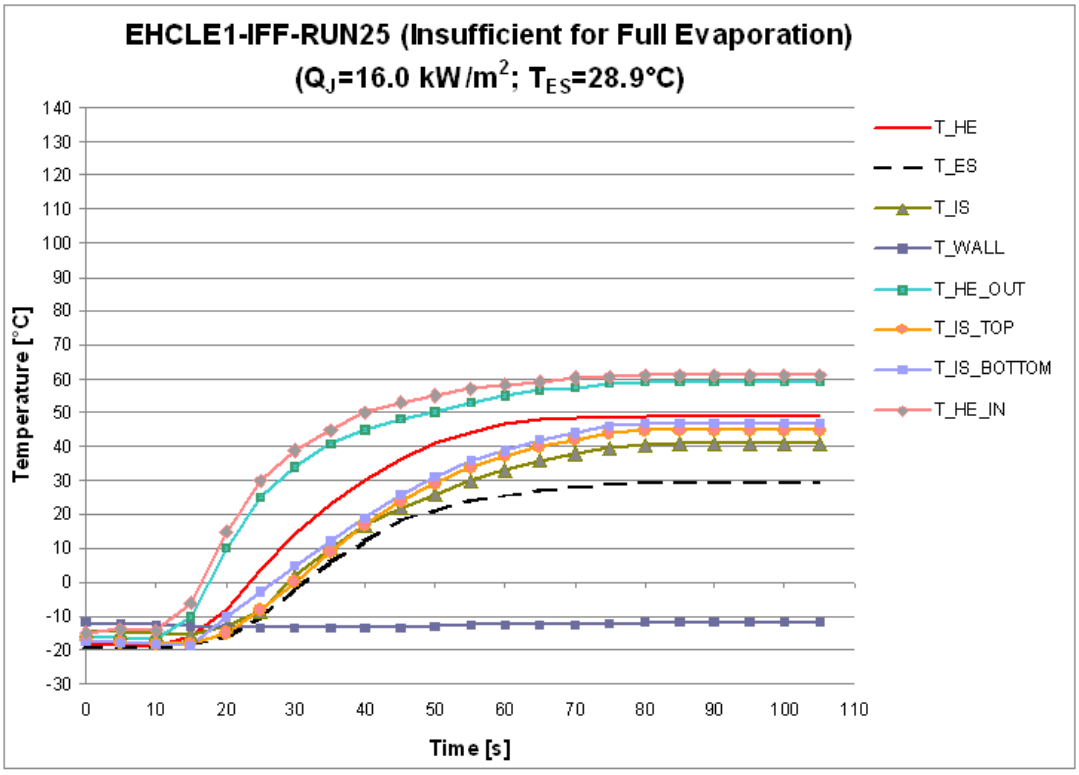

Fig.5.35 Temperature plot relevant to the run EHCLE1-IFF-RUN-25 measurements

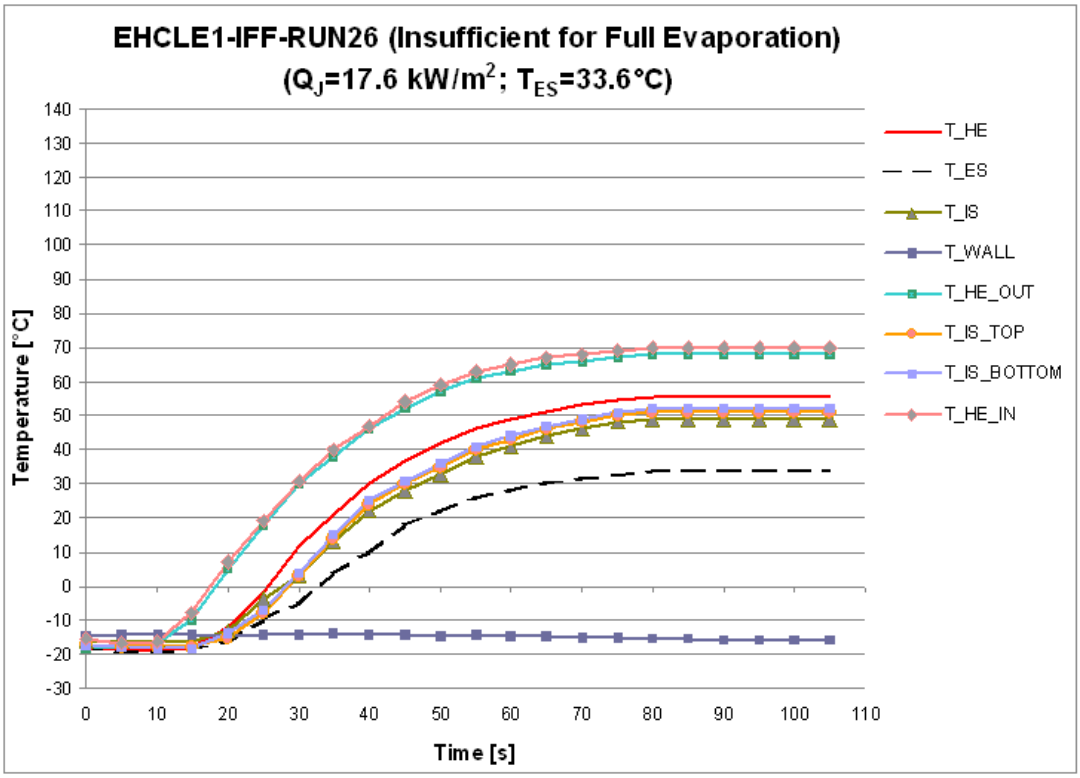

Fig.5.36 Temperature plot relevant to the run EHCLE1-IFF-RUN-26 measurements

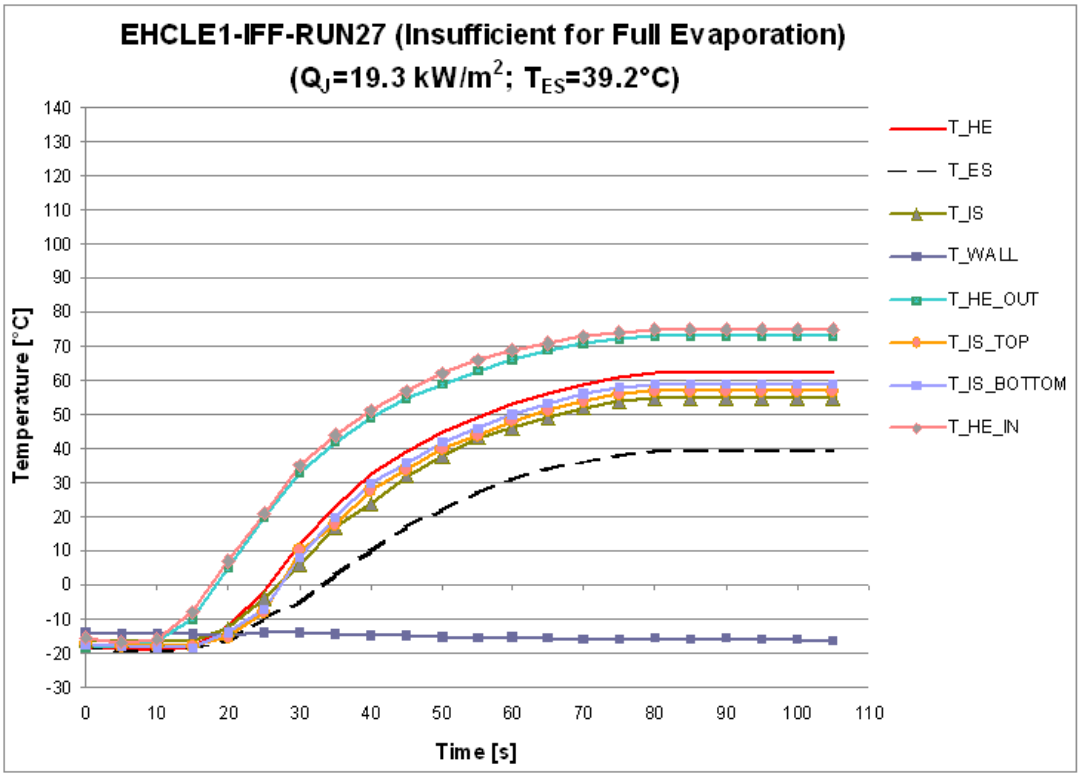

Fig.5.37 Temperature plot relevant to the run EHCLE1-IFF-RUN-27 measurements

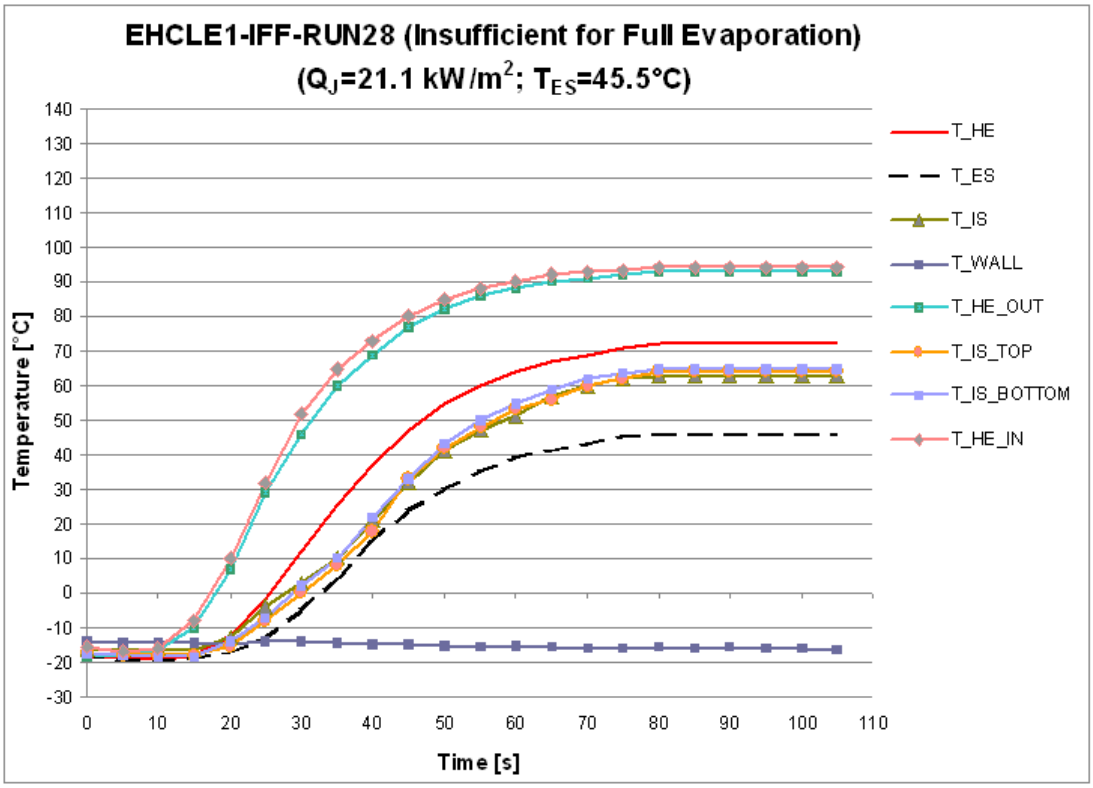

Fig.5.38 Temperature plot relevant to the run EHCLE1-IFF-RUN-28 measurements

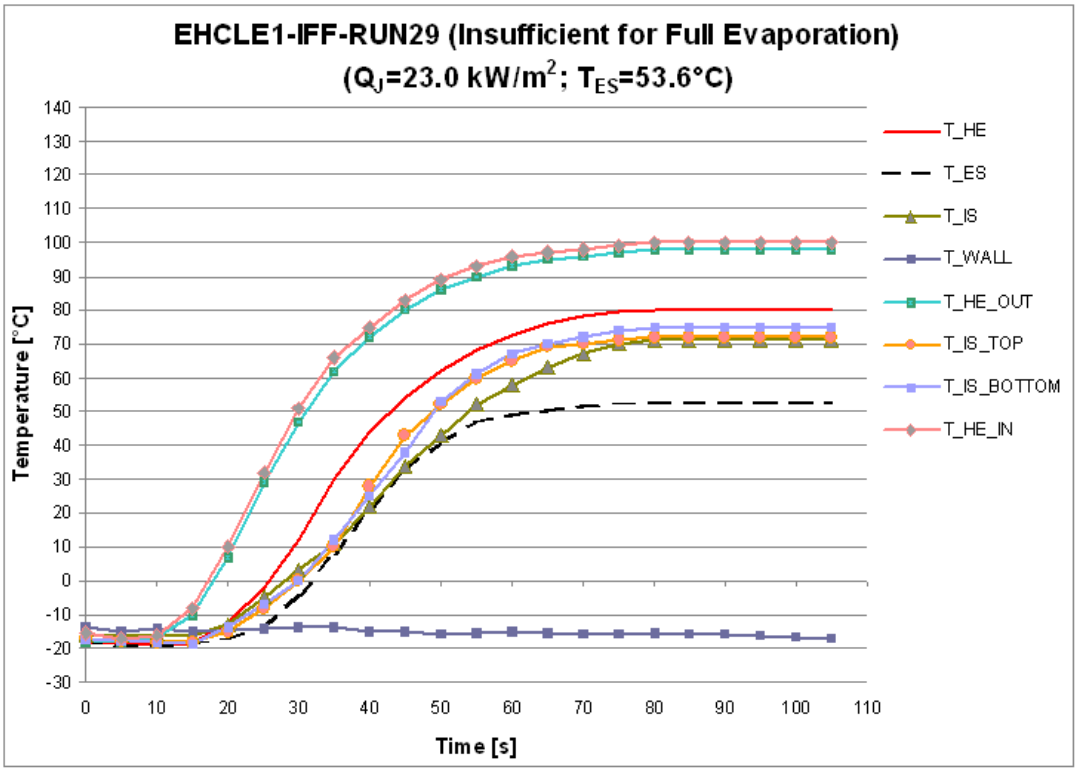

Fig.5.39 Temperature plot relevant to the run EHCLE1-IFF-RUN-29 measurements

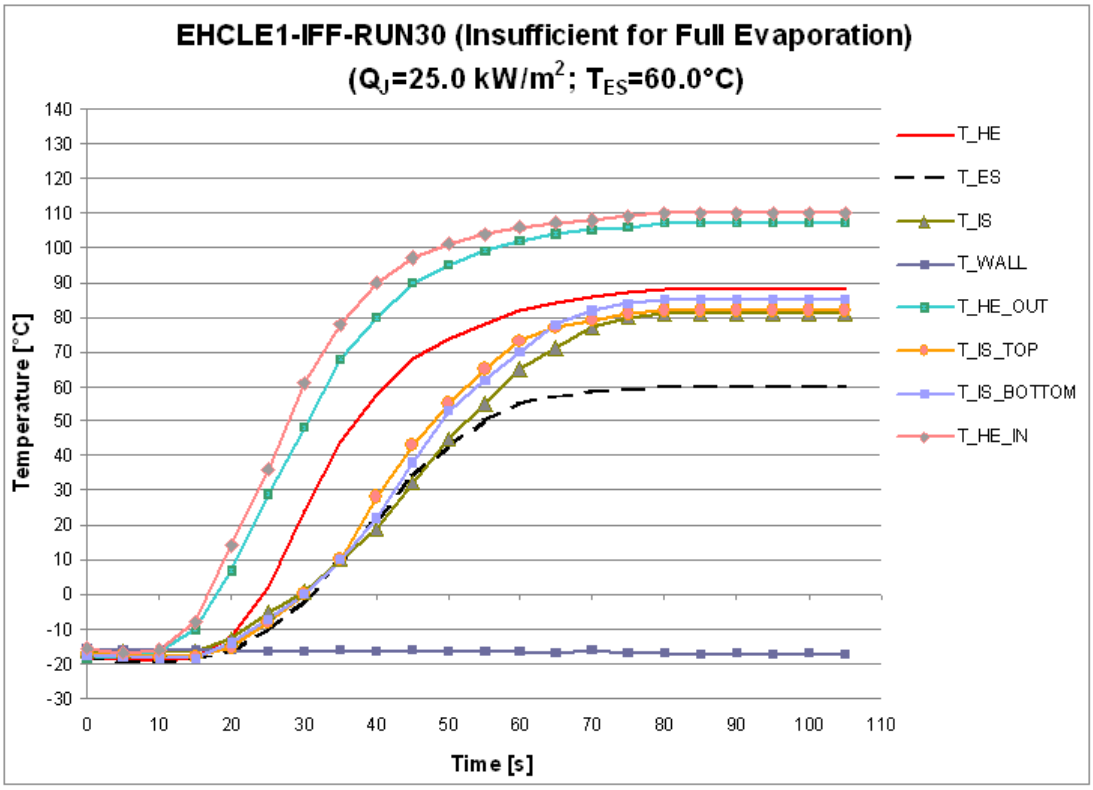

Fig.5.40 Temperature plot relevant to the run EHCLE1-IFF-RUN-30 measurements

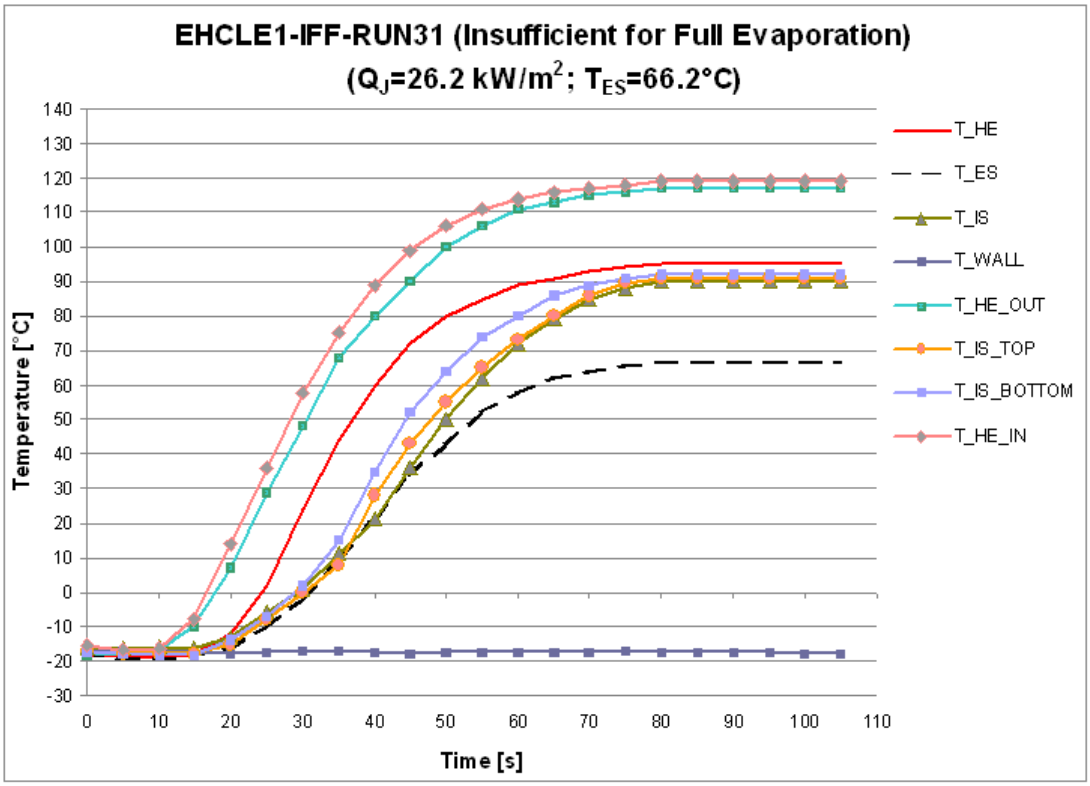

Fig.5.41 Temperature plot relevant to the run EHCLE1-IFF-RUN-31 measurements

Fig.5.42 Typical runback ice left after a run with insufficient power for full evaporation

5.10 Fully Evaporative tests

Approaching the 27.0[kW m^{-2}] power density supplied to the leading, the surface temperature was topping 70[°C], under ITC5 icing conditions, no liquid water was observed to slip on the leading edge and no trace of runback ice was observed downstream the heated zone.

In these conditions we could assess the "Fully Evaporative" functional mode was achieved. This type of test, characterized by a power density of around 27.0 [kW m^{-2}] was performed several times to check the repeatability of the results with an overall acceptable final agreement. A final test was performed at a power density topping 30.0[kW m^{-2}] with similar results, fully evaporative functionality achieved and no runback ice observed. External surface temperature raised almost up to 80[°C] and no anomalies were reported. Obviously the 27.0[kW m^{-2}] is the required power density to reach fully evaporative functionality under the top ITC5 icing conditions of the IFF wind tunnel but, for a final assessment about the effective power densities required for such Icing Protection System to be extended to real applications, more severe icing condition should be explored in a higher scale icing wind tunnel.

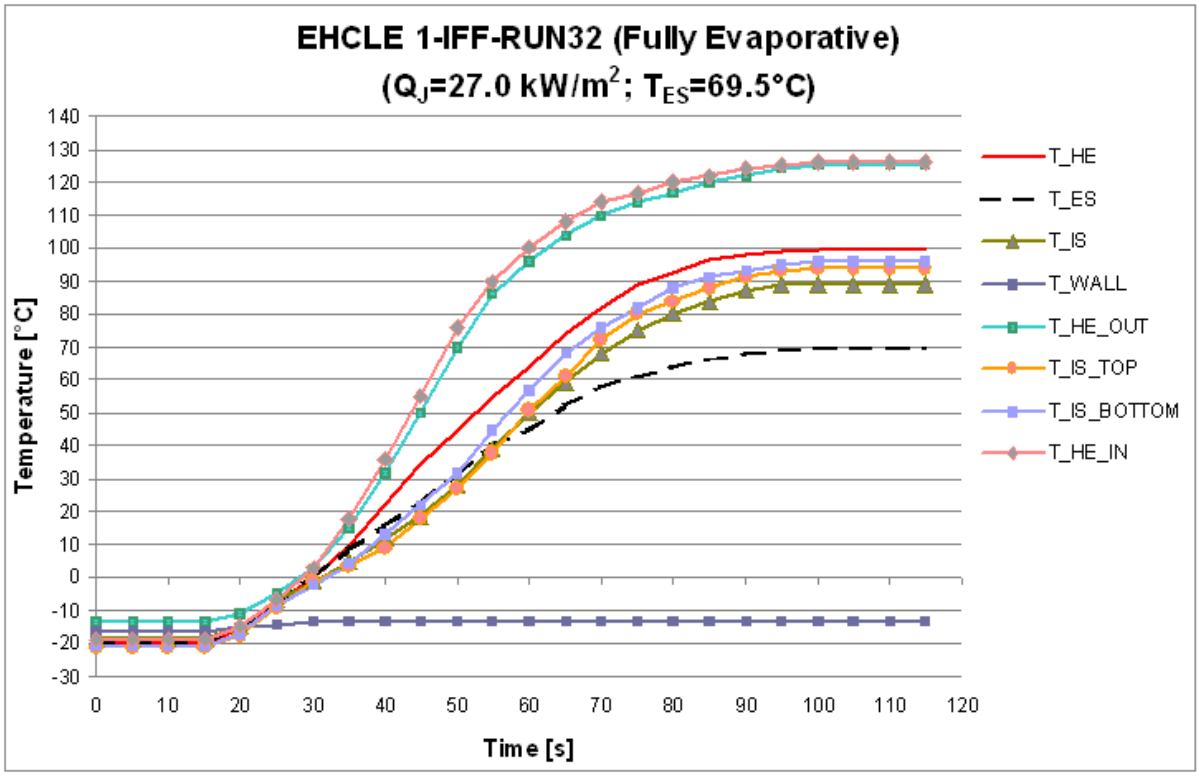

Fig.5.43 Temperature plot relevant to the run EHCLE1-IFF-RUN-32 measurements

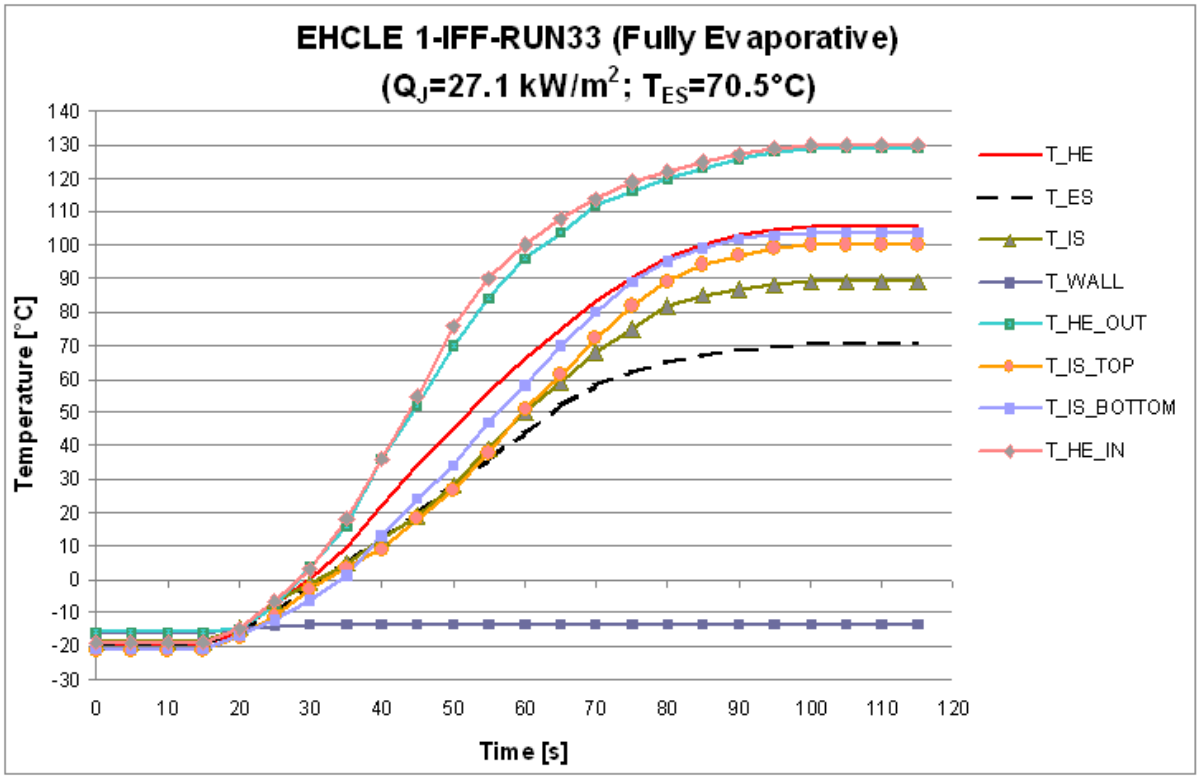

Fig.5.44 Temperature plot relevant to the run EHCLE1-IFF-RUN-33 measurements

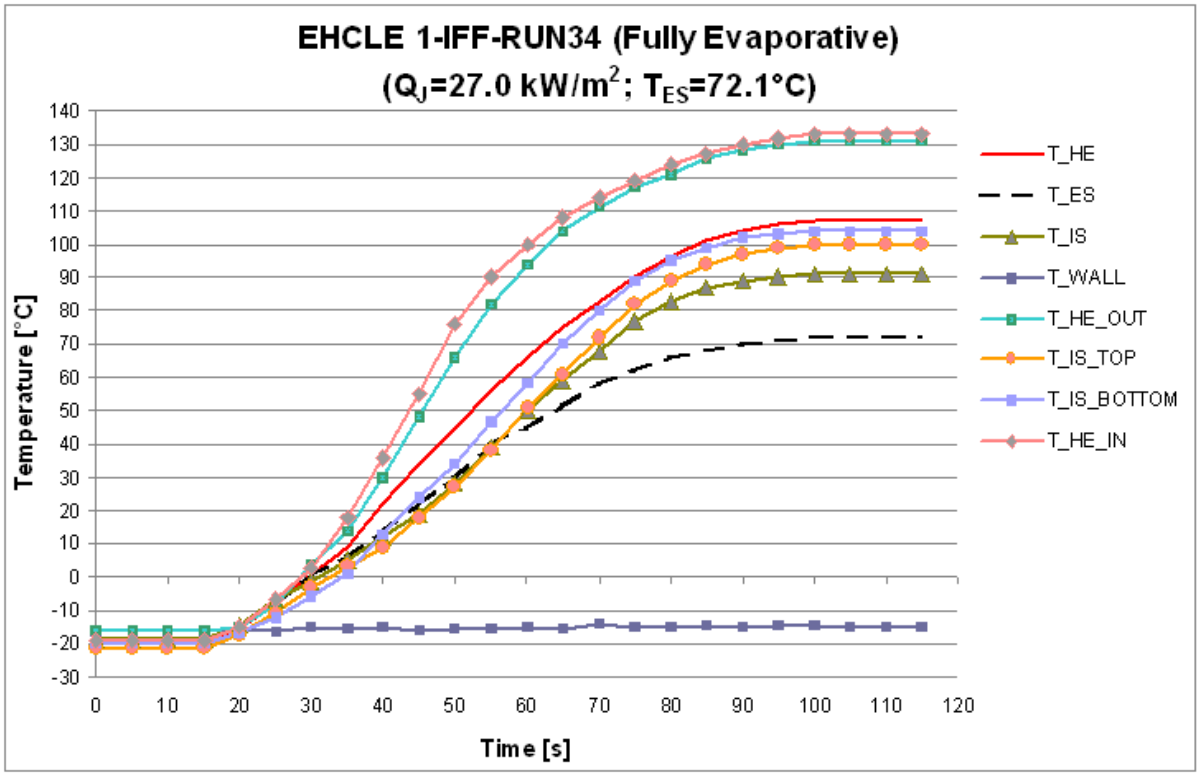

Fig.5.45 Temperature plot relevant to the run EHCLE1-IFF-RUN-34 measurements

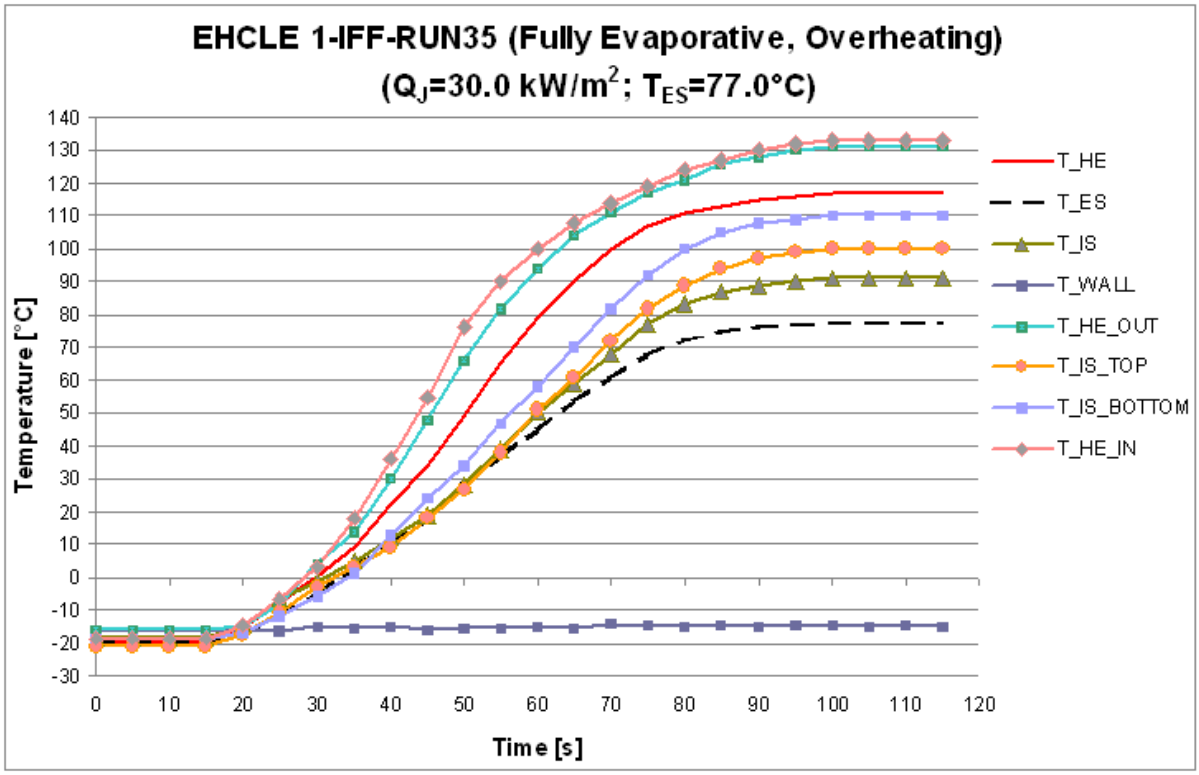

Fig.5.46 Temperature plot relevant to the run EHCLE1-IFF-RUN-35 measurements

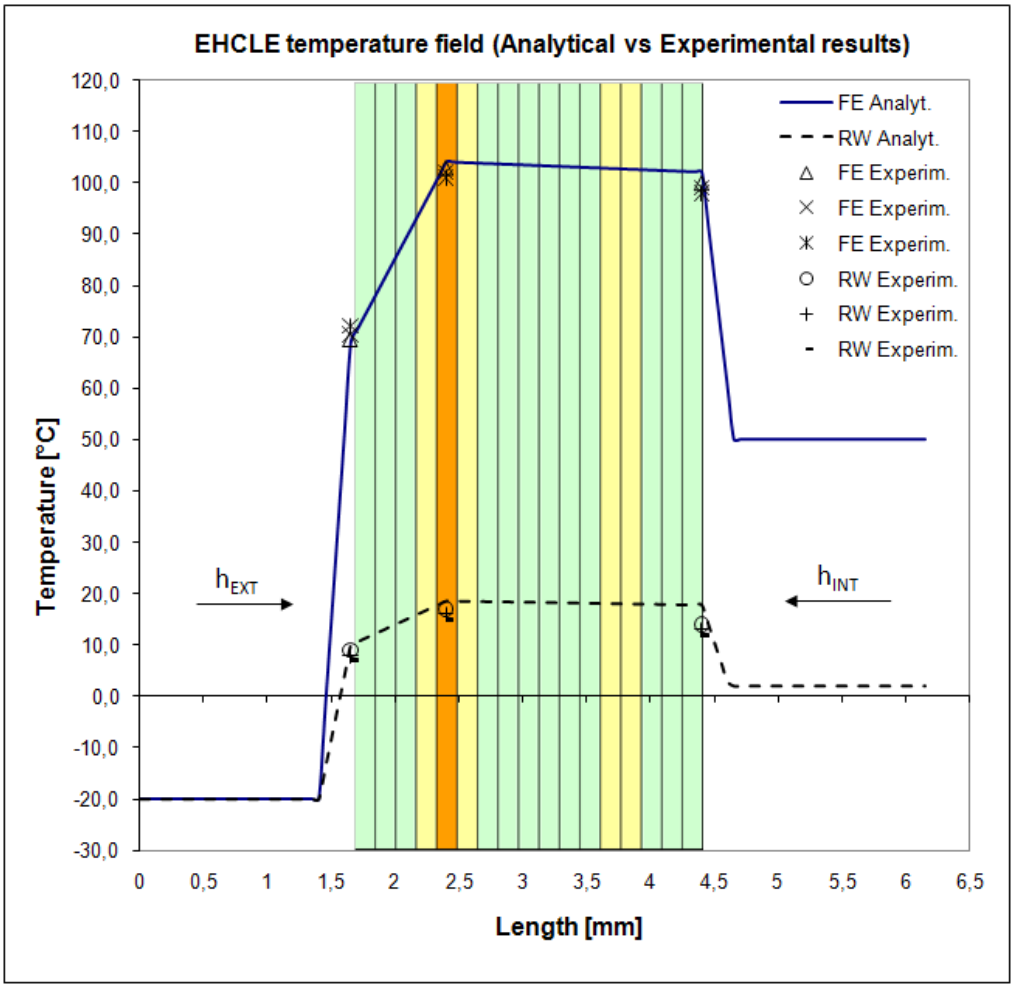

Fig.5.47 Comparison between Analytical and Experimental results "Running Wet" and "Fully Evaporative" functional modes

5.11 Thermal Endurance Test (TET)

Due to the lack of standardized Thermal Endurance Test procedure for this specific application it has been very difficult to schedule and identify a procedure which could produce results to be put in comparison with existing literature. TET has been therefore performed under following general conditions:

- Temperature: test has been performed at RT which has ranged 12÷20 [°C]

- Atmosphere: uncontrolled atmosphere, static air and relative humidity ranging 50÷60%

- Duration: test has been run for a total number of 10^4 cycles with an average of 250 cycles per day for about two months (test was run only during working hours and only in working days either for safety reason and either to monitor the correct functionality of the equipment)

- Thermal Load Cycle: the thermal load cycle has been set imposing a maximum TET temperature equal to 1.5 times the EHCLE maximum operational temperature (~105°C). Maximum TET temperature was reached in static air at RT in about 3 seconds after the timer switched ON the power supply unit. The supplied power was established during test setup at value of 6.8 [W] which is equivalent to a power density $\boldsymbol{Q_J = 9.0}$ [kW m^{-2}] on the coupon total area. After 3 seconds the timer was switching the power supply OFF and temperature started to drop at a an average rate of 4 [°C s^{-1}] reaching the RT conditions back in about 35 [s]. Timer switch-OFF time was set at 117 [s] to give a large margin to the laminate to reach the RT conditions. Temperature cycle evolution within days was monitored minimum once a day applying a flat thermocouple T-type on the external surface (the surface representing the external surface of the leading edge) and in Fig 5.47 the minimum and maximum values registered are reported.

After the Thermal Endurance Test the EHCLE coupon was cut in span and chord directions, examined through micrographic inspection and results compared to micrographic inspections of unstressed samples (Sample5, Sample6 and Sample7). Preliminary results showed in general no significant degradation of the laminate in the area close to the heating element. The fiberglass cloth and the HT resin which directly envelop the resistance showed also no sign of degradation.

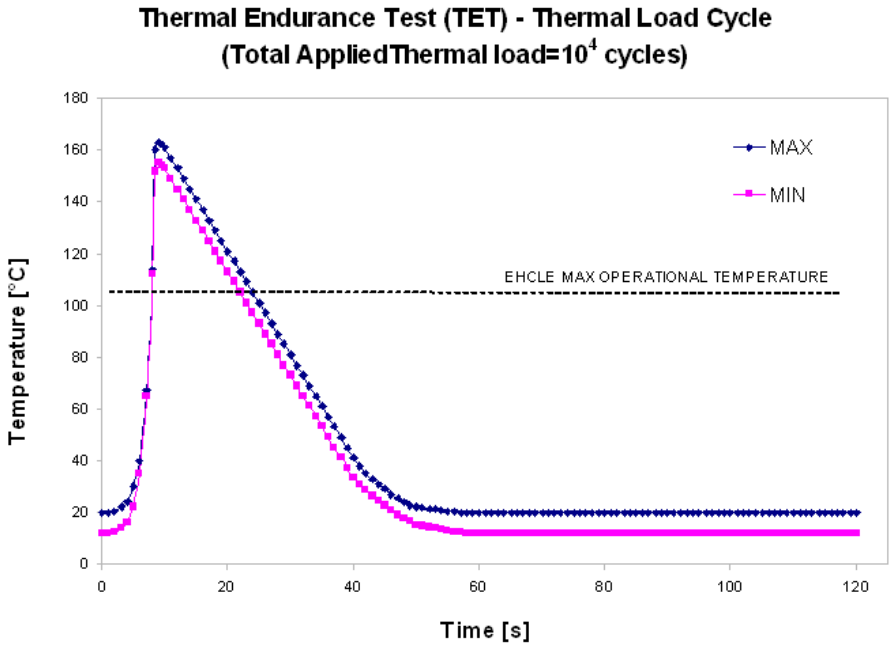

Fig.5.48 Thermal Endurance Test, TET, load cycle envelope

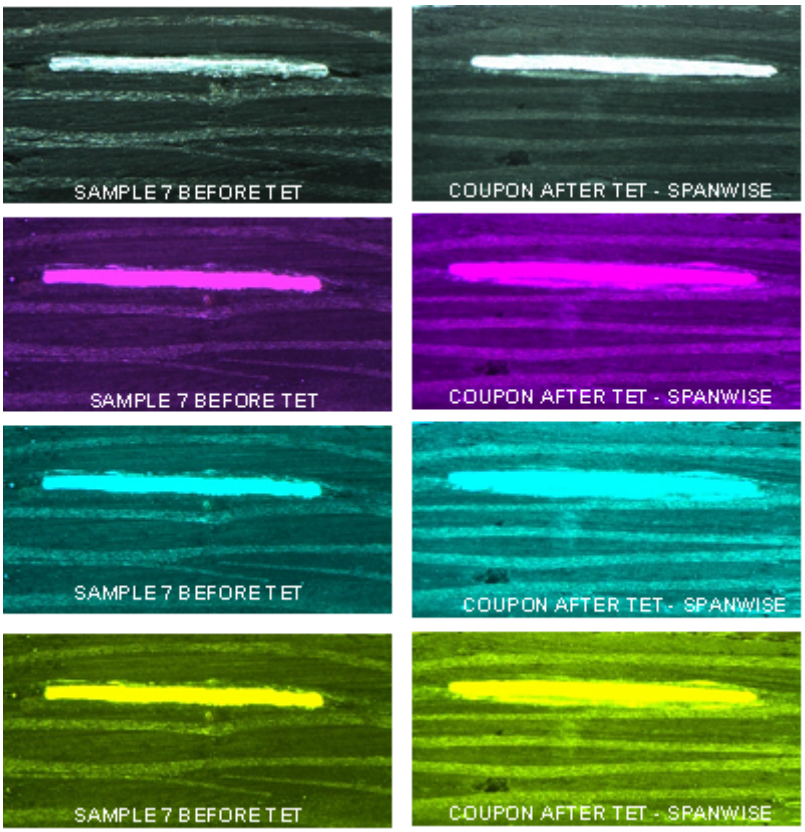

Fig.5.49 Micrographic Inspection before and after the Thermal Endurance Test (example of spanwise cut micro-graphed and filtered to highlight details)

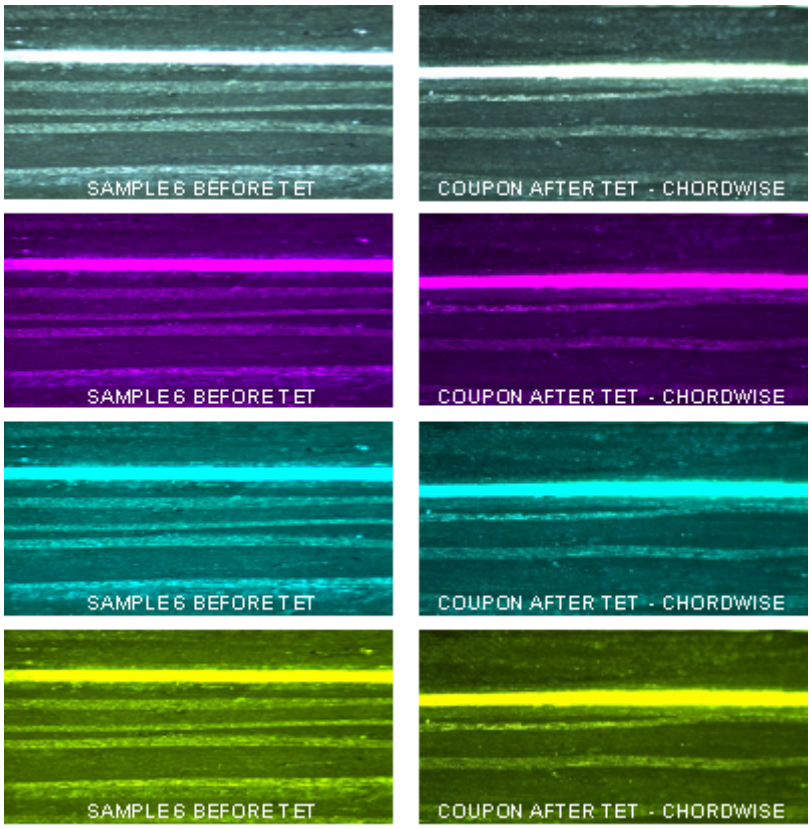

Fig.5.50 Micrographic Inspection before and after the Thermal Endurance Test (example of chordwise cut micro-graphed and filtered to highlight details)

5.12 Scaling methods and an EHCLE concept generalized validation

Scaling methods for icing test has been long debated within the aeronautical scientific and industrial community. Mach number and Reynolds number in this sense play certainly a primary role as also shown in [31][41] and the difficulty to simulate contemporarily both numbers makes the scaling very difficult [42][43].

On one side, from geometrically view point is proven [29] that hybrid wing design of 2D airfoils built up with the identical leading edge and a scaled body (half of the chord and reduced max thickness) reproduces and accretes equivalent ice shapes than full scale airfoil in the same icing flow conditions. This definitely proves that for IPS design and sizing only the leading edge geometry and dimensions play a role. On the other side, purely from a convective heat exchange view point, it would be necessary to simulate a Weber number to parametrize the water film thickness obtaining a proper scaling of the ice accretion [40]. But this last circumstance requires sophisticated techniques which out of scope for the present work. Nevertheless, to achieve a complete icing similarity, it would be necessary to account

for all tolerances which the icing parameters are effected by [37] and therefore, being these parameters function of the specific considered cases, the achieved results will lose anyway their general validity but will be case-specific [38][39].

In the end, for the EHCLE Icing Protection System final validation, basic information can be taken from the present work but, being the icing scaling simulation within the IFF wind tunnel limited by the IFF capabilities, it is necessary to test the system on scale 1:1 geometry under more accurate icing scaling simulation.

In Tab.5.3 a comparison is proposed between the ITC5 icing conditions simulated by the IFF tunnel and a real case at 5000 [m] altitude .

Tab.5.3 Comparison between icing parameters at 5000[m] altitude and those simulated by the IFF wind tunnel

Parameter	Real case (5000m)	IFF	Dimensions
T_0	-20	-20	°C
p	54048	100062	$N\ m^{-2}$
ρ	0,736	1,377	$kg\ m^{-3}$
LWC	0.3 ÷ 2.8	0,6	$g\ m^{-3}$
c_P	1007	1007	$J\ kg^{-1}\ °K^{-1}$
c (chord)	1,415	0,283	m
L_{LE}	0,150	0,03	m
λ	0,0227	0,0226	$W\ m^{-1}\ °K^{-1}$
μ	0,00001628	0,00001622	$kg\ m^{-1}\ s^{-1}$
a	321	340	$m\ s^{-1}$
Pr	0,721	0,722	-
M	0,20	0,20	-
T_{LF}	25	25	°C
Re (T_{LF} , L_{LE})	3,2E+05	1,3E+05	-
h_{cDRY}	54	172	$W\ m^{-2}\ °K^{-1}$
Re_{EXT} (T_0 , c)	4,1E+06	1,6E+06	-

In general we can assume that the simulated Reynolds number achieved under ITC5 conditions within the IFF tunnel (see $\boldsymbol{Re_{EXT}}$ Tab.5.3) is not dramatically far from the 5000[m] one at same Mach number and this is due to the partial compensation obtained having an higher density but a lower chord. On the other hand the simulated Mach number under ITC5

conditions within IFF tunnel is limited to max value of M=0.2 and higher values should be tested affecting both ice accretion and convective heat exchange.

The Dry-convective heat coefficient nevertheless, being calculated at liquid film temperature of 25[°C] (as reference for the fully evaporative case), shows a sensibly lower value at 5000[m] altitude being adversely affected by both lower density and longer leading edge chord $\boldsymbol{L_{LE}}$. This last circumstance is giving an higher potentiality to the EHCLE system due to the fact that it has been tested against a more than 3 times bigger value of $\boldsymbol{hc_{DRY}}$ which will partly compensate the higher power densities required to operate in more severe icing conditions on scale 1:1.

6 Conclusions

An investigation was conducted in the Aerospace Engineering Department (DIAS) at Federico II University of Naples aiming to evaluate the feasibility and the performance of an electrically heated composite leading edge for anti-icing and de-icing applications. A 283 [mm] chord NACA0012 airfoil prototype was designed, manufactured and equipped with an High Temperature hybrid carbon-glass composite leading edge, 2.7[mm] thick, with embedded Ni-Cr heating element. The average power densities supplied to the leading edge were ranging 1.0÷30.0 [kW m^{-2}]. Thermal tests were performed under fixed icing conditions with zero AOA, Mach=0.2, total temperature of -20 [°C], liquid water content LWC=0.6 [g m^{-3}], average mean volume droplet diameter MVD=35 [μm]. Under these icing conditions mixed ice accretion type was observed and "Running Wet" and "Fully Evaporative" functional modes were experimentally experienced at 6.5[kW m^{-2}] and 27.0[kW m^{-2}] respectively, in reasonable agreement with analytical forecast. In fully evaporative mode the max temperature recorded within the laminate was 110[°C]. A preliminary room temperature thermal endurance test has been run using a flat coupon fully representative of the leading edge laminate, for 10^4 cycles of 120[s] duration each, with recorded peak thermal load ranging 155÷165[°C]. Micrographic inspection of the endurance coupon showed no evidence of laminate degradation in comparison to the unstressed laminate. The achieved results, despite obtained under limited icing conditions imposed by the IFF wind tunnel, showed great potentialities for the Electrical Heated Composite Leading Edge (EHCLE) which has been constantly working below 60% of its maximum operative temperatures under the given icing conditions and the explored power densities. This potentiality justifies the need for future development in a larger scale under more severe icing conditions for a final assessment about both limit capabilities and applicability of such Icing Protection System to real aircrafts.

References

[1] CAA, “Aircraft Icing Handbook”, 2000

[2] FAA, “Pilot guide - Flight in icing conditions,” AC 091-74, 2002

[3] FAA, "Flight in Icing Conditions", AC 025-1419-1, 1999

[4] K.T. Brown, M.J. Layland, D.B. Sweet, “High Efficiency Ice Protection System for Aircraft Engine Lips”, SAE 2004-01-3110, 2004

[5] H.A. Ross, R. Zumwalt, G. Provose, J. Padmanabhan, V. Thomson, J. Riley, J. “FAA Icing Handbook”, DOT/FAA/CT-88/8-2, 1991

[6] A.R. Lewis, A.P. Jones, “A flight investigation about exhaust-heat de-icing”, NACA-TN-783, 1940

[7] V.H. Gray, U.H. Von Glahn, “Heat requirements for ice protection of a cyclically gas heated 36° swept airfoil with partial-span leading edge slat”, NACA-RM-E56B23, 1956

[8] G.C. Botura, D. Sweet, “Concept Development of Low Power Electro-thermal De-icing System”, AIAA 2006-864, 2006

[9] B. Burkett, M. Mitrovic, D. Sweet, G.C. Botura, D. Burner, K. Brown, M. Layland, “Development and Test Results on a High Efficiency Ice Protection System”, AIAA 2006-863, 2006

[10] R.J. Ranaudo, K.L. Mikkelsen, R. McKnight, P.J. Perkins Jr., “Performance degradation of a typical twin engine commuter type aircraft in measured natural icing conditions”, NASA TM83564, 1984

[11] W. Olsen, R. Shaw, J. Newton, “Ice Shapes and the Resulting Drag Increase for a NACA 0012 Airfoil,” NASA TM 83556, 1984

[12] J.P. Lewis, D.T. Bowden, “Preliminary investigation of cyclic de-icing of an airfoil using an external electric heater”, NACA RM-E51J30, 1952

[13] G.P. Russo, A. Esposito, F. de Rosa, “Icing Tests in a Small Blow-Down Wind Tunnel“, FDMP, vol.196, no.1, pp.1-16, 2009

[14] S.F. Hoerner, “Fluid-Dynamic Lift”, 1975

[15] Bowden, D.T., "Effect of Pneumatic De-Icers and Ice Formations on Aerodynamic Character of an Airfoil," NACA TN-3564, February, 1956. 286

[16] Y.A. Cenghel, “Introduction to Thermodynamics and Heat Transfer”, McGraw-Hill, 2005

[17] G.C. Botura, D. Sweet, D. Flosdorf, “Development and demonstration of low power electro-thermal de-icing system”, AIAA 2005-1460, Reno 2005

[18] M.B. Bragg, T. Basar, W.R. Perkins, M.S. Selig, P.G. Voulgaris, J.W. Melody, N.B. Sarter, “Smart icing systems for aircraft icing safety”, AIAA 2002-0813, 2002

[19] M.B. Bragg, W.R. Perkins, B. Sarter, T. Basar, P. G. Voulgaris, H.M. Gurbacki, J. W. Melody, S.A. MCray, “An interdisciplinary approach to in-flight aircraft icing safety”, AIAA 98-0095, 1998

[20] R.J. Scavuzzo, M.L. Chu, C.J. Kellackey, “Structural analysis and properties of impact ices accreted on AC structures”, NASA-CR-198473, 1996

[21] K.M. Al-Khalil, M.G. Potepezuk, “Numerical modelling of anti-icing system and comparison to test results on a NACA0012 airfoil”, NASA-TM-105975, 1993

[22] I. Paraschivoiu, F. Saeed, “Aircraft Icing”, JOHN WILEY & SONS, 2004

[23] A.E. Von Doenhoff, E.A. Horton, “A Low Speed Experimental Investigation of the Effect of Sandpaper Type of Roughness on Boundary-Layer Transition,” NACA TN 3858, 1956

[24] P.T. Hacker, R.G. Dorsch, “A summary of meteorological conditions associated with aircraft icing and proposed method of selecting design criterions for ice-protection equipment”, NACA-TN-2569, 1951

[25] A.R. Jones, W. Lewis, ”Recommended values of meteorological factors to considered in the design of aircraft ice prevention equipment” NACA-TN-1855, 1949

[26] T. Bond, “Proposed Expanded Icing Envelope”, NTSB, DN SA533 EN 13-I, FAA 2009

[27] J.P. Lewis, R.S. Ruggeri, “Experimental droplet impingement on four bodies of revolution”, NACA-TN-4092, 1957

[28] T.F. Gelder, J.P. Lewis, S.L. Koutz, “Icing protection for a turbojet transport airplane: heating requirements, method of protection and performance penalties”, NACA-TN-2866, 1953

[29] F. Saeed, M.S. Selig, M.B. Bragg, “Hybrid Airfoil De-icing Procedure Validation for full-scale Ice Accretion Simulation”, Journal of Aircraft, Vol. 36, No. 5, 1999

[30] V.H. Gray, D.T. Bowden, U. von Glahn, “Preliminary results of cyclical de-icing of a gas heated airfoil”, NACA-RM-E51J29, 1952

[31] D.N. Anderson, “Manual of Scaling Methods”, NASA-CR-2004-212875, 2004

[32] F. Muller-Plathe, S. Pal, H. Weiss, H. Keller, “Can Nanostructuring improve the properties of hydrophobic surfaces?”, Soft Materials, Vol.3 N1, 2005

[33] L.M.K. Boelter, L.M. Grossman, R.C. Martinelli, E.H. Morrin, “An investigation of Aircraft heaters”, NACA-TN-1453

[34] X. Wang, E. Bibeau, G.F. Naterer, “Experimental correlation of forced convection heat transfer from a NACA airfoil”, *Experimental Thermal and Fluid Science, Volume 31, Issue 8, 2007, Pages 1073-1082*

[35] X. Wang, E. Bibeau, G.F. Naterer, ”Modified Hilpert Correlation for Turbulent Convective Heat Transfer from a NACA Airfoil”, AIAA 2007-4391, 2007

[36] X. Wang, G.F. Naterer, E. Bibeau, “Convective Droplet Impact and Heat Transfer from a NACA Airfoil”, JOURNAL OF THERMOPHYSICS AND HEAT TRANSFER, Vol. 21, No. 3, 2007

[37] D.N. Anderson, “Acceptable Tolerances for Matching Icing Similarity Parameters in Scaling Applications”, NASA-CR-2003-211822, 2001

[38] D.N. Anderson, “A Preliminary Study of Ice-Accretion Scaling for SLD Conditions”, NASA-CR-2003-211824, 2003

[39] G.C.Botura, D.N. Anderson, A.P. Broeren, “A Study of Scaling for Inter-cycle Ice Accretion Tests”, NASA-CR-2003-211825, 2001

[40] D.N. Anderson, A. Feo, “Ice-Accretion Scaling Using Water-Film Thickness Parameters”, NASA-CR-2003-211826, 2003

[41] D.N. Anderson, “Effect of Velocity in Icing Scaling Tests”, NASA-CR-2003-211828, 2000

[42] G.A. Ruff, D.N. Anderson, “Quantification of Ice Accretions for Icing Scaling Evaluations”, NASA-TM-2003-212308, 1998

[43] D.N. Anderson, G.A. Ruff, “Evaluation of Methods to Select Scale Velocities in Icing Scaling Tests”, NASA-CR-2003-211827, 1999

[44] J. Cole, W. Sand, , “Statistical Study of Aircraft Icing Accidents,” AIAA Paper 91-0558, Jan. 1991.

[45] B.L. Messinger, “Equilibrium Temperature of an Unheated Icing Surface as a Function of Air Speed,” Journal of Aeronautical Sciences, Vol. 20., No. 1, Jan. 1953.

[46] R.J. Hansman, K.S.Breuer, D. Hazan, A. Reehorst, M. Vargas, “Close-Up Analysis of Aircraft Ice Accretion,” AIAA Paper 93-0029, Jan. 1993.

[47] W.R. Sand, C.J. Biter, “Meteorology Surrounding the Roselawn Accident,” AIAA-99-0496, 1999.

[48] M.T. Brahimi, P. Tran, D. Chocron, F. Tezok, I. Paraschivoiu, “Effect of Supercooled Large Droplets on Ice Accretion Characteristics,” AIAA-97-0306, 1997.

[49] C.L. Johnson, “Wing Loading, Icing and Associated Aspects of Modern Transport Design,” Journal of Aeronautical Sciences, Vol. 8, No. 2, Dec. 1940, pp. 43-54.

[50] K. Al-Khalil, “Assessment of Effects of Mixed-Phase Icing Conditions on Thermal Ice Proten Systems”, DOT/FAA/AR-03/48, 2003

[51] B.C. Bernstein, T.P. Ratvasky, D.R. Miller, F. McDonough, , “Freezing Rain as an In-Flight Hazard,” NASA TM 2000-210058, 2000.

[52] M.B. Bragg, “Aircraft Aerodynamic Effects Due To Large Droplet Ice Accretions,” AIAA-96-0932, 1996.

[53] M.B. Bragg, “Aerodynamics of Supercooled-Large-Droplet Ice Accretion and the Effect on Aircraft Control,” DOT/FAA/AR-96/81,II, 1996

[54] R. Ashenden, J. Marwitz, “Turboprop Aircraft Performance Response To Various Environmental Conditions,” AIAA97-0305, 1997

[55] S. Lee, H.S, Kim, M.B. Bragg, “Investigation of Factors that Influence Iced-Airfoil Aerodynamics,” AIAA-2000-0099, 2000

[56] M.B. Bragg, A. Khodadoust, S.A. Spring, "Measurements in a Leading-Edge Separation Bubble due to a Simulated Airfoil Ice Accretion," AIAA Journal, Vol. 30, No. 6, June 1992

.

[57] R.E. Brumby, “Wing Surface Roughness – Cause & Effect,” D.C. Flight Approach, Jan. 1979, pp. 2-7.

[58] H.S. Kim, M.B. Bragg, “Effects of Leading-Edge Ice Accretion Geometry on Airfoil Performance,” AIAA Paper 99-3150, 1999.

[59] W.B. Wright, J.K. Chung, “Correlation Between Geometric Similarity of Ice Shapes and the Resulting Aerodynamic Performance Degradation - A Preliminary Investigation Using WIND,” AIAA Paper 2000-0097, 2000.

[60] N. Gregory, C.L. O’Reilly, “Low-Speed Aerodynamic Characteristics of NACA 0012 Aerofoil Section, including the Effects of Upper-Surface Roughness Simulating Hoar Frost,” ARC R&M 3726, Jan. 1970.

[61] W.H. Rae, A. Pope, “Low-Speed Wind Tunnel Testing”, John Wiley & Sons, New York, 1984. 287

[62] H.W. Coleman, W.G. Steel Jr., “Experimentation and Uncertainty Analysis for Engineers”, John Wiley & Sons, Inc., New York, 1989.

[63] R. Ashenden, W. Lindberg, J. Marwitz, “Two-Dimensional NACA 23012 Airfoil Performance Degradation by Super Cooled Cloud, Drizzle, and Rain Drop Icing,” AIAA, 1996

[64] K.M. Al-Khalil, T.W. Ferguson, D.M. Phillips, “A Hybrid Anti-Icing Ice Protection System,” AIAA Paper 97-0302, Jan. 1997

[65] S.K. Thomas, R.P. Cassoni, C.D. MacArthur, “Aircraft Anti-Icing and Deicing Techniques and Modeling,” Journal of Aircraft, Vol. 33, No. 5, 1996, pp. 841–854

[66] R. Henry, “Development of an Electrothermal De-Icing/Anti-Icing Model,” AIAA Paper 92-0526, 1992.

About the Author

Francesco de Rosa, born in Telese Terme -BN- Italy in 1970, has been working for over 15 years either for the Aerospace Industry either for the Aerospace Research and is today Senior Aircraft Structural Consultant for major Aerospace Companies and Research Centers. Long has been his cooperation with Department of Aerospace Engineering at University of Naples where he has been co-Author of several papers about Experimental Hypersonic Aerodynamics, Icing Wind Tunnels and Aircraft Anti-icing applications.